PARTICLE TRANSPORT IN TOKAMAK PLASMAS

THÈSE N^O 3252 (2005)

PRÉSENTÉE À LA FACULTÉ SCIENCES DE BASE

CRPP Association Euratom

SECTION DE PHYSIQUE

ÉCOLE POLYTECHNIQUE FÉDÉRALE DE LAUSANNE

POUR L'OBTENTION DU GRADE DE DOCTEUR ÈS SCIENCES

PAR

Alexey ZABOLOTSKIY

M.Sc. in physics, Université de Novosibirsk, Russie
et de nationalité russe

accepTée sur proposition du jury:

Dr H. Weisen, directeur de thèse
Prof. A. Bay, rapporteur
Dr R. Dux, rapporteur
Dr X. Garbet, rapporteur

Lausanne, EPFL
2005

Version abrégée

Le transport des particules dans les plasmas confinés magnétiquement est d'une grande importance pour le développement de l'énergie de fusion. Il sera déterminant pour les techniques d'alimentation en combustible, pour le contrôle des impuretés et pour l'évacuation des particules alpha produites par les réactions de fusion. Les questions liées au transport des particules ont reçu, jusqu'a relativement récemment, moins d'attention que celles concernant le transport de la chaleur. Ajouté a la difficulté plus grande des mesure expérimentales de transport des particules, ceci peut expliquer pourquoi notre compréhension de ce sujet est encore lacunaire.

Le but de cette thèse est de documenter expérimentalement le comportement des profils de densité dans les tokamaks TCV (*Tokamak à Configuration Variable*) et JET (*Joint European Torus*) et d'en tenter des interprétations dans le cadre de différents modèles théoriques et empiriques. Le tokamak TCV est bien adapté aux études de transport des particules grâce à ses possibilités extrêmes de variation de forme, qui permettent d'explorer un large éventail de différentes conditions de plasma. Cette polyvalence est renforcée par le système puissant et flexible de chauffage cyclotronique électronique (ECH) de TCV, qui permet de contrôler les profils locaux de dépôt de puissance et des profils de courant non inductif. Une étude sur le tokamak JET nous a permis de comparer les résultats de TCV à ceux obtenus dans un dispositif beaucoup plus grand et de compléter ainsi les étude de TCV avec l'analyse d'un régime pertinent à un réacteur, le mode de haut confinement (mode H).

L'information expérimentale a été assemblée dans une base de données des profils de densité en état d'équilibre, qui contient près de 1000 échantillons pour TCV et 600 échantillons pour JET. Les données analysées sont représentatives d'un vaste éventail de conditions de décharge, comprenant le mode de bas confinement (mode L), le mode H, des types de chauffage différents, nottamment l'ECH, l'ICH (chauffage cyclotronique ionique), la LHCD (chauffage par ondes hybrides inférieures), et le NBI (chauffage par injection de faisceaux des neutres énergétiques), et comprennent des décharges dont le courant est

entièrement générée de maniere non inductive. Les paramètres les plus important qui influencent les profils de densité ont été déterminés par régression statistique.

Une analyse détaillée des sources de particules a prouvé que les particules neutres qui pénètrent depuis le bord dans TCV et JET ne peuvent pas être responsables du gradient de densité a l'intérieur de plasma, confirmant la présence d'un transport convectif de particules ('pincement'). L'existence d'un pincement anomal a été clairement démontrée sur JET et sur TCV par l'observation des profils piqués dans des décharges stationaires soutenues entièrement par un courant non inductif, c.à.d. en l'absence du pincement néoclassique de Ware. Une différence inattendue dans les dépendances paramétriques a été trouvée entre les mode L et H. En mode L, dans TCV et dans JET, les longueurs de gradient de densité (ou le 'piquage' des profils) dépendent du cisaillement magnétique et sont indépendants de la collisionalité électronique. L'absence de dépendance de la collisionalité en mode L est en contradiction avec les modèles théoriques existants. Les profils de densité en mode H dans JET, par contre, dépendent clairement de la collisionalité en accord avec la théorie et avec une observation antérieure dans le tokamak ASDEX-Upgrade, tout en exhibant seulement une faible, voire aucune dépendance des profils de cisaillement et de température.

En mode L, tant dans TCV que dans JET, le piquage de densité peut être interpreté comme étant dû a l'equipartition turbulente, qui est basée sur l'hypothèse la conservation du moment magnétique et l'invariant longitudinal pendant le transport. L'observation d'une réduction du piquage sur TCV avec ECH soutient la théorie de turbulence des ondes de dérives, qui prévoit l'apparition d'une convection des particules dirigée vers l'extérieur, quand les modes d'électrons piégés sont déstabilisés. Dans le mode H sur JET, l'observation d'une corrélation secondaire faible du piquage et du rapport des températures électronique et ionique, T_e/T_i, peut également être considéré, au moins qualitativement, comme étant en accord avec la théorie de la turbulence des ondes de dérive.

Abstract

The transport of particles in magnetically confined plasmas is of great importance for the development of fusion energy. It will determine techniques for fuelling, for controlling impurity concentrations and for the removal of the alpha particles produced by fusion reactions. The issues related to particle transport have received, until relatively recently, less attention than those regarding heat transport. Besides the greater experimental difficulty of measuring particle transport, this may explain why our understanding of this subject is still incomplete.

The aim of this thesis is to document and tentatively interpret the experimental density profile behaviour in the TCV (*Tokamak à Configuration Variable*) and JET (*Joint European Torus*) tokamaks in the framework of different theoretical and semi-empirical models. The TCV tokamak is well suited to transport studies due to its extreme shaping capability, which allows the exploration of a wide range of different plasma conditions. This versatility is matched by the powerful and flexible electron cyclotron heating (ECH) system on TCV, which allows a control of the local power deposition profiles and current drive profiles. A study of particle transport on the JET tokamak has allowed us to compare the results of TCV to those of a much larger device and supplement the TCV study with the analysis in reactor relevant high confinement regime (H-mode).

The experimental information was compiled into a database of density profiles in steady state, containing nearly 1000 samples for TCV and 600 samples for JET. The data analyzed covered a wide range of discharge conditions, including low confinement regime (L-mode) and H-mode discharges, ECH, ICH (ion cyclotron heating), LHCD (low hybrid), beam heated plasmas and include fully current drive discharges. The most relevant parameters which influence the density profiles were determined by regression.

A detailed analysis of the particle sources showed that edge fuelling in TCV and JET cannot be responsible for density gradient in the plasma bulk, confirming the presence of particle convection or a 'pinch'. The existence of an anomalous pinch was unambiguously demonstrated both on JET and on TCV by the observation of peaked density profiles in

stationary, fully relaxed, fully current driven discharges and hence in the absence of the neoclassical Ware pinch. An unexpected difference in the parameter dependencies was found in L-and H-modes. In TCV and JET, density gradient lengths (or profile peaking parameters) in L-mode were found to depend on magnetic shear with no dependence on collisionality. This lack of collisionality dependence in L- mode is inconsistent with current theoretical models. H-mode density profiles in JET, on the other hand, are clearly dependent on collisionality in agreement with theory and a prior observation on ASDEX-Upgrade, while exhibiting only a weak or no dependence on shear and temperature profiles.

It was found that for TCV and JET, L mode density peaking can be interpreted as being due to turbulent equipartition, which assumes conservation of the magnetic moment and the longitudinal invariant during transport. The observation of a reduction of peaking in TCV with ECH supports drift wave turbulence theory, which predicts the appearance of outward particle convection, when trapped electron modes are destabilized. In JET H-mode, the weak secondary correlation of peaking with the electron-ion temperature ratio T_e/T_i, may also be considered, at least quantitatively, as being supportive of drift wave turbulence theory.

Contents

Chapter 1

Introduction

1.1 Nuclear fusion

Nuclear fusion is a nuclear reaction which two light nuclei merge, forming a larger nucleus and releasing the energy corresponding to the difference of the masses of reactants and products of the reaction. There are several fusion reactions that can be considered for energy production of these the easiest to achieve is the reaction between the two heavier isotopes of hydrogen, deuterium and tritium

$$_1D^2 + \; _1T^3 \longrightarrow \; _2He^4 \,(3.50\,MeV) + \; _0n^1 \,(14.1\,MeV) \tag{1.1}$$
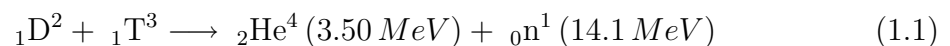
D is contained in water in the form of molecules of semiheavy water HDO. Despite the fact that for 6500 molecules of H_2O, there is only one molecule of HDO, the energy which can in principle be extracted from one litre of water is 300 times larger than the energy obtained from combustion of 1 litre of gasoline. Tritium does not occur naturally, but can be produced in the fusion reactor by exposing lithium present in the Earth's crust to the neutron flux from fusion reactions.

An advantage of fusion energy with respect to conventional fossil energy is the absence of CO_2 emission, claimed to be responsible for "greenhouse" effect. Compared to fission reactors, fusion reactors are much safer, since only a small amount of fuel is involved in the reaction and the radioactive waste from fusion reactors is mainly due to the activation of structural materials by neutrons. This activation can be kept short lived (< 100 years) by a careful selection of materials. Therefore fusion energy is one of only a few future power sources with the potential to be both economically acceptable and attractive in

terms of safety and its impact on the environment.

A substantial energy barrier opposes the fusion reaction. This barrier can be overcome if the reactants involved have a temperature of the order of $10 - 100 \ keV$ (1 $eV = 11'600^0$ K), at which nearly all matter exists in the form of a fully ionized gas, called plasma. Once a critical temperature for nuclear fusion has been achieved, plasma must be maintained at that temperature for a long enough time at a high enough ion density to obtain a net yield of energy. The most desirable operating regime for the reactor is called ignition, at which no external heat source are required and the losses of the energy are compensated by the energy deposition of fusion α particles. The criterium to achieve the ignition condition, proposed by Lawson gives the limit on the product of density, temperature and confinement time

$$nT\tau_E > 5 \cdot 10^{21} \ m^{-3} \ \text{keV s}$$

The limit on product rather than on values leaves some freedom in the choices of the thermonuclear plasma confinement method. Mainly two approaches in confinement are pursued at present in the world - one based on inertial confinement and the other based on magnetic confinement. In the inertial confinement approach conditions for fusion reactions are reached by creating a plasma sufficiently dense in order to release enough energy at the time scale below the natural inertia, with no effort being made to confine the plasma. The basic idea is to compress a small pellet (in the order of $1 - 10 \ mm$) of D-T to densities of order of $10^{27} - 10^{28} \ m^{-3}$, heating it at the same time to thermonuclear temperatures for $10 - 100 \ ns$. At the present time, laser beams are the most highly developed means for inertial confinement, and the progress in increasing the power gain (a ratio between fusion power and input power) is similar to that for magnetic confinement, although laser beam fusion has not yet achieved results close to the Lawson criteria [1].

In the magnetic confinement approach, the plasma is maintained inside the reactor volume by external magnetic fields. Magnetic confinement devices feature relatively low density plasmas $\sim 10^{19} - 10^{21} \ m^{-3}$, limited by the strength of the magnetic field. However, higher confinement times than in inertial fusion devices, of the order of $0.5 - 10 \ s$, still allow to satisfy the Lawson criterion for energy production. A number of different configurations for achieving fusion conditions have been proposed over the years. Some of the more

common ones include: tokamaks [2–4], stellarators [5,6], magnetic mirrors [7] and reversed field pinches [8]. The tokamaks and stellarators are equally promising as a future fusion reactor, however stellarators are less advanced because they have not, so far, benefited from the same level of resources as tokamaks.

1.2 The tokamak concept

A tokamak is a toroidal plasma confinement device invented in the 1950s by the Russians Igor Tamm and Andrei Sakharov. The word "tokamak" is a contraction of the Russian words meaning "toroidal chamber with magnetic coils". The essential tokamak geometry is shown in Fig. 1.1. The tokamak is characterized by a plasma current which creates the magnetic configuration and heats the plasma at the same time. The magnetic fields in a tokamak are produced by a combination of currents flowing in external coils and the currents flowing within the plasma itself. The poloidal component of the magnetic field is produced by current in the plasma superimposed on the toroidal component of the magnetic field produced by current in the external coils. The resulting magnetic field lines form the toroidal helixes. Actually, the toroidal and poloidal fields alone are not enough to confine the plasma in the tokamak. The plasma current J interacts with the poloidal field B, which is weaker on the outside of the torus than on inside, to produce a net $J \times B$ force directed outward along the major radius of the torus. Under the influence of this force the plasma major radius would increase until it reaches the wall. An equilibrium thus can be established in a tokamak only by applying a restoring force to overcome this tendency of the plasma to expand outward. This force is created by an external vertical magnetic field B_v applied in a direction parallel to major axis of the torus. This magnetic field interacts with the toroidal plasma current to produce inward directed $J \times B_v$ force which stops the outward expansion of the plasma.

The important feature of tokamaks is that their magnetic field configuration is sheared. Shear occurs because the plasma current produces a poloidal field which is small near the minor axis of the torus and increases to a maximum near $r/a \sim 0.7$, where r is minor radius and a is a radius of last closed flux surface, while the toroidal field varies slowly across the cross section. The net result is a change in the pitch of the helical field lines.
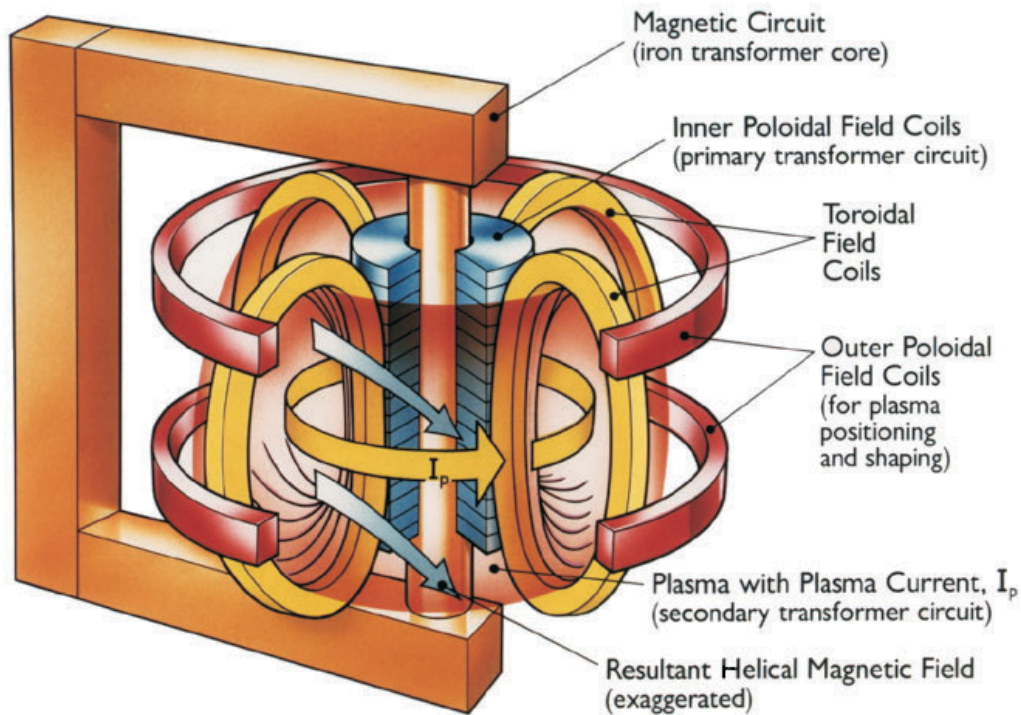
Figure 1.1: *Schematic representation of the tokamak device.*

The current circulating in the tokamak heats the plasma resistively. However, the decrease of the resistivity with increase of temperature limits the possible temperature attainable by resistive dissipation. Moreover, an inductively produced current can only be sustained for a limited time. Auxiliary heating is therefore required to reach high temperatures and non inductive current drive is needed for steady state operation.

1.3   Particle transport in tokamaks

In fusion reactor plasmas, a sustained burn cannot be achieved if the ratio of particle- to energy confinement times exceeds a critical value. Therefore, a crucial problem in fusion research is to understand the heat and particle transport perpendicular to magnetic field lines in hot plasmas.

Both heat and the particle transport play an important role in the determination of the confinement properties of reactor plasmas, however particle transport in tokamaks has received much less attention in plasma research than heat transport. In part this fact

is attributable to the greater experimental difficulties for example in direct measurements of particle sources at the plasma periphery.

Experimental observations in all tokamaks have shown that the particle transport is usually higher than predicted by collisional processes alone [9]. This so-called anomalous transport is mainly associated with small-scale instabilities generating turbulence and large scale relaxation events which can redistribute heat and particles over a sizeable fraction of the cross section. However, the limited amount of the experimental data, as well as the complex nature of the processes involved, do not currently allow to make an extrapolation of existing results to reactor conditions. Moreover, no theory-based description for particle transport in tokamak plasmas can today reproduce the whole range of existing experimental results.

One important issue of tokamak particle transport is the existence of inward particle convection (or 'pinch'). The presence of such a pinch is most easily seen from the fact that the density profile in tokamaks is peaked in the centre, where there are no particle sources. Peaked electron and fuel density profiles in reactor plasmas are advantageous since at fixed edge density a fusion power

$$P = \frac{1}{4}n^2 < \sigma v > E$$

(where $< \sigma v >$ is the rate coefficient for reaction, E is the energy released per reaction and n is the density of deuterium equal to density of tritium) is higher in the core. This is particulary important if the density limit, as recently extrapolated from JET and ASDEX Upgrade H-mode discharges [10], restrains the reactor edge density below the generally accepted value [11]. A peaked density profile increases also the bootstrap current $j_b \propto dn/dr$. The bootstrap current, driven dominantly by the density gradient, is important in non inductive scenarios relevant for the fusion reactor. The presence of the inward convection may, however, cause impurity accumulation in the plasma core and as a result may decrease the reactor performance due to increased level of radiation losses and dilution.

The nature of the inward particle pinch, which leads to the observed peaking of the density profile in tokamaks, has been the subject of controversy for a long time [9]. Recent experiments of fully current driven plasmas with negligible particle source in Tore

Supra [12] and TCV [13] have shown that substantial peaking is obtained in the absence of the neoclassical Ware pinch [14] ($V_{Ware} \propto E_{tor}/B_{pol}$), providing an unambiguous demonstration of the existence of anomalous pinches. Transport simulations for a variety of JET discharges have also concluded that an anomalous pinch must be present in the gradient zone ($r/a > 0.5$), at least in L-mode plasmas [15]. The situation is more complicated in H-modes because sawteeth, ELMs, neutral beam fuelling and a significant Ware pinch may all contribute to the particle balance. The theoretical candidates for explaining anomalously high convection are turbulent equipartition (TEP) [16–20] or equivalently, its fluid counterpart, the anomalous curvature pinch and anomalous thermodiffusion [21–26]. Neoclassical thermodiffusion [27] may only be expected to be important in regions with strongly reduced anomalous particle diffusivity.

1.4   Outline of the thesis

A brief introduction to nuclear fusion, to the tokamak as a possible concept to exploit fusion as a future energy source and an introduction to particle transport in tokamaks has been given in this chapter. The rest of this thesis is organized as follows. Chapter 2 is dedicated to a presentation of the TCV and JET tokamaks, its heating systems and main diagnostics used for particle transport studies. Chapter 2 includes an investigation of the consistency of density profile data, produced by different diagnostics. As an alternative to Thomson scattering measurements, methods of inversion of line integrated density measurements are proposed. Chapter 3 is devoted to a brief introduction to the theories of particle transport in tokamaks. In chapter 4, a detailed study of the influence of the particle source term on density peaking, both in JET and TCV is presented. Chapter 4 includes the results of simulations using a one dimensional kinetic particle transport code as well as a selection of experimental results destined to indicate the importance of edge neutrals in the total particle balance. The experimentally observed density profile behaviour in different discharge conditions, including Ohmic L-modes, electron cyclotron heated L-mode plasmas, discharges with electron internal transport barriers are analyzed in chapter 5 using comprehensive databases. Tests of three pinch models, the Ware pinch, turbulent equipartition and turbulent thermodiffusion, against the experimental data are presented.

In chapter 6 a study of density profile behaviour in JET L- and H- mode discharges is presented. The statistical scaling of the density peaking with the plasma parameters is analysed over several hundreds experimental data points. The possible explanation of the observed particle pinch in L-mode in the framework of turbulent equipartition and turbulent thermodiffusion is discussed. Although the bulk of this work is on particle, or more precisely on electron transport, this thesis also makes first step in addressing the issue of a method for estimating the transport coefficients of the intrinsic impurity carbon. This method presented in chapter 7 is based on the interpretation of measured profiles of the He-like and H-like ionization stages, using a multichannel ultra soft x-ray spectrometer. A comparison of the experimental profiles with simulations performed by the impurity transport code STRAHL allowed to infer carbon diffusivity profiles in TCV. The conclusions of this work are presented in the chapter 8.

Chapter 2

TCV and JET tokamaks

2.1 The TCV tokamak

The Tokamak à Configuration Variable (TCV) at the Centre de Recherche en Physique de Plasmas (CRPP) is a medium size tokamak. TCV has been designed (see main parameters in Table 2.1) explicitly for the study of the effect of the plasma shape on confinement and stability. The device has a rectangular vacuum vessel with a height-to-width ratio of 2.9, surrounded by 16 shaping coils. The flexibility of TCV allows to obtain different plasma configurations and shapes, not only from one discharge to another, but during a single discharge. Some examples of the TCV poloidal shapes produced on TCV since November 1992 are presented in Fig. 2.2.

TCV is equipped with a powerful and flexible Electron Cyclotron Resonance Heating (ECRH) system able to produce Electron Cyclotron Current Drive (ECCD). The system consist of six 82.7 GHz gyrotrons coupled in two clusters for heating at the second harmonic of the electron cyclotron resonance and a cluster of three 118 GHz gyrotrons for heating at the third harmonic. The 82.7 GHz gyrotrons are located on two equatorial and four upper lateral ports (Fig. 2.1). The nominal power of each 82.7 GHz gyrotron is 0.5 MW, resulting in total of 3 MW of nominal heating power at the second harmonic ($\sim 2.7\ MW$ is delivered to plasma) with a maximum pulse length of 2 seconds. Each launcher has two degrees of freedom, one in the poloidal direction and one in the toroidal direction. The poloidal injection angle can be changed during the discharge, allowing to perform power deposition location sweeps. Variations of the toroidal injection angle can

Parameters	Value
Major radius	0.88 m
Minor radius	0.25 m
Aspect ratio	~ 0.36
Toroidal magnetic field	1.4 T
Maximum plasma current	1 MA
Loop voltage	$< 10V$
Plasma elongation	$1 \div 2.8$
Plasma triangularity	$-0.7 \div 1$
Discharge duration	< 4 s

Table 2.1: *Principal characteristics of TCV tokamak*

be performed between discharges in order to change the fraction and direction of current drive in the plasma. The polarization of each beam can be adjusted to create the extraordinary "X" (wave electric field $\vec{E}$ perpendicular to the local magnetic field) or ordinary "O" wave ($\vec{E}||\vec{B}$). Since the second harmonic X-mode is better absorbed than the second harmonic O-mode, the polarization of all beams is usually set to X-mode, further referred to as X2 in the case of the heating at the second harmonic and as X3 for third harmonic heating.

The cut-off density determined from the refraction index for the X2 wave is $n_e \sim 4{\cdot}10^{19}$ m^{-3}. In order to extend the accessible domain of operation up to $n_e \sim 1.1 \cdot 10^{20}$ m^{-3}, the 118 GHz gyrotrons for X3 heating were recently added. A common launcher for the 118 GHz gyrotrons is located at the top of the vessel (Fig. 2.1). Each gyrotron provides 0.46 MW of power and in total 1.4 MW of heating with a maximum pulse length of 2 s can be coupled into the plasma. The steerable mirror provides nearly tangential injection to the resonance surface, maximising the interaction with resonant electrons and as a result, increasing the power absorbtion. The injection of the heating beam from the low or the high field side with respect to the resonance is determined by the position of the mirror, which can be displaced between discharges.

The calculations of the absorbtion of X2 and X3 waves as well as the fraction of the current drive are performed using a linear ray tracing code TORAY-GA [28].
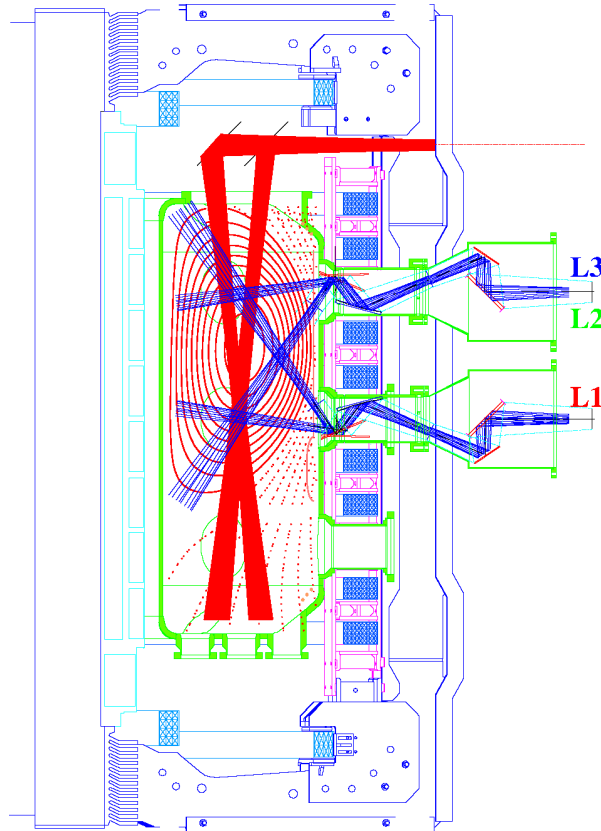
Figure 2.1: *Poloidal view of the TCV ECRH system*

2.2 TCV diagnostics

TCV has a broad operational domain, with a large variety of plasma shapes, sizes and positions. As a result TCV is equipped with comprehensive set of diagnostics, several of which offer a complete coverage of the highly elongated vacuum vessel. Standard diagnostics in TCV include Thomson scattering (TS) for measuring the electron temperature and the electron density profiles, a multichannel far-infra red (FIR) interferometer measuring the line integrated electron density and several multichannel systems for plasma radiation measurement: a soft x-ray (SXR) tomographic system, a multiwire X-ray proportional detector, a set of foil bolometers and a bolometric system using dead-layer free Si diodes arrays. TCV was recently equipped with a neutral diagnostic beam together with charge exchange spectroscopy (CXS), which is used to obtain profiles of light impurities as well as of ion temperature. A system designed to measure plasma electron cyclotron emission (ECE) allows a measurement of the profiles of the electron temperature with high time

a) #9849 – t=0.50s

b) #6010 – t=0.80s

c) #5650 – t=0.80s

d) #8856 – t=0.29s

Limited (κ=1.2, δ=0.0, Ip=230kA)

SND upper (Ip=330kA)

SND lower (Ip=335kA)

DND (Ip=325kA)

e) #11368 – t=0.65s

f) #18548 – t=1.50s

g) #6442 – t=0.50s

h) #10159 – t=0.01s

Highest current, Ip=1.06MA

Highest fully ECCD driven current, Ip=210kA

Pear shape (Ip=360kA)

Doublet shape (Ip=115kA)

i) #19373 – t=0.42s

j) #8890 – t=0.75s

k) #11928 – t=0.67s

l) #11962 – t=1.00s

Highest elongation, κ=2.80

Highest triangularity, δ=0.86

Lowest triangularity, δ=−0.77
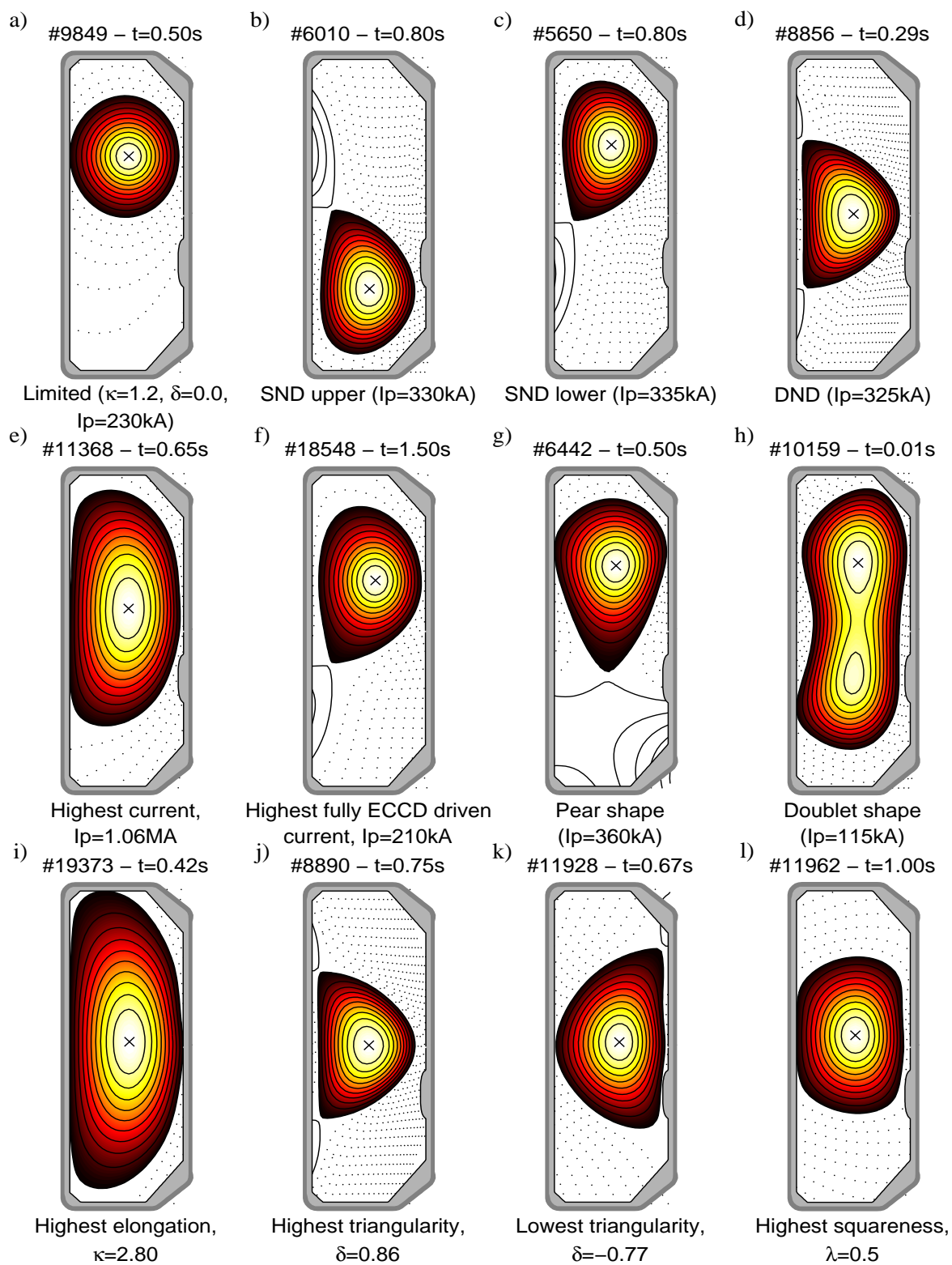
Highest squareness, λ=0.5

Figure 2.2: *TCV shapes*

resolution. In the following sections we describe in details only the TS, FIR and SXR, which are the diagnostics having provided the most important measurements relevant for present work. The ultra soft x-ray (USX) spectrometer used in this work for impurity transport study will be introduced in chapter 7.

2.2.1 Thomson scattering
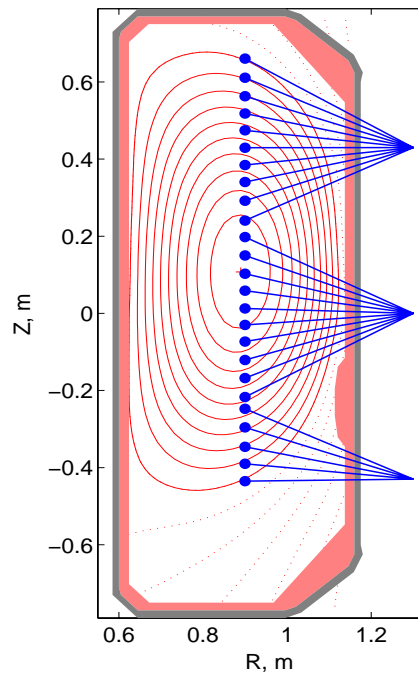
Figure 2.3: *Poloidal section of TCV with 25 viewing chords of the Thomson scattering diagnostic. Dots mark the volumes from which scattered light is collected.*

The Thomson scattering diagnostic makes use of a laser beam that passes through the plasma and interacts with free plasma electrons, so that a minute amount of the laser light is scattered from them. The analysis of scattered light gives local values of the electron temperature and the density since the spectral width of the scattered radiation depends on the electron temperature (due to Doppler line broadening), and its intensity is related to the electron density [29].

At TCV, three Nd-Yag lasers (1.06 mm) are used with a repetition rate of 20 Hz, delivering 1 J per pulse [30]. Three sets of wide angle lenses on 3 lateral ports allow at present measurements at 25 positions with a spatial resolution of 4 cm (see Fig. 2.3).

Figure 2.4: *Schematic representation of a single channel Mach-Zehnder heterodyne interferometer set-up (left). Experimental setup of the TCV multichannel far infrared interferometer (right). The chord used for the density feedback control of the plasma is highlighted*

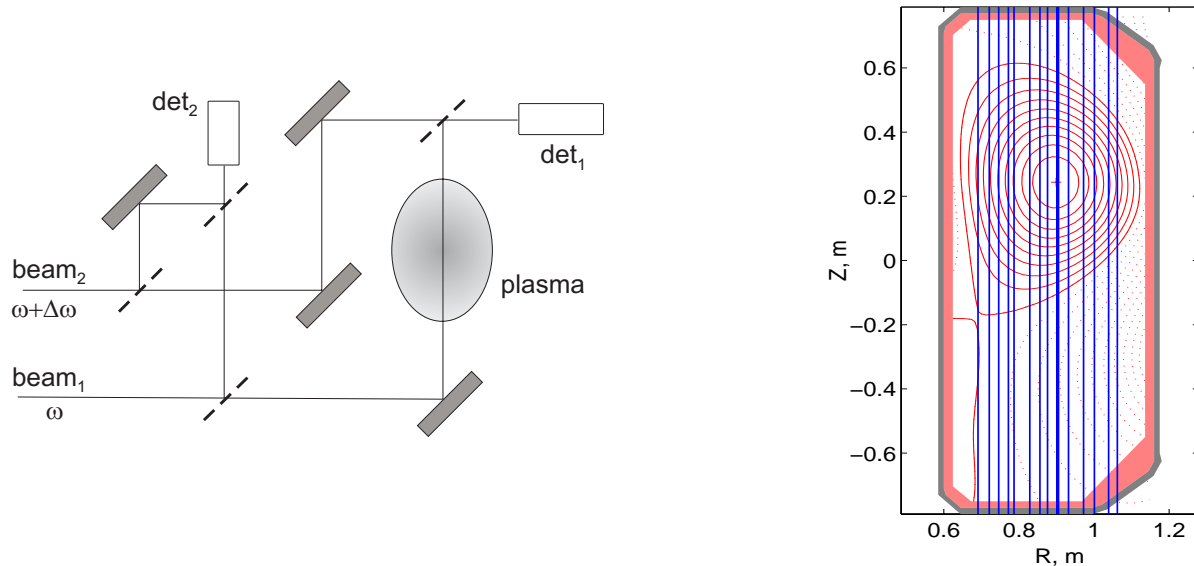Optical fibre bundles transfer scattered light into polychromators equipped with 3 or 4 broadband filters. Si-avalanche photodiodes finally convert the detected light into an electric signal. The system is absolutely calibrated by means of Raman scattering from nitrogen introduced into the TCV vessel.

The strength of the TS technique is that it provides accurate localized measurements, with systematic uncertainties less than 5%. On the other hand, the very small scattering cross section can lead to statistical errors of the order of 10%. Moreover, powerful pulsed lasers are needed to be used in order to produce sufficient useful light and therefore the measurements are not continuous in time.

2.2.2   The FIR interferometer

A 14 vertical channel FIR interferometer build using the heterodyne Mach-Zehnder scheme is used to measure the line integrated electron densities in TCV (Fig. 2.4). A schematic of a single channel Mach-Zehnder heterodyne interferometer is shown in Fig. 2.4 (left). Heterodyne or double-frequency detection makes use of two beams with slightly different frequency ($\Delta\omega = 6.28 \cdot 10^5 \ rad/s$ in TCV), one of which passes through the plasma.

The two beams are then recombined on a detector (det_1). A reference detector (det_2) completes the setup collecting an unperturbed signal from both beams. Assuming the electric vector of the two beams before the recombination to be $E_1 = |E_1|e^{i(\omega t + \Phi(t) + \phi_1)}$ and $E_2 = |E_2|e^{i(\omega t + \phi_2)}$, where $\Phi(t)$ is the time-varying phase shift due to the plasma electron density and ϕ_1 and ϕ_2 are constant over time, the resulting intensity on the detector (det_1) can be written as

$$I_{det_1} = |E_1 + E_2|^2 = |E_1|^2 + |E_2|^2 + 2|E_1||E_2|\cos(\Delta\omega t - \Phi(t) - \phi_1)$$

The resulting signal, after filtering out the dc term, is proportional to

$$S_{det_1} \propto |E_1||E_2|\cos(\Delta\omega t - \Phi(t) - \phi_1)$$

The phase shift $\Phi(t)$ due to the plasma can be determined by comparing the phase shift of the signal on det_1 to that of a reference ac signal on det_2,

$$S_{det_2} \propto |E_1||E_2|\cos(\Delta\omega t - \phi_2)$$

and taking into account the fact that the phase offset $\phi_2 - \phi_1$ remains constant over time. The relative phase delay $\Phi(t)$ between the beams passing through the plasma and the reference beam, is due to an increase of the phase velocity of light through the plasma and thus to the refractive index of the plasma. The line integrated plasma density is thereafter derived from [31]

$$\int n_e dl = \frac{4\pi\varepsilon_0 m_e c^2}{e^2 \lambda}\Phi(t)$$

where λ is the wavelength of the laser.

The TCV FIR interferometer makes use of a CO_2 laser which pumps the 213.6 μm line of CH_2F_2. The infrared laser light is divided into the reference beam and a wide slab beam encompassing most of the cross-section. The 14 measurement chords are defined by the positions of the dielectric waveguides, installed behind a wire mesh, which combines the reference beam with the plasma beam. The signal of the reference beam and the plasma beams are captured by a detector array of liquid He cooled $InSb$ bolometers installed at the top of TCV. The linear densities measured by the FIR interferometer are sampled at rate $t = 50$ μs with an accuracy of about 1%.

FIR measurements are not local and it is necessary to carry out an inversion procedure which can introduce significant uncertainties in the resulting profiles. Several techniques of resolving the inverse problem have been developed so far [32–35]. One of these methods, the SVD-I method [35], is now routinely used in TCV to invert line integrated data. The SVD-I method is based on singular value decomposition of the Thomson scattering density profiles for obtaining the base functions for FIR signals inversion. It provides electron density profiles which are in good agreement with the profiles obtained from the local TS scattering measurements [35].

2.2.3   Soft x-ray tomography
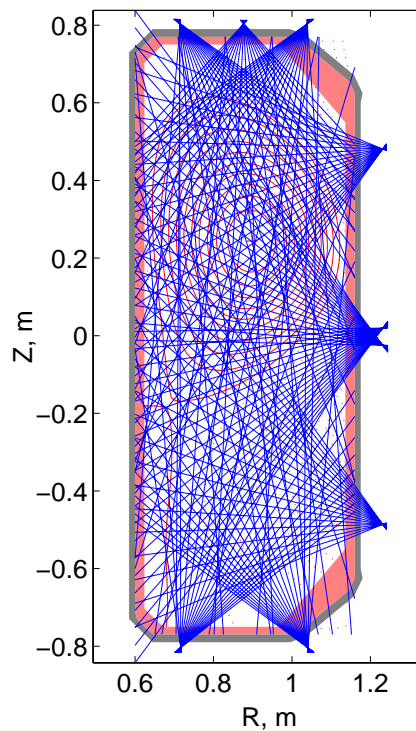
Figure 2.5: *View of experimental setup of the TCV soft x-ray tomographic system.*

The soft x-ray tomographic system consists of 10 linear detector arrays, each equipped with one strip of 20 Silicon diodes and a beryllium absorbtion foil of 47 μm thickness in front of each array. The arrays are distributed in 9 ports of a single poloidal sector to give a full poloidal coverage (Fig. 2.5). The resulting 200 lines of sight are used to perform a tomographic reconstruction with spatial resolution of 3-4 cm and with temporal resolution

limited to 80 kHz for virtually all possible plasma configurations on TCV [36].

The local x-ray emissivity is a strong function of the electron temperature, the electron density and the impurity mixture. Therefore, the measured x-ray signals are sensitive, for example, to the presence of MHD-instabilities. In the particular case of sawtooth oscillations, analysis of the emissivities by the method of singular value decomposition [37] yields the geometric location of the sawtooth inversion radius or, equivalently, the $q = 1$ surface. In conjunction with measurements of electron densities and temperature profiles, the local x-ray emissivities are used to obtain local values of intrinsic impurity density and concentrations or alternately of the effective charge Z_{eff} by the method described in [38].

2.3 The JET tokamak

The Joint European Torus (JET) located at Culham in the United Kingdom is at present the largest tokamak in the world. It has been built and is being operated through the collaborative effort of European Union plus Switzerland. JET is designed for investigations of heating and confinement in reactor relevant plasma conditions, the investigation of plasma-wall interactions and for the study of α-particle production, confinement and consequent plasma heating.

In 1997 experiments with a D - T fuel mix produced a record DT fusion power of 16.1 MW during 1 s, with a total heating power of 25.4 MW which included neutral beam heating (22.3 MW) together with hydrogen minority ion-cyclotron resonance heating (3.1 MW) [39]. The plasma attained $n_{D+T}(0)T_i(0)\tau_E = 8.7 \cdot 10^{20}$ $m^{-3}keV s$ and a total stored energy of 17 MJ, the highest of any experiments to date. Clear evidence of electron heating by α-particles was also obtained [40].

The main parameters of JET are presented in the Table 2.2. JET is equipped with a neutral beam injection (NBI) heating system, ion cyclotron heating (ICRH) and a lower hybrid radio frequency heating (LH) systems. A long pulse ($\simeq 10$ s) neutral beam (NBI) injector with eight beam sources, able to inject D and H beams with particle energies up to 120 keV providing a total power currently exceeding 20 MW [41]. The four antenna JET ICRH system has been designed for operation in a wide frequency

Parameters	Value
Major radius	2.96 m
Minor radius vertical	2.10 m
Minor radius horizontal	1.25 m
Aspect ratio	~ 0.35
Maximum plasma current	< 6 MA
Additional heating power	$25MW$
Plasma elongation	1.6
Discharge duration	20 s

Table 2.2: *Main parameters of JET tokamak*

range (23-56 MHz) and can deliver up to 12 MW of the power to the plasma in L-mode, but is limited to 5 MW in most H-modes due to the coupling differences in the presence of edge localized modes [42, 43]. The radio frequency power is used to excite a fast magnetosonic wave, to which the high density plasma core is accessible. The wave is absorbed at a cyclotron resonance which is positioned in major radius by the choice of magnetic field and RF frequency. ICRH has an ability to control the power deposition in localized and predetermined regions and to effectively couple power to the plasma ions and electrons. Power deposition profiles are calculated using code PION. The PION code is a time dependent code which calculates the ICRH power deposition and the velocity distribution function of the resonating ions. In order to take into account the influence of the beam particles on the ICRH power deposition, the NBI source term [44] is included in PION [45]. The 3.70 GHz LHCD system is capable of launching 4 MW of the power for 20 s [46]. The system is suitable for a non-inductive lower hybrid current drive (LHCD). LHCD has been used for current profile control in several experiments [47] where the LH waves have proven to be effective for establishing radial profiles of the plasma current with flat or even reversed safety factor profiles $q(r)$, which are suitable for improving the energy confinement in tokamaks [48–50].

2.4 The main JET diagnostics

A wide range of diagnostics specially adapted for the large physical dimensions, tritium compatibility and a remote handling is employed on JET. The electron density profiles in JET are measured with multichannel far infra-red (FIR) interferometry [51] and LIDAR Thomson scattering system [52]. Electron temperature profiles are measured with LIDAR TS scattering [52] and with a 48 channel heterodyne ECE radiometer [53]. Impurity ion densities in JET are obtained from the data of various passive spectroscopic diagnostics in the visible, VUV and XUV regions of the spectrum and from active Charge Exchange Resonance spectroscopy (CXRS) which uses the heating neutral beams [54]. The CXRS method is used to measure ion temperature and rotation profiles by using an array of viewing chords intersecting the neutral beam. Radial profiles of the effective ion charge Z_{eff}, are determined from measurements of the visible Bremsstrahlung and from simultaneous measurements of the main light impurities by CXRS.

2.4.1 JET LIDAR Thomson scattering

The JET LIDAR Thomson scattering system has a practically horizontal line of sight at the midplane as in Fig. 2.6 [52]. By the principle of Thomson scattering the backscattered light spectrum is generated by a short laser pulse (250 ps duration) and following analysis of the width and intensity of the scattered spectrum, yields the electron temperature and density in the usual way [29]. By the time of flight or LIDAR (Light Detection and Ranging) principle, the position of the laser pulse within the plasma is also known at any instant [55] and leads to knowledge of both electron temperature and density as a function of radial position. The backscattered light is collected by 8 spectrometers installed on the 'roof laboratory' above the Torus Hall ceiling. The time resolution is provided by successive pulses at 4 Hz frequency. The spatial resolution of about 9 cm the system is limited by the finite pulse width of the laser and the response time of the detection system.

The accuracy of the resulting electron temperature and electron density measurements along the line of sight are usually in the order of 10 %. The profile mapped on $\rho = \sqrt{\psi}$
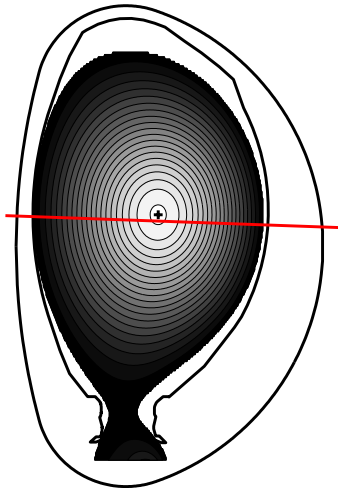
Figure 2.6: *The geometry of the JET LIDAR TS system together with vessel contours and contours of magnetic surfaces for particular shot*

grid, where ψ is a poloidal flux, is obtained using the equilibrium code EFIT [56].

2.4.2   JET FIR interferometer
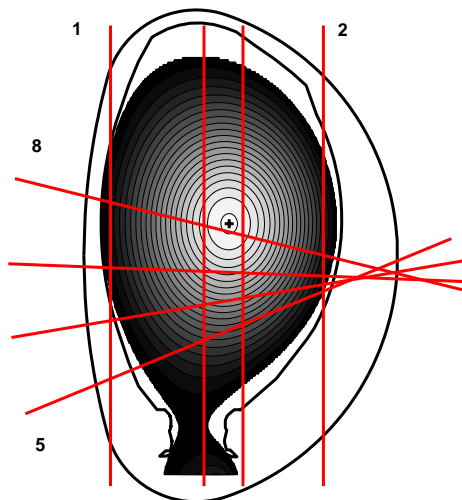
Figure 2.7: *The geometry of the 8 channel JET FIR interferometer system, together with the vessel contours and contours of magnetic surfaces for a particular shot*

A 8 channel JET FIR interferometer is build using the heterodyne Mach-Zehnder scheme [51]. The Fig. 2.7 shows the arrangement of the 4 vertical and 4 horizontal chords of the system. The source for the interferometer is a deuterated hydrocyanic acid laser with a maximum power of 250 mW. The signal of the laser beam after the plasma is

captured by liquid He-cooled InSb crystal detectors.

The FIR system is equipped with a compensating interferometer which is used to correct the effect of vibrations of the torus wall. The normal level of accuracy of the line-integrated electron density is determined by the resolution of the phase measurement. The design provides an accuracy of about $1/20$ of a fringe, corresponding to about $5 \cdot 10^{17}$ m^{-2} in terms of measured electron density.

The signals from FIR interferometer chords are used for polarimetric measurements of the Faraday rotation in order to determine plasma current densities and profiles of safety factor q [47, 57].

2.5   JET density profile inversion

The local character of Thomson scattering measurements is an advantage over the FIR line integrated measurements. However, the limited time resolution, which yields only about 150 density profiles for the 20-30 s JET discharge, does not allow to analyze fast transport phenomena. The presence of parasitic light and necessity of a calibration of the Thomson scattering system can limit the accuracy of the measurements. On the contrary, the FIR measurements provide the data for density reconstruction with high time resolution and accuracy, but the problem of inverting the line integrated measurements taken using a limited number of chords remains an issue in density profile reconstruction despite the fact that several techniques have been proposed [32–35]. In the following sections we will present the analysis and will show the limitations of the JET electron density profile data obtained using Thomson scattering and the existing simple methods of FIR inversion. To improve the quality of density profiles we propose two alternative methods for line integrated data reconstruction. The first method is an inversion which uses localized base functions and the second method uses a set of base functions derived from LIDAR density profiles by means of singular value decomposition (SVD) analysis.

2.5.1   Electron density profiles in JET

A detailed study of profiles, obtained with the LIDAR system on JET, reveals significant inaccuracies of the measurements of the density near the plasma edge. An example of
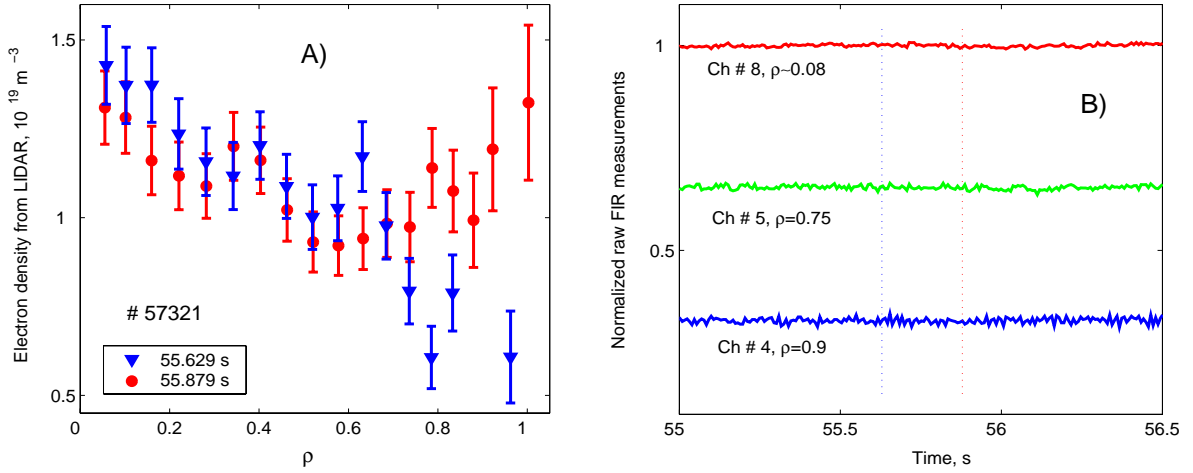
Figure 2.8: **A)** *Two consecutive profiles of the electron density obtained by LIDAR system and mapped on ρ_{pol} grid.* **B)** *Time traces of three channels of FIR interferometer normalized on the value of channel #8 at 55 s. The parameter ρ is the impact factor corresponding to the shortest distance of the chord to plasma centre on $\sqrt{\Psi/\Psi_{LCFS}}$ coordinate. Two vertical dashed lines indicate the times of LIDAR measurements for the profiles presented on the left figure.*

LIDAR measurements in a particular discharge is presented in Fig. 2.8. Two consecutive profiles of the electron density taken in a quiescent phase of the discharge and mapped on ρ_{pol} grid are seen to be very different. The overall changes in the measured density at $\rho \sim 0.9$ in a time frame of 50 ms exceeds a factor of 2, well outside the error bars. Moreover starting from $\rho_{pol} \sim 0.7$ the later profile (red circles) has a positive density gradient in the absence of any discharge feeding by a gas puff or pellets. This behaviour of the density is not compatible with the measurements of the line integrated density presented on Fig. 2.8 on the right. Indeed, the time traces of the line density integral measured by FIR at the corresponding time, indicated by vertical dashed lines, show no variations. This discrepancy between LIDAR and FIR measurements indicates a failure of the LIDAR measurements for later profile.

The erratic appearance of positive density gradients at the profile edge in numerous analyzed discharged indicates that an absolute calibration of the LIDAR system cannot explain the incorrect measurements. Possible errors in the equilibrium reconstruction influencing the mapping of the profiles cannot be an origin of sudden rise of the edge values, since both profiles on Fig. 2.8 were reconstructed using practically identical equilibria

taken in a quiescent plasma. One of the reasons of such behaviour of the measurements may be the parasitic light, however the source of this light is unknown.

To perform a broad study of the measurement inconsistency we compared FIR and LIDAR data over a database of about 400 samples taken in different plasma conditions. Profiles of the density on equilibrium ρ_{pol} grid were obtained using a cubic spline interpolation with constraints on the second derivative of the profile. The resulting profiles were remapped to the FIR chords and integrated along them in order to obtain linear integrated density $n_{lin}^{LIDAR}(i)\ m^{-2}$, a quantity which can be directly compared to the raw FIR signals. In order to account for possible errors of the absolute calibration of the LIDAR, all integrated LIDAR data for each sample were corrected using a coefficient $k = n_{lin}^{LIDAR}(8)/n_{lin}^{FIR}(8)$ calculated using the LIDAR profile integral and raw data of FIR chord No. 8, passing closest to the plasma centre. We took care to exclude any samples with FIR fringe jumps from this comparison.

A histogram reflecting the distribution of the ratio of LIDAR and FIR signals for four chords is presented on Fig. 2.9. To each chord we attributed an impact parameter ρ_{imp} which is equal to the shortest distance from chord to plasma centre on the $\rho_{pol} = \sqrt{\Psi/\Psi_{LCFS}}$ coordinate.

From Fig. 2.9A-C it is seen that distributions of the ratios are nearly Gaussian for ρ_{imp} up to 0.75. As the impact parameter ρ_{imp} increases the distribution of the LIDAR/FIR ratios becomes broader with the standard deviation $\sqrt{\chi^2}$ reaching 0.1 for chord # 5. More importantly, we observe a gradual displacement of maximum of the distribution, reaching 10 % for $\rho_{imp} \sim 0.75$. This deviation from the FIR measurements indicates a systematic flattening of the LIDAR profile. The distribution of the ratio obtained along the chord # 4 (Fig. 2.9D) which correspond to the measurement of plasma edge is not Gaussian since is visibly deformed to the high values side. The difference between LIDAR and FIR measurements for this chord can be as high as factor 3 and those cases corresponds to the clear effects of LIDAR malfunctioning presented on the Fig. 2.8. At the same time the ratios in the centre of the distribution correspond to the profiles which do not have positive gradient or any other particularity which would clearly indicate a problem with the measurements. However, those LIDAR profiles are also broader than FIR profiles
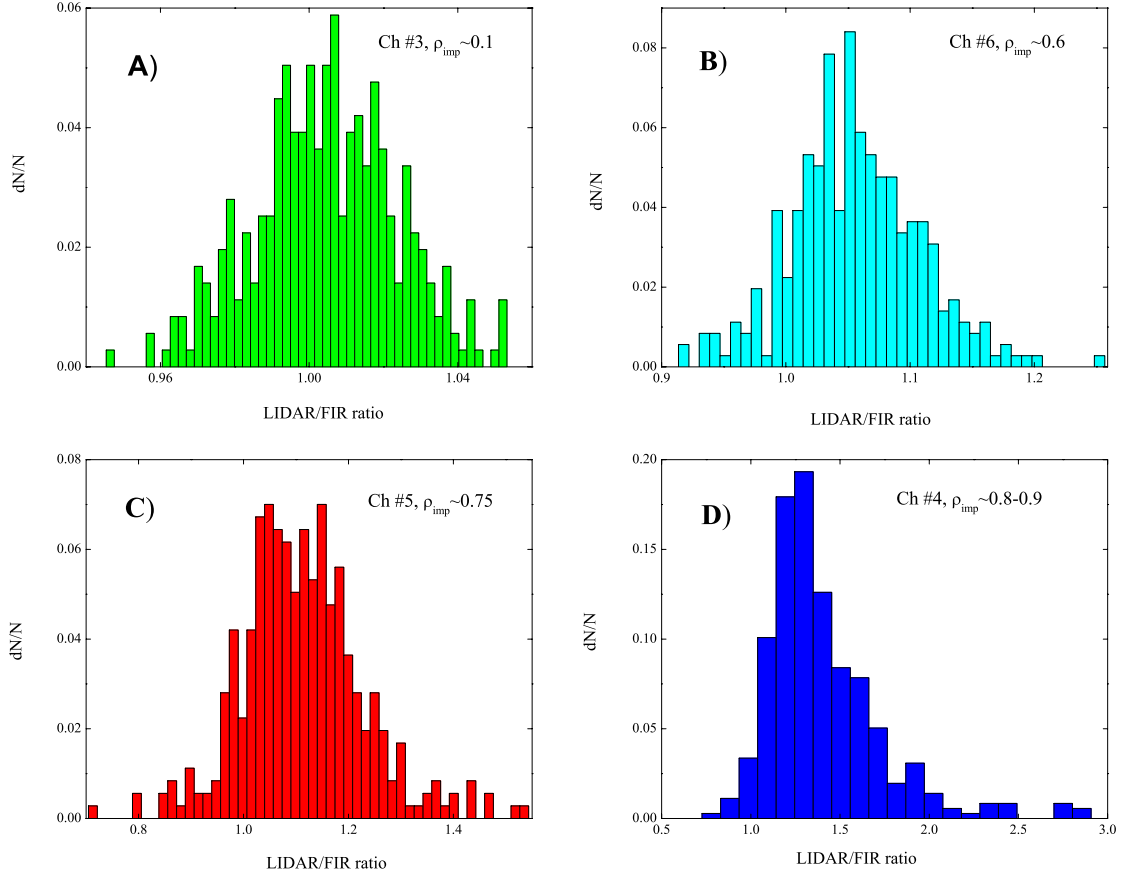
Figure 2.9: *Distribution of the ratios $n_{lin}^{LIDAR}(i)/n_{lin}^{FIR}(i)$, where i is FIR chord number, over the 400 samples.*

because the mean value of the distribution is displaced by nearly 30%. This additional flattening could have the same origin as the sudden rise of the edge values of the density shown in Fig. 2.8.

The LIDAR's malfunctioning and noise of the edge LIDAR channels makes alternative measurements of the density profiles crucial for reliable transport analysis. JET is not equipped with any other (than FIR and LIDAR) diagnostic for electron density measurements therefore the only alternative to LIDAR is to make use of the integrated FIR measurements. Reconstructions can be performed using different methods and, since the number of chord is limited (eight), all those methods have to assume the electron density to be constant on the flux surfaces. The dependence of the density only on the flux coordinate applicable in the absence of strong magnetohydrodynamic activity reduces the number of degrees of freedom and simplifies the inversion problem.

Parametric reconstructions using predefined polynomial functions on flux surfaces with free parameters represents the approach used routinely on JET to derive the profile of the density. As an illustration we present here the approaches in JET, having processed pulse file nodes NET and NEX. The first uses a polynomial approximation to density profile with three free parameters:

$$n(\rho) = n_w + n_0 \cdot (1 - x^2)^\gamma$$

where n_0 and n_w are the central and wall density respectively and $x = \sqrt{\Psi/\Psi_{LCFS}}$. The second uses the polynomial approximation of the profile in the bulk in the form:

$$n_e(x) = (1 - x^2)(Q(1 + x^2 + 4x^4) + P(1 - 2x^2 + x^4)$$

where the free parameters are P, Q and x is $x = \sqrt{\Psi/\Psi_{LCFS}}$. $Q(1 + x^2 + 4x^4)$ represents a "hollow" profile whilst $P(1 - 2x^2 + x^4)$ represents a "peaked" profile. In both cases NET and NEX free parameters are found by means of minimization in least squares sense of the discrepancy between the raw measurement and signals obtained from polynomial approximation.

It was found that both methods give reliable results only in very limited range of discharge conditions. For example NET very often fails to reconstruct the density profile in the case of Ohmic L - mode discharges giving the profiles which are much flatter than those observed by LIDAR. In the case of H - mode discharges both methods, in most cases, give non physical strong hollow profiles or even profiles with negative values at the centre for the case of NEX or constant over ρ_{pol} density ($\gamma = 0$) for the case of NET. These observations reinforce the strong suspicion that no general and physically justifiable functional form exist for fitting the variety of electron density profiles in tokamak plasmas.

Summarizing the data analysis, we can conclude that neither measurements of density by LIDAR system nor simple polynomial reconstruction of the FIR signals can provide reliable density profiles.

2.5.2   Electron density profile reconstruction

The principle of reconstruction proposed here consists of an approximation of the density by a weighted sum of base functions $f_i(\rho, t)$ $(i = 1 \ldots K)$ defined on flux surfaces:

$$n_e(\rho, t) = \sum_{i=1}^{K} a_i(t) f_i(\rho, t) \tag{2.1}$$

with corresponding weight coefficients $a_i(t)$ satisfying the following:

$$N_l(t) = \sum_{i=1}^{K} a_i(t) \int_l f_i(\rho, t) d\rho \tag{2.2}$$

where l indexes the interferometer chords, i indexes the base functions and $N_l(t)$ represents the interferometer measurements for chord l. Integrals of the base functions along the chords in the sum 2.2 are evaluated numerically using the plasma equilibrium.

In the case when the number of base functions is equal to the number of chords the inversion is a straight forward inversion of the matrix $M_{il}(t) = \int_l f_i(\rho, t) d\rho$ giving the set of coefficients $a_i(t) = M^{-1}(t) N_l(t)$. When the number of base functions is less than the number of chords, the inversion consists in solving for each time point and in a least squares sense, the overdetermined set of equations 2.2.

In general any set of base functions can be chosen. The simplest choice for f is such that n_e is continuous and is a polynomial of degree $<= 1$ on each interval $[\rho_i, \rho_{i+1}]$ where $0 = \rho_0 < \rho_1 < \rho_2 \ldots < \rho_{K-1} < \rho_K = 1$ are $(K + 1)$ points chosen in the interval $[0, 1]$. The functions f_i becomes a hat element defined as follows:

for $i = 1, 2, \ldots, K - 1$

$$
\begin{aligned}
f_i(\rho) &= 0, & \rho &\notin [\rho_{i-1}, \rho_{i+1}], \\
f_i(\rho) &= (\rho - \rho_{i-1})/(\rho_i - \rho_{i-1}), & \rho &\in [\rho_{i-1}, \rho_i], \\
f_i(\rho) &= (\rho_{i+1} - \rho)/(\rho_{i+1} - \rho_i), & \rho &\in [\rho_i, \rho_{i+1}],
\end{aligned}
\tag{2.3}
$$

and for $i = 0$ and $i = K$

$$
\begin{aligned}
f_i(\rho) &= 0, & \rho &\notin [\rho_0, \rho_1] \text{ or } \rho \notin [\rho_{K-1}, \rho_K] \\
f_i(\rho) &= (\rho - \rho_{K-1})/(\rho_K - \rho_{K-1}), & \rho &\in [\rho_{K-1}, \rho_K], \\
f_i(\rho) &= (\rho_1 - \rho)/(\rho_1 - \rho_0), & \rho &\in [\rho_0, \rho_1],
\end{aligned}
$$

In this set of localized base functions (further referred as LBF) the zeros of each function correspond to the maximum of function in neighbouring interval. Consequently the sum of the base functions at any point of the grid will be equal to 1 providing the continuity of the reconstructed profile. The main advantage of the above choice of base functions is that it makes no further assumptions on the density profiles and it is therefore applicable to a large variety of situations. Nevertheless, practical applications show that inversion based on LBF (LBF-I) does not provide satisfactory results in the case of hollow density profiles or when the number of available interferometer chords is small.

To overcome this difficulty the SVD inversion (SVD-I) method based on the singular value decomposition (SVD) described in [35] was applied at JET. The principle of the SVD-I is the following. As a first step, the density profiles obtained at M ρ points by any local measurements (in our case LIDAR) for each of N time points are arranged in an $M \times N$ matrix N_e

$$N_e = \begin{pmatrix} n_e(\rho_1, t_1) & \dots & n_e(\rho_1, t_N) \\ \vdots & \dots & \vdots \\ n_e(\rho_M, t_1) & \dots & n_e(\rho_M, t_N) \end{pmatrix}$$

The SVD [37] provides a decomposition of this matrix into a product of three matrices U, V and S such that

$$N_e = U \cdot S \cdot V^T$$

of sizes $M \times M$, $M \times N$ and $N \times N$. Matrices U and V are unitary and S is diagonal with positive elements conventionally ordered in descending order such that

$$S_1 \geq S_2 \geq S_3 \geq S_k,$$

where k is equal to the rank of the data matrix N_e. The columns of U and V represent respectively spatial and temporal 'eigenvectors' (topos and chronos), while the diagonal elements, or singular values S represent their respective weights. U forms an orthonormal spatial basis on which the signal N_e is decomposed and V is its time evolution. Since the U basis diagonalizes the covariance matrix, it can be expected that it better describes the spatial features of the whole signal, compared to other possible bases chosen *a priori*. This is confirmed by the fact that, in practice, most of the singular values are very small

compared to a few dominant ones. The SVD technique is well known in the field of
digital data processing where it is used to effectively filter the noise, i.e. any feature of
one channel uncorrelated to the others.

A truncated set of spatial eigenvectors from U are taken as base functions f_i in the
Eq. 2.1 and the coefficients a_i are determined from Eq. 2.2. Note that f_i in SVD-I are
constant in time and therefore only one set of base function is used for reconstruction. The
advantage of base functions obtained using SVD is that such functions contain already
physical information about the profiles. As a result, only a few chords are needed for the
satisfactory approximation of n_e.

2.5.3 Applications

In the case of an experimental profile reconstruction only part of the complete set of FIR
chords is available for inversion. For example, in all diverted discharges the chord No 2
passing through divertor (Fig. 2.7) is not taken into account. The outmost chord No 1 is
often excluded from analysis since it is nearly tangential to LCFS and the corresponding
contributing integral is very sensitive to the equilibrium reconstruction errors.

The triangular functions (Eq. 2.3) were chosen to form the set of base functions on flux
surfaces grid. To improve the reconstruction which has to use small number of chords as
constraints, a special choice of discretization along the radius is made. The radial grid was
divided in such a way that the maximum of each base function corresponds to the defined
above impact parameter ρ_{imp} of the corresponding chord. In order to force the profile to
have zero derivative at the centre, the first base function is chosen to be trapezoidal. In
order to adopt the reconstruction to the changes of plasma geometry the base functions
were calculated for each time point of equilibrium.

In Fig. 2.10A an example of density profile reconstruction of a profile in L-mode using
localized base functions is shown. The corresponding base functions are presented in Fig.
2.10B. The number of base functions used is equal to the number of chords (constraints)
and the solution is obtained by a simple inversion of the matrix, which due to the high
signal to noise ratio of the FIR interferometer, gives good results. Since LIDAR TS data
cannot be considered as reliable to compare with, we use the profile obtained with LBF-I
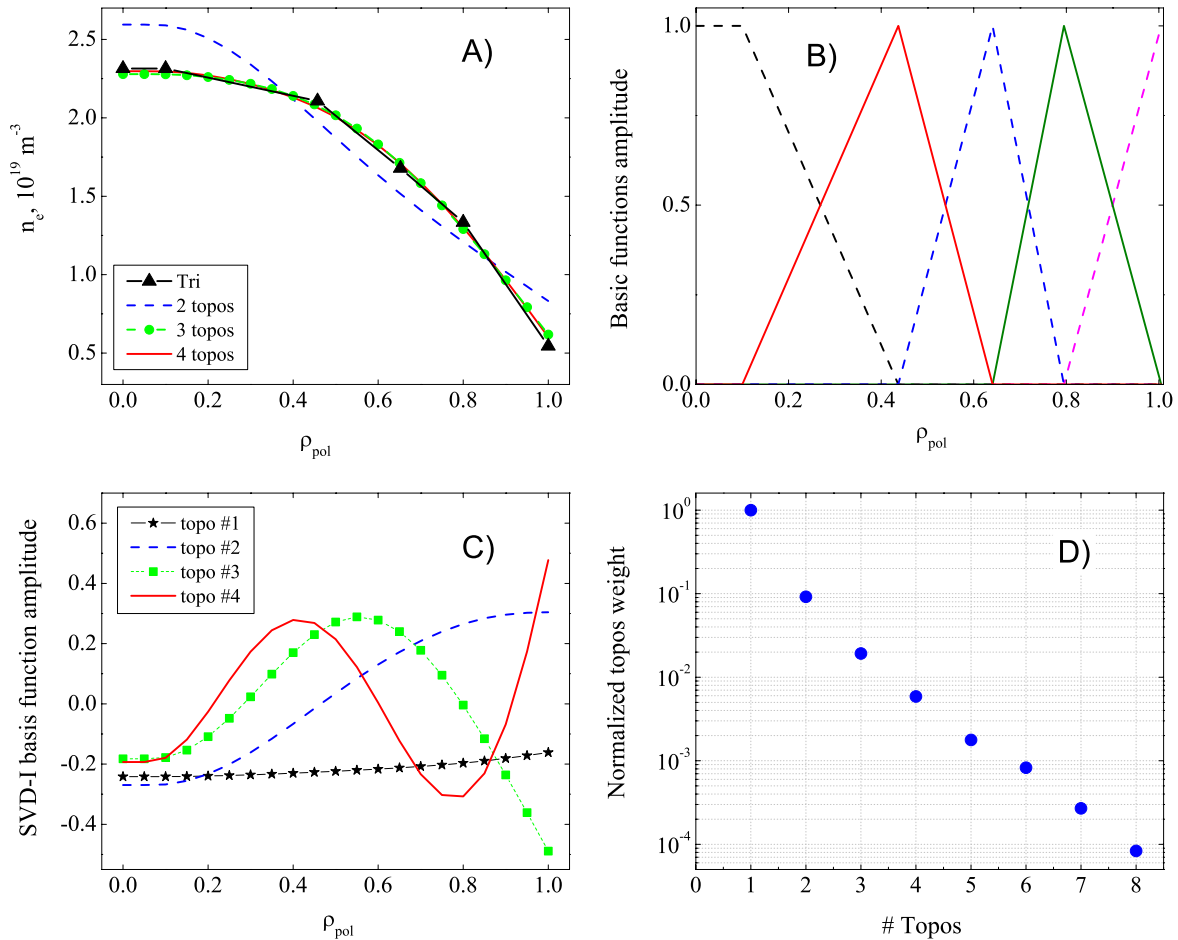
Figure 2.10: *Reconstruction of the density profile in JET discharge #57867 at time 46.8 s.* **A)** *Electron density profile reconstructed using LBF-I and SVD-I with different number of topos taken into account* **B)** *Base functions used for LBF-I.* **C)** *First four topos of SVD decomposition of LIDAR TS measurement.* **D)** *Normalized energy (diagonal elements of matrix S_k) corresponding to first eight topos*

as reference to check the accuracy of the SVD-I.

An example of a reconstruction using base functions obtained from LIDAR data using SVD is shown on Fig. 2.10A. The topos were obtained using filtered LIDAR density profiles. The filtering consisted in the removal from the matrix of the profiles with artifacts described in section 2.5.1, having a clear positive gradient at the edge. For this example, about 130 profiles form the matrix N_e, providing a coverage of different discharge phases. The resulting four topos are shown on Fig. 2.10C. For the SVD reconstruction presented, the number of base functions is smaller than the number of the chords and an overdetermined problem was resolved by least square minimization. The reconstruction
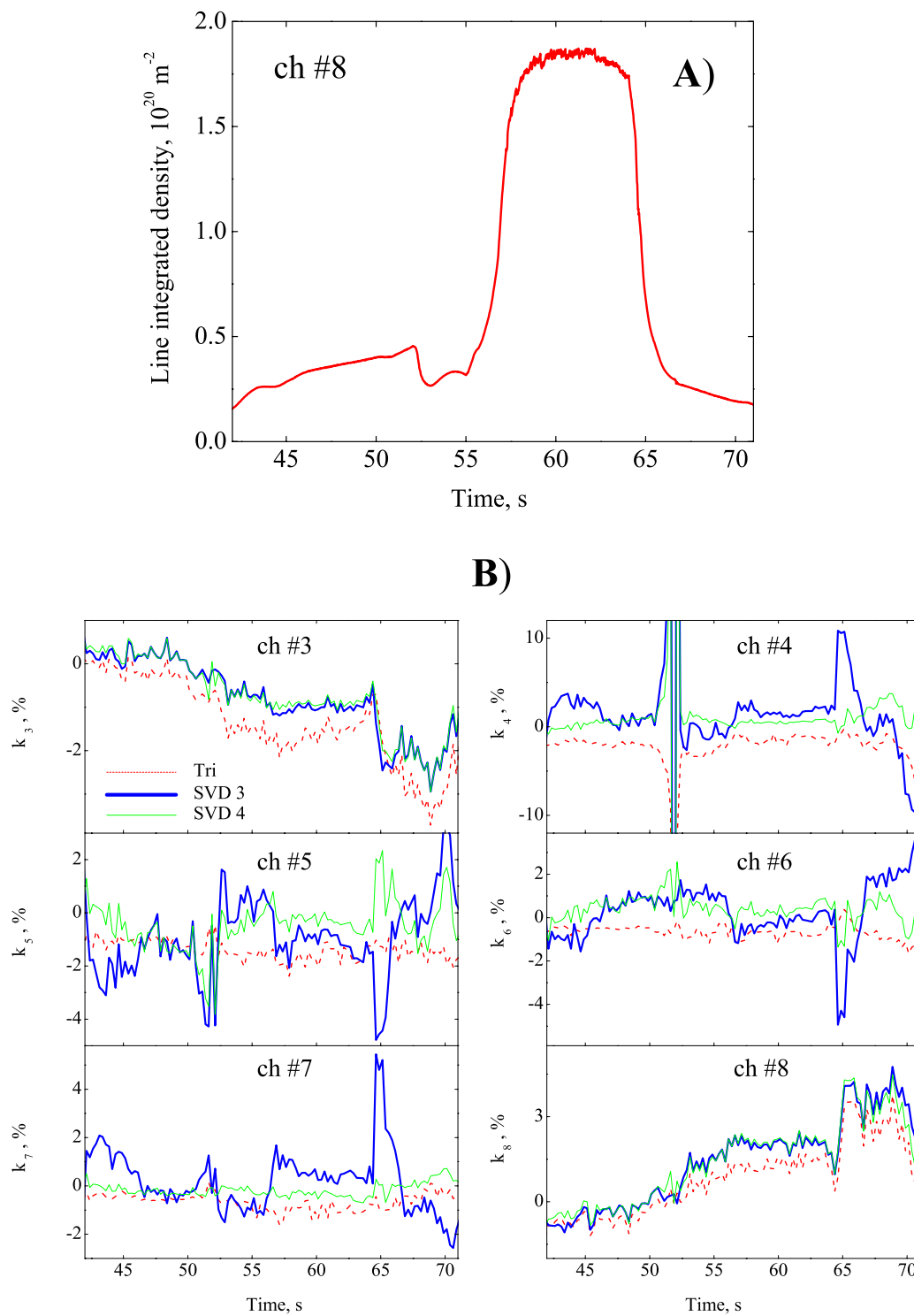
Figure 2.11: **A)** *Temporal behaviour of line integrated electron density for discharge #57867 using chord No. 8 of FIR.* **B)** *Temporal behaviour of the relative difference of the raw FIR data and line integrated density obtained using inverted profiles for chords No. 3 - 8 (see the definition of the k_i in the text)*

which uses only the first two topos give the profile rather different from reference profile. Increasing the number of topos in use up to first three leads to reconstructed profiles similar to LBF-I. Adding the fourth topos does not change the profile obtained with only three topos. The importance of each topo in the final reconstruction can be understood from the power distribution of the singular values (diagonal elements of matrix S_k). In Fig. 2.10D the power of the eight first topos, normalized to the power of first topo, is shown. For this discharge, the first four components contain together about 99.5% of the total signal energy. Hence adding more than four topos in the Eq. 2.1 would not lead to increase of valuable information in the reconstructed profile.

To prove the applicability of the method one needs to compare the line integrals along the chords of the inverted density with the raw FIR signals. We perform this analysis in the same discharge as in Fig. 2.10. The time trace of the raw signal of the central FIR chord is shown in Fig. 2.11A. The discharge starts in an L-mode limited configuration, than at about 51 s the divertor is formed. The H-mode lasts from about 55 s to 65 s and is characterized by a sharp density increase with respect to L-mode and finally, the discharge finishes in L-mode. The results of the inversion and raw data were compared using the normalized difference expressed in percent

$$k_i = 100 \cdot (\int\limits_i n_e^{inv} dl - n_{ei}^{fir})/n_{ei}^{fir}$$

where i corresponds to the chord number, n_e^{inv} to the inverted density profile and n_{ei}^{fir} is the raw FIR signal for particular chord. In Fig. 2.11B this normalized difference is plotted for SVD-I with three topos used, SVD-I with four topos used and LBF-I. For all chords except No. 4 the agreement between raw data and integrated inversion profiles is within a few % for most of the discharge duration. The maximum differences are observed during transition phases (limiter to divertor, H-mode to L-mode) where the limited time resolution of reconstruction of the equilibrium or errors in this reconstruction can affect the profile reconstruction. For example, a zero integration path for the outmost chord No. 4 with non zero FIR signal for this chord are responsible to increase of k_4. It has to be noted that such equilibrium reconstruction errors only slightly affect the reconstructed profile itself because the inversion routine excludes the edge chord from the analysis and
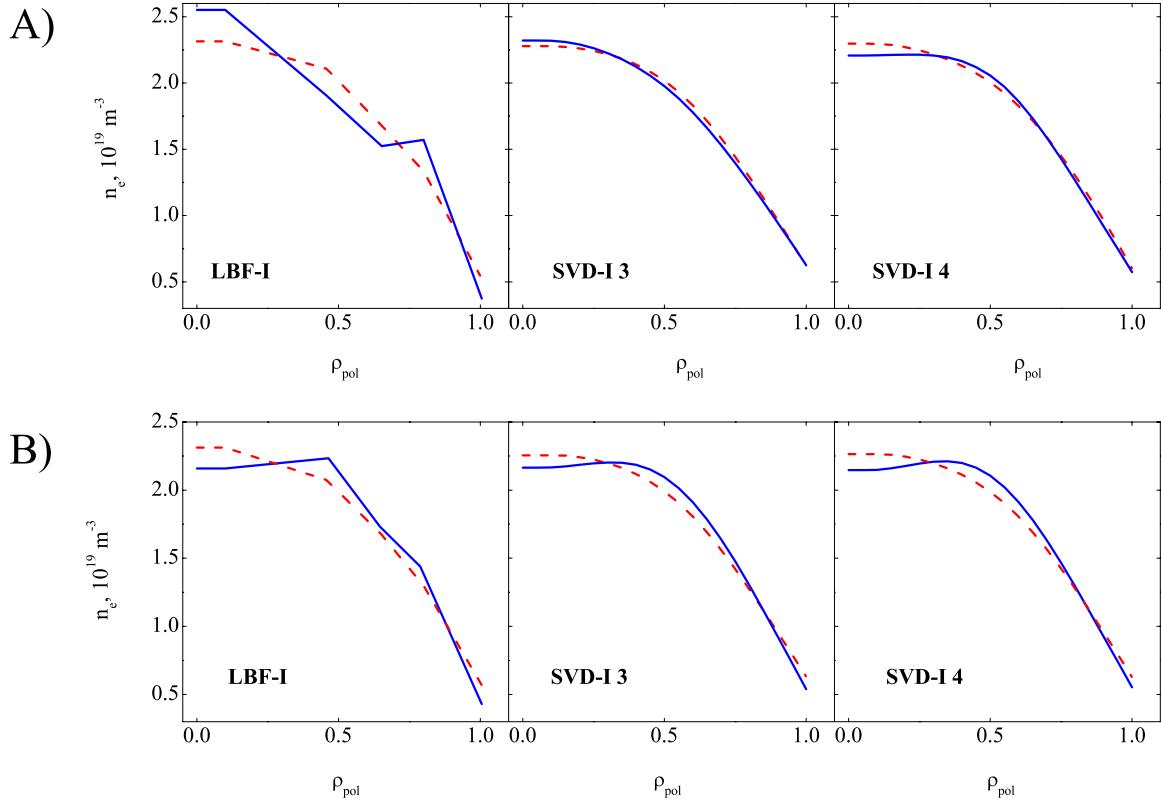
Figure 2.12: *Examples how equilibrium errors influence the reconstructed density profile in JET discharge #57867 at time 46.8 s. The dashed line corresponds to the original profiles and the solid line to the profiles calculated using the disturbed equilibrium.* **A)** *10 % random errors added to the contours of flux surfaces.* **B)** *Influence of a 10 cm Shafranov shift added to EFIT equilibrium.*

the inversion is performed using the remaining FIR channels.

The good agreement of the profile integrals with the raw FIR data and the smallness of the differences between SVD-I and LBF-I proves the applicability and reliability of the novel SVD-I method. However, the database of the local Thomson scattering profiles, from which the SVD-I base functions are derived, needs to be rich enough to contain sample profiles which are representative of all phases of the density profile evolution of interest. It is also important to note that base functions giving good reconstructions in a particular physical situation should not be expected to be suitable in different situations.

Any method of reconstruction of the FIR line integrated signals will be affected by errors in equilibrium reconstruction. In order to estimate the magnitude of the errors in the final profile we artificially added ±5% random error to the contours of each of 21

(in standard JET poloidal flux division) flux surfaces. These errors affect the integrals $\int_l f_i(\rho, t)d\rho$ along the chords and therefore add the uncertainties in the estimation of the coefficients a_k in Eq. 2.2. In practice, random errors in the equilibrium appear, for example, in the presence of macroscopic magnetohydrodynamic (MHD) activity which noticeably disturb the symmetry of the flux surfaces. It is seen from the Fig 2.12A that equilibrium errors strongly influence the LBF-I. At the same time the SVD-I seems to be less affected than the LBF-I only slightly changing when three topos are used. The SVD-I with the four topos is more susceptible to equilibrium errors than SVD-I with 3 topos but changes on the profile are significantly less pronounced than for LBF-I case. From this example we can conclude that SVD-I is more resilient to errors in equilibrium and therefore to MHD activity and gives more reliable results that LBF-I.

We also studied the influence on SVD-I and LBF-I of the systematic errors in the equilibrium reconstruction. One possible systematic error is a misestimate of a radial displacement of the centres of magnetic flux surfaces with respect to the centre of the bounding surface, the Shafranov shift, which depends on the core current and pressure profile. A comparison of the inversions performed on the EFIT equilibrium with the inversions calculated on the same base equilibrium with an artificially added 10 *cm* displacement of the flux surface centres is presented in Fig. 2.12B. Both SVD-I and LBF-I are affected by the Shafranov shift, however in contrast to the example in Fig. 2.12A the modification of SVD - I and LBF - I are very similar and therefore in this case SVD - I does not provide a considerable advantage over LBF - I. Another typical systematic error in equilibrium reconstructions leads to uncertainties in the values of central elongation. SVD-I and LBF-I found to be practically unsensitive to artificially produced changes of κ_0 from an initial value of 1.2 to 1.4 with fixed κ_{edge}. This insensitivity is related to the fact that only one vertical FIR chord (see Fig. 2.7) passing close to the centre is influenced by κ_0 changes.

2.5.4   Summary

The analysis of the electron density profiles obtained from the LIDAR TS system showed an inconsistency with the line integrated interferometric measurements. The random

occurrence of anomalous positive gradients at the edge remains unexplained. Alternative methods of obtaining density profiles on JET, based on a functional fit inversion of FIR data, were found to be unable to provide reliable results in large variety of JET discharge conditions.

Two independent methods, SVD-I (recently developed and applied on TCV) and LBF-I were successfully applied to invert interferometric measurements from JET. Both techniques provide inverted profiles which are in good agreement with raw interferometer measurements. The accuracy of reproduction of the raw interferometric data is significantly improved with respect to the functional fit techniques routinely performed on JET.

The novel method SVD-I combines the high bandwidth of interferometer systems with the spatial accuracy of Thomson scattering. The singular value decomposition of LIDAR profile measurements is used to obtain the base functions, as well as information on their relative importance in profiles. This additional information allows to optimize the number of base function used. An interesting feature of the SVD-I reconstruction is its ability to redistribute the weights of spatial eigenvectors obtained from noisy LIDAR profiles and give results very close to the LBF-I. Good agreement of SVD-I with the independent LBF-I method confirms the reliability of both methods.

The advantages of the SVD-I with respect to the LBF-I method are the decreased level of noise on the profiles and the possibility to use only a few chords (down to as few as 3 or 4 chords) since the number of base functions needed for reconstruction is usually three or four. Using SVD-I can be beneficial from the point of view of computational time, since the spatial smoothness of the base functions allows a significant reduction of the accuracy of its projection on the diagnostic chords with respect to the accuracy needed for the calculation of sharp-edged LBF-I base function projections. Another advantage of SVD-I it is lower sensitivity to the MHD activity.

Chapter 3

Theory of transport in tokamak plasmas

3.1 Introduction

In a collisionless plasma with straight magnetic field lines, particles move along helical orbits composed of a circular motion with a Larmor radius $\rho_L = mv_\perp/eB$ in the direction perpendicular to the magnetic filed and a free motion in the direction of magnetic field. In such plasma there is no perpendicular displacement of the particles from one field line to another and therefore there is no perpendicular transport. Collisions lead to the deviation of the trajectory of the particles and in the direction perpendicular to the magnetic field particles are displaced by a distance of the order of the Larmor radius ρ_L. The time step of this random walk driven by independent scattering events is the characteristic time between two collisions $1/\nu$, where the ν is collision frequency. This gives the following expression for the diffusion coefficient across the magnetic field

$$D \sim \rho_L^2 \nu \tag{3.1}$$

In the case of a fully ionized plasma ν will be the electron-ion collision frequency. This transport induced by collisions in a cylinder is called classical transport. The classical transport is very small and plasma losses associated with it would not be of concern in a magnetic confinement system.

Under the influence of the drift in the inhomogeneous magnetic field of a toroidal device, the characteristic displacement step of particles significantly exceeds the Larmor

radius. The resulting diffusion coefficient will be therefore considerably higher, than the case of straight cylinder. This theory, which takes into account the influence of the magnetic field curvature is called the neoclassical theory.

Unfortunately, the experimental results have shown that plasma confinement in toroidal systems is significantly poorer than would be expected on the basis of classical or even neoclassical diffusion. In the presence of plasma turbulence, the existence of which is known from numerous measurements, the radial transport governed by two-dimensional turbulence in the plane, perpendicular to the magnetic field is much larger than given by classical or neoclassical theory. This additional transport is called anomalous.

In the following we represent a short overview of neoclassical transport as well as different mechanisms which can lead to anomalous transport.

3.2   Particle balance equation

To describe an evolution of the plasma particle density on transport time-scales, a fluid representation is generally used. Axisymmetry is assumed and the plasma density is deemed to be constant on a flux surface over the poloidal angle. In this way a one dimensional radial transport equation for particles in the plasma bulk, the particle balance equation is written in the form

$$\frac{\partial n_e}{\partial t} = -\nabla \vec{\Gamma} + Q \qquad (3.2)$$

where $\vec{\Gamma}$ is the particle flux density and Q represents the sources and sinks due to ionization, recombination and charge exchange.

For $\vec{\Gamma}$ an ansatz with a diffusive and convective part is used and in general

$$\vec{\Gamma}(r,t) = -D(\rho)\vec{\nabla}n(\rho,t) + n(\rho,t)\vec{V}(\rho) \qquad (3.3)$$

where the proportionality coefficient for $\vec{\nabla}$ is the diffusion coefficient and V has the dimensions of a velocity and therefore is called a pinch velocity. The diffusion coefficient is positive by definition and by convention a positive V lead to an outward particle flux and a negative V to an inward convective flux.

In steady state ($\partial n_e/\partial t = 0$), if particle sources can be neglected ($Q = 0$), the particle

flux is zero and particle balance equation becomes:

$$\frac{\nabla n}{n} = \frac{\vec{V}}{D} \tag{3.4}$$

From this relation it is seen that in steady state a negative pinch velocity leads to the formation of a density profile which is peaked at the centre (negative density gradient) and a positive pinch would lead to a hollow density profile. Thus, the ratio of D and V can be easily obtained from density gradient length $L_n = n/|\nabla n|$ of the steady state profile. However, to separately determine D and V, it is necessary to perform more complex time resolved measurements of density under non stationary conditions.

3.3 Neoclassical transport

Deformation of a cylinder into an axisymmetric torus leads to a non-uniform toroidal field in the poloidal plane. The toroidal field varies roughly as $B \cong B_0(1 - \varepsilon \cos \theta)$ ($\varepsilon = r/R$ is the inverse aspect ratio), with a maximum, B_{max}, on the inside of the torus and a minimum, B_{min} on the outside. The particles with energy E and magnetic momentum $\mu = mv_\perp^2/2B$, where $mv_\perp^2/2$ is a perpendicular particle kinetic energy and B is the magnetic field, pass freely along the field line if $E > \mu B_{max}$. Those particles are called passing. The particles with $E < \mu B_{max}$ are reflected from the high magnetic field region and are trapped. The projection of the motion of the trapped particles on the poloidal cross-section is the "banana-shaped" trajectory. The existence of such banana trajectories has a profound effect on the transport, since the collisions, which scatter the electrons out of their trapped orbits displace the particle across the flux surface by the banana-orbit width. The width of the banana is approximately $q\rho_e/\varepsilon^{1/2}$ and therefore this step is larger than the Larmor radius step length ρ_L associated with classical diffusion.

The existence of trapped particles requires that the collision frequency of pitch angle scattering

$$\nu = \frac{\nu_{ei}}{\varepsilon}$$

where ν_{ei} is the electron ion collisionality and ε is the aspect ratio, is small enough to allow the trapped particles to execute many banana orbits before being collisionally de-trapped.
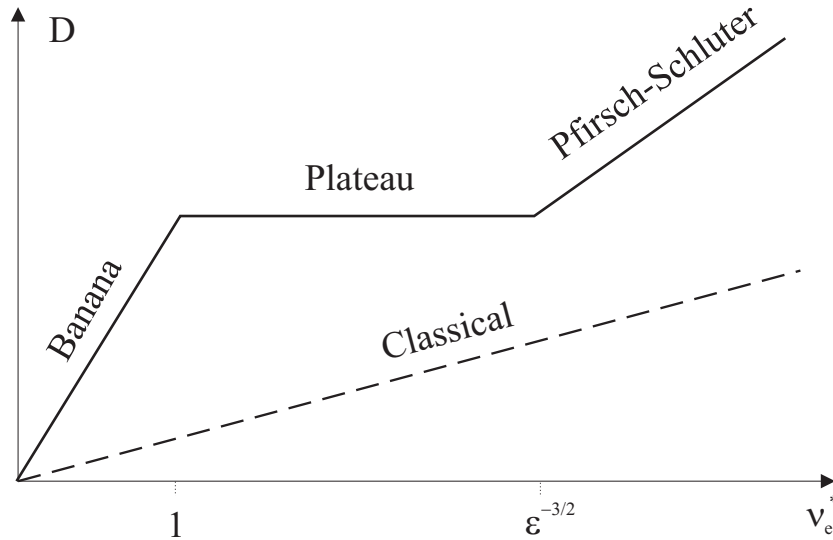
Figure 3.1: *Neoclassical prediction of variation of D with collision frequency. Dashed lines corresponds to the behaviour of classical diffusion coefficient.*

In terms of the collisionality parameter

$$\nu^* = \frac{\nu}{\omega_{be}} = \frac{\nu_{ei}qR}{\varepsilon^{3/2}v_{th}} \tag{3.5}$$

where ω_{be} the banana trajectory bounce frequency, q is the safety factor, R is the major radius and v_{th} is the thermal velocity, the basic requirement here is just $\nu^* < 1$. Particles satisfying this criterion are said to be in the "banana-regime". It has to be noted that the frequency ν_{ei} in the Eq. 3.5 is the collision frequency between electrons and ions ν_{ei}, because collisions between particles of the same species on average do not produce net diffusion. When collisions are sufficiently frequent for trapping of particles in the region of lower magnetic field to be negligible, $\nu^* > \varepsilon^{-3/2}$, particles are said to be in the Pfirsch-Schlüter regime. The intermediate regime when the trapped particles can complete many transit orbits before undergoing a Coulomb scattering is called "plateau regime".

The exact calculations of the neoclassical transport coefficient are complicated and can be found in Refs. [58–60]. In Fig. 3.1 we give only an illustrative picture of neoclassical diffusion coefficient behaviour with the collision frequency. In the banana regime when $\nu^* < 1$ the dependence of D on ν^* is linear. In the plateau regime which exists in $1 < \nu^* < \varepsilon^{3/2}$ the diffusion coefficient does not depend on collisionality. A further increase of ν^* leads to a linear increase of D on ν^* in Pfirsch-Schlüter regime. In all regimes the

values of neoclassical diffusion are higher than classical.

In addition to the increase of the diffusion coefficient, the toroidal geometry produces also a dependence of the particle flux on thermodynamic gradient forces other than density gradient. In general the neoclassical particle flux can be written as

$$\Gamma_{nc} = -D_{nc}\nabla n + n(c_{T_e}\nabla T_e + c_{T_i}\nabla T_i + c_w E_{II}) \tag{3.6}$$

The first term on the right is diffusion (see Fig. 3.1) and the terms in the brackets, according to the Eq. 3.3, represent the particle convection. The terms proportional to the gradient of the temperatures are called thermodiffusion and the radially-inward particle drift due to parallel electric field is known as Ware pinch effect [14].

The neoclassical theory predicts positive values for c_{T_e} and c_{T_i}, corresponding to inward particle pinches. However these coefficients are very small and neoclassical thermodiffusion is usually negligible.

3.3.1 Ware pinch effect

The last term in Eq. 3.6 exists only in the banana and plateau regimes and arises because the trapped particles spend unequal amounts of time in the upper and lower halves of the torus, when a toroidal electric field is present [14]. An interaction of the parallel electric field with the trapped particles in banana orbits results in incomplete cancelation of the drifts. Detailed calculations lead to the expression for Ware pinch

$$V_{Ware} = 2.44\frac{E_{II}}{B_\theta} \tag{3.7}$$

where B_θ is a poloidal magnetic field.

Varma [61,62] proposed a correction for Ware particle pinch expression, which includes the effect of charge separation in the presence of the parallel electric field. An additional θ average $E_{ad} \times B$ inward drift occurs because of the movement of the positive ions in the direction of the field and the electrons to the opposite direction, together with rotational transform, creates a polarization charge density and an electrostatic field E_{ad}. These calculations lead to a correction to V_{Ware}

$$V_{Varma} = \frac{8}{9}\varepsilon^{1/2}(1 - \varepsilon^{1/2})^{-1}V_{Ware} \tag{3.8}$$

Since there does not seem to be a theoretical consensus as for which of the two expressions Eq. 3.7 or Eq. 3.8 the most accurately describes the neoclassical pinch driven by $E_{||}$, we will discuss both in this work.

The Ware and Varma pinches involve only the trapped particles, thus to obtain the effect on the plasma as a whole, this velocity has to be corrected for the trapped particle fraction in a collisional plasma.

$$V = f_t f_\nu V_{Ware} \tag{3.9}$$

In this equation the decrease of the trapped particle towards the plasma centre due to the decreasing magnetic mirror ratio is accounted for by [63]

$$f_t = 1 - \frac{(1-\varepsilon)^2}{(1+1.46\sqrt{\varepsilon})\sqrt{1-\varepsilon^2}}$$

and the modification of the pinch profile due to the collisionality by [64]

$$f_\nu = \frac{1}{1 + \sqrt{\nu^*} + 0.25\nu^*/Z_{eff}^2}.$$

3.4 Anomalous transport

It is generally accepted that the experimentally observed level of transport in tokamak is due to instabilities and fluctuations of electric potential and magnetic field inherent to the plasma. In accordance to the scale of instabilities they may be roughly categorized in two classes: macroscopic and microscopic. The first class involves the physical displacement of plasma on the scale much larger than Larmor radius and may be therefore described by magnetohydrodynamic equations. Microscopic instabilities are caused by small fluctuations of the electric or magnetic field which lead to a small fluctuations in the particle's velocity and radial position, enhancing the characteristic length of radial particle displacement and leading to anomalous particle and energy transport.

3.4.1 Macroinstabilities

An anomalously high level of particle transport may be associated with the excitation of various large scale MHD instabilities: ideal and resistive ballooning modes, kink instabilities and tearing modes [4]. Some of these instabilities rarely occur in tokamak plasmas,

other are easily destabilised and present in a wide range of operating conditions. In the following we introduce only the sawtooth and edge localised mode instabilities, which are macroinstabilities often present in tokamak plasmas and strongly influence particle and heat transport.

Tokamaks are often subject to sawtooth instabilities in the centre of the plasma. This instability is characterized by relaxations with a fast collapse or crash of the central plasma pressure followed by a gradual build-up phase. The presence of sawteeth is an important energy loss channel from the central region. Although the sawtooth instability has long been observed and studied in tokamaks, the understanding of the underlying physical mechanism is still incomplete. Existing models assume that an $m = 1$, $n = 1$ resistive internal mode is unstable for $q_0 < 1$ (m and n are the poloidal and toroidal mode numbers and q is the safety factor at the magnetic axis) [65–67]. The sawtooth crash is a result of magnetic reconnection of an $m = 1$ island formed inside the $q = 1$ surface. The instability is triggered when the current profile peaks and q becomes smaller than 1, flattening the current profile such that $q = 1$ after the crash. During the sawtooth crash a large scale convective motion creates enhanced transport within the central region, causing the flattening of the temperature and density profiles up to so-called the mixing radius. Recover of the profiles takes place by a diffusive process on a slower timescale. Outside the inversion radius, r_{inv}, the effect of sawtooth crash manifests itself as a heat and particle pulse propagating outwards.

The improved confinement regime known as the H-mode is often perturbed by quasi-periodic series of relaxation oscillations involving bursts of MHD activity and emission, known as edge localised modes (ELMs). ELMs results in a rapid (< 1 ms) losses of particles and energy from the region near the plasma boundary, reducing the average global energy confinement by 10-20%. A positive effect of these relaxation oscillations is that they allow quasi-stationary operating conditions to be obtained. Despite the fact that numerous model for ELMs have been proposed, the fundamental mechanisms behind the phenomenon is not yet known [68, 69].

3.4.2   Microinstabilities

Microinstabilities are characterized by wavelengths of the order of a few ion Larmor radii. Approximating an average plasma particle displacement, caused by microinstabilities, with typical perpendicular wavelength of the unstable spectrum $1/k_\perp$ and characteristic time with the linear growth period $1/\gamma$ one can obtain an estimate of the diffusion coefficient:

$$D \simeq \gamma/k_\perp^2$$

Depending on the growth rate γ, the resulting diffusion coefficient can be significantly larger than the neoclassical value. In addition, depending on the type of the instability, a inward or outward convection can appear.

A particularly important class of microinstabilities, called drift instabilities, occur as a result of destabilization of drift waves. Drift waves exist as a result of small fluctuations of the electric field together with density and/or temperature gradients. When the electrons and ions are driven out of phase by dissipative processes, such as collisions or wave particle resonances, the particles can transfer energy to the waves and can cause them to grow. The presence of trapped particles has an essential influence on the development of drift instabilities. This is due to the fact that passing and trapped particles react quite differently to low-frequency oscillations of potential with small phase velocities.

One of the most important drift instabilities that results from passing particle dynamics is the ion temperature gradient (ITG) mode. The ITG mode is a drift wave driven by an ion pressure gradient and destabilized by the coupling with the parallel transit drift in the unfavourable magnetic curvature. The parameter

$$\eta_i \equiv \frac{d \ln T_i}{d \ln n_i}$$

plays a crucial role in the stability of ITG mode. The threshold of the stability is defined by η_{icrit} and its predicted value depends on the logarithmic density gradient, on the ratio of electron to ion temperatures, on the effects associated with a magnetic shear or with a presence of impurities [70–74]. Trapped electron modes (TEM) are basically drift waves that are destabilized by an electron temperature gradient in the presence of a population

of trapped electrons. The threshold for TEM is a critical value of $-R\nabla T_e/T_e$ which depends on density gradient and on the fraction of trapped particles.

The importance of collisionality results from the fact that trapped and passing particles behave differently in the electrostatic potential perturbation. When the mode frequency ω_{De}, exceeds the particle collision frequency, trapping can be neglected for that species. For example, some fluid calculations predict a disappearance of convective fluxes and a flattening of the density profiles for effective collisionalities defined for drift wave instabilities

$$\nu_{eff} = \frac{\nu_{ei}}{\omega_{De}} \sim 3 \left(\frac{m_i}{m_e}\right)^{1/2} \frac{\varepsilon^{3/2}\nu_{ei}^*}{q} \sim 10^{-14} \frac{n_e R Z_{eff}}{T_e^2} \geq 1 \qquad (3.10)$$

where ω_{De} is the curvature drift frequency [26], Z_{eff} is the effective charge, R is the major radius and T_e is the temperature in eV.

Electrostatic drift waves destabilised by trapped particles and ion temperature gradient modes are prime candidates for explaining the observations of anomalous particle transport. However, in some situations the contribution of magnetic fluctuations such as MHD instabilities with high poloidal mode number which results in small scale magnetic island (for example microtearing) appears to be evident [75]. It is likely that different physical situations occur in different regions of a discharge and several instabilities magnetic and electrostatic may additively account for the experimental phenomenology across the plasma cross section.

3.5 Anomalous convective processes

We can distinguish between two lines of theoretical investigation of anomalous convective processes, which have led to testable predictions on the characteristics of the density profile. The first of these, referred to as turbulent equipartition (TEP) theories, is based on single particle invariants of motion and aims at predicting the general features of the plasma profiles resulting from turbulent driftwave transport within the frame of kinetic theory, while making a minimum number of assumptions on the nature of the underlying instabilities [16–20]. The second line is represented by a range of fluid turbulence models [22–26], which make predictions on both heat and particle transport.

3.5.1   Turbulent Equipartition

Turbulent equipartition (TEP) assumes the conservation of the second adiabatic invariant

$$J = \oint \sqrt{E - \mu B} dl$$

(where E is the particle kinetic energy, B is the magnetic field and μ is the usual first adiabatic invariant) during turbulent transport [16]. As a result of this assumption, particles distribute themselves evenly over the poloidal flux, i.e. $\partial N / \partial \Psi = const$, where N is the total number of particles within a given flux surface. This relaxed profile is closely related to the boundary (marginal) stability, when the further relaxation of the equilibrium state is no longer possible because of the vanishing of the growth rate.

The first TEP predictions by Yankov et al [16,17] conjectured that the electron density profile should be approximately given by

$$\frac{n_e(r)}{n_e(0)} \approx \frac{q(0)}{q(r)} \tag{3.11}$$

Isichenko et al [18] recognized that trapped electrons are most likely to be subject to transport driven by low frequency driftwave turbulence, such as that produced by ion temperature gradient instabilities (ITG) and trapped electron instabilities (TEM) and consequently restricted TEP to trapped electrons. The resulting profiles are broader and are approximated by [18]

$$\frac{n_e(r)}{n_e(0)} \approx \left\{ 1 - \frac{4}{3R_0} \int\limits_0^r \left(\frac{d\ln q}{d\ln r} + \frac{3}{8} \right) dr' \right\} \tag{3.12}$$

for circular cross sections. This expression is also recovered in fluid theory [22].

The two conflicting early predictions were reconciled by Baker et al [19,20], who investigated TEP under the assumption that turbulent transport is pitch angle dependent. The prediction of Eq. 3.11 appears as a limiting case when passing and trapped electrons are transported equally, whilst Eq. 3.12 is appropriate when only trapped particles undergo turbulent transport. Unfortunately, this theory introduces the pitch angle dependence of transport as a free parameter. It has, however, been suggested that profiles described by Eq. 3.11 may be characteristic of plasmas dominated by dissipative trapped electron

modes, whilst those described by equation Eq. 3.12 may relate to ITG-dominated turbulent plasmas, with the general possibility of mixed turbulence, giving rise to density profiles intermediate to those given by the above equations [76]. As shown in Ref. [19,20], this give rise to a family of density profiles, which for convenience can be approximated by

$$\frac{n_e(r)}{n_e(0)} \approx \left[\frac{q(0)}{q(r)}\right]^{\eta} \tag{3.13}$$

with $0.3 \leq \eta \leq 1$, where $\eta \simeq 0.3$ roughly corresponds to Eq. 3.12.

3.5.2 Thermodiffusion

Quasilinear calculations for electrostatic turbulence in tokamaks [21] show that the diffusion coefficient in phase space decreases with the energy, and as a consequence, particle inward convection occurs. Anomalous thermodiffusion is expected to lead to a steady state density gradient, which, in source free regions and in the absence of other pinch mechanisms, are proportional to the temperature gradient, such that

$$\frac{\nabla n}{n} = \alpha \frac{\nabla T}{T} \tag{3.14}$$

The values and sign of α depend on the type and strength of electrostatic turbulence assumed to be responsible for anomalous thermodiffusion [21, 23, 26].

Predictions for thermodiffusion appear to be more model dependent, as well as dependent on plasma conditions, such as the ratio of electron temperature to ion temperature and the nature of the underlying instabilities (ITG or TEM). So far, no general theoretical picture for anomalous thermodiffusive convection has emerged. While some results [22,25] suggest that thermodiffusive pinches can be comparable in magnitude to the curvature driven pinch, others suggest that the curvature pinch can be significantly stronger than the thermodiffusive pinches [26]. It is believed that α is positive (inward convection) in a regime dominated by ITG modes and decreases when TEM become important. In plasmas with dominant TEM, α can become negative (outward convection) [74].

3.6   Conclusion

The transport in tokamaks can often be discussed in terms of three radial regions - the edge, where the atomic processes and edge localized modes are important, the centre, $q < 1$, where sawtooth macroinstabilities dominates and the high-gradient confinement region in between, in which drift-type microinstabilities are believed to be responsible for anomalous particle transport.

A variety of the mechanisms responsible for anomalous pinch in the confinement zone have so far been proposed. Neoclassical theory predicts a pinch proportional to the loop voltage (Ware pinch). Turbulent transport models predict a pinch proportional to the temperature gradient (thermodiffusion) and a pinch proportional to the gradient of the safety factor (TEP or curvature pinch). It was also shown [19,21,23] that the contribution of these pinches are additive and therefore the particle flux can be written as

$$\Gamma = -D\nabla n_e + D\left\{\frac{V_{Ware}}{D} - c_q\frac{\nabla q}{q} + \alpha_e\frac{\nabla T_e}{T_e} + \alpha_i\frac{\nabla T_i}{T_i}\right\} \qquad (3.15)$$

The coefficient c_q is positive, whilst α_e and α_i may be either positive or negative depending on the conditions (ITG or TEM) [23, 26]. Fluid turbulence codes do not in general provide convenient expressions for these coefficients for immediate comparison with experimental data. An assessment of the contributions of the different terms can, however, be obtained from experiment or from many simulations by varying the input profiles in the fluid model calculation [26].

Chapter 4

Particle sources

4.1 Introduction

For a deuterium (or hydrogen) plasma in steady state, the electron n_e and neutral n_0 densities within the closed flux surfaces can be described by fluid transport equations

$$\nabla(-D\nabla n_e + V \cdot n_e) = n_e n_0 S_{ion} - n_e^2 S_{rec} \tag{4.1}$$

$$\nabla(n_0 v_0) = -n_e n_0 S_{ion} + n_e^2 S_{rec}. \tag{4.2}$$

where V is the radial flow velocity (pinch velocity), v_0 is the neutral fluid velocity, S_{ion} is a rate coefficient for ionization of neutrals by electron impact, S_{rec} is the rate coefficient for radiative recombination and D is the particle diffusivity within the closed flux surfaces. These equations show that the presence of the particle source term directly influences the density gradient in regions where the source is important. Ionization of neutral particles causes peaking of the density and as it is seen from the equations above, the term $n_e n_0 S_{ion}$ has a similar influence on the density profile as an inward pinch velocity. Therefore the neutral particle source has to be considered as a possible candidate for peaked density profiles.
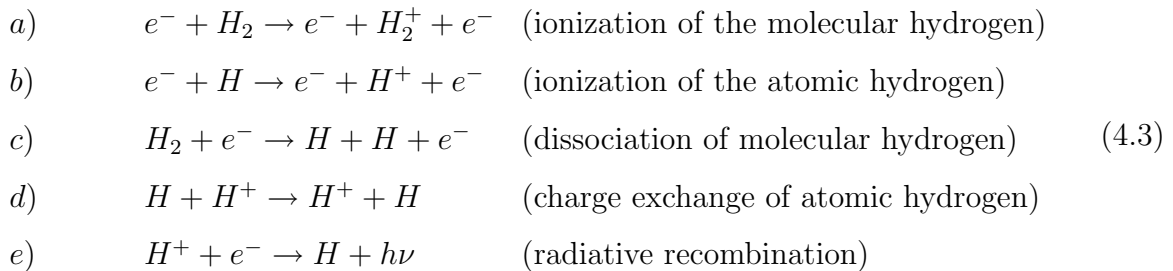
The potential sources of neutral particles in tokamak plasmas are neutrals coming from recycling, neutrals produced by recombination and neutrals injected by neutral heating beams. In the absence of neutral beams, the majority of the neutral influx comes from recycled deuterium released from the wall protection tiles (carbon in TCV and JET), which cover the inside of the tokamak vessel and are thus located at the edge. These

neutrals are initially cold and can be accelerated via charge exchange processes with hot plasma ions and produce fast neutrals with high v_0, which penetrate from the edge to the bulk plasma.

Neutral beam injection used for plasma heating represents an addition to the edge recycling source of neutral particles. The beam neutrals are characterized by high energy ($\sim 10^5\ eV$ in JET) and therefore can penetrate in to the plasma core. The location of the particle source produced by the beam and its strength depend on the beam deposition profile and have to be calculated for each discharge using numerical codes.

4.2   Penetration of neutrals

There are several reactions which are important in creation of ionized particle sources or sinks in hydrogen plasmas [77]:

$$
\begin{aligned}
&a) && e^- + H_2 \rightarrow e^- + H_2^+ + e^- && \text{(ionization of the molecular hydrogen)} \\
&b) && e^- + H \rightarrow e^- + H^+ + e^- && \text{(ionization of the atomic hydrogen)} \\
&c) && H_2 + e^- \rightarrow H + H + e^- && \text{(dissociation of molecular hydrogen)} && (4.3) \\
&d) && H + H^+ \rightarrow H^+ + H && \text{(charge exchange of atomic hydrogen)} \\
&e) && H^+ + e^- \rightarrow H + h\nu && \text{(radiative recombination)}
\end{aligned}
$$

The two major processes which lead to ionization of neutral hydrogen coming from the periphery are direct ionization of the molecular hydrogen (a) and ionization of the atomic hydrogen (b). Important processes which do not lead directly to creation of additional charged particles but determines the concentration of neutrals are dissociation of molecular hydrogen and the creation of Frank-Condon atoms (c) and charge exchange of atomic deuterium (d). A sink for hydrogen ions in the plasma is provided by radiative recombination (e). Reaction rate coefficients as a function of temperature for the reactions listed in Eq. 4.3 are shown on Fig. 4.1 [78]. It is seen from the comparison of Fig. 4.1A and B that radiative recombination of hydrogen atoms can play a role only in high density plasmas, since the rate coefficient of this process is significantly lower than the ionization and charge exchange rate coefficients. In the energy range above 100 eV, the recombination rate coefficient is smaller by 6 orders of magnitude than the rate coefficient
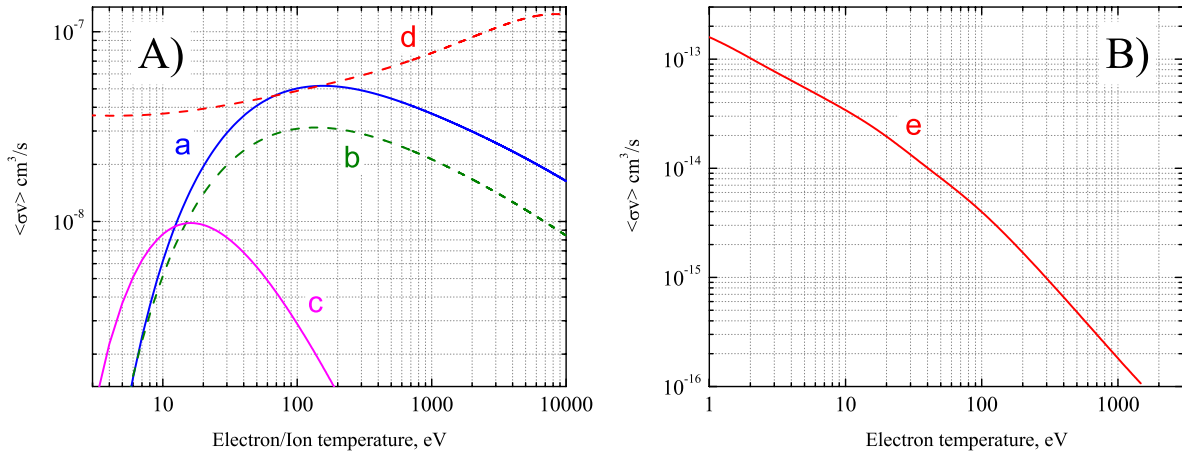
Figure 4.1: *A) and B) Rate coefficients for atomic processes in hydrogen [78]. The labelling corresponds to the reactions listed in Eq. 4.3*

for charge exchange or ionization. Consequently, in the regimes with low electron densities the main source of the neutral particles is the flux from the wall. The neutral concentration in the plasma is therefore determined by a balance between neutrals entering the plasma from the wall and the ionization. This balance depends on the velocity of neutrals, their concentration and on the density of the electrons.

For a particle with velocity v, the mean free path can be estimated as

$$\lambda = \frac{v}{n < \sigma v >},$$

where σv is the rate coefficient for the processes considered and n is the plasma electron or ion density. For the electron temperature range $20 < Te < 400\ eV$, typical for conditions just inside the LCFS, the rate coefficient for processes leading to the direct ionization of molecular hydrogen are larger than $2 \cdot 10^{-8}\ m^3$. For densities near the LCFS, which are usually in the range $0.5 - 5 \cdot 10^{19}\ m^{-3}$ and typical thermal velocities of $2 \cdot 10^3\ m/s$, the penetration length of molecular hydrogen λ is 1 cm or less. This penetration depth is rather small compared to the minor radius of TCV ($25\ cm$) or JET ($1\ m$) and therefore the contribution of the molecules to density peaking is small beyond the vicinity of the LCFS.

For Frank-Condon atoms, which result from molecular dissociation, with an average energy of $2\ eV$ the mean free path is still only of the order of $1\ cm$ at the high end of the density range, (at which molecular deuterium is not expected to penetrate beyond the
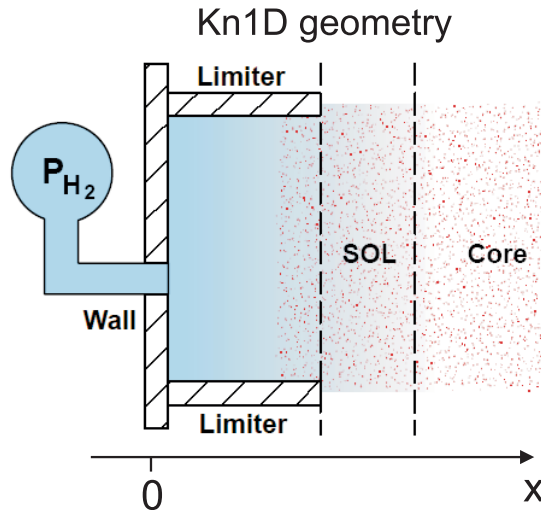
Figure 4.2: *Kn1D geometry*

LCFS), but may be as high as 10 *cm* at the lowest edge densities, which include many
of the TCV ECH plasmas. Moreover, unlike molecules neutral atoms can penetrate in
a diffusive-like manner by a sequence of charge exchange processes until an ionization
occurs. Charge exchange of slow neutral particles with fast plasma ions creates slow ions
and fast neutral particles. Energetic neutrals can have penetration lengths comparable
to the size of the plasma and therefore can be ionized or undergo subsequent charge
exchange reactions further inside the LCFS. The CX process is indeed important because
the resonant charge exchange cross section is higher than the ionization cross section.
Several CX reactions can occur before ionization, leading to an acceleration of the neutral
particles and therefore its flux.

The importance of CX neutrals depends on the ratio of neutral atomic fluxes to the
molecular fluxes as well as on the plasma background conditions and normally requires
specific codes to estimate. Additional complexity for the calculation of the neutral flux
comes from the fact that neutral atoms are not constrained by magnetic fields, therefore
numerical codes have to follow the particles in 2D or even 3D. Common methods used to
compute neutral particle penetration and sources in plasmas resulting from edge fuelling
are based on Monte-Carlo simulations implemented for example in code EIRENE [79]. The
complex 2D geometry of the wall source, the limiters and the scrape-of layer can be treated
by EIRENE, but large computational times limit the possible applications especially when

calculations of neutral concentrations deeply inside LCFS are needed. For the purpose of numerical treatment of neutral flux the bulk plasma simplified kinetic or fluid 1D codes are often used and since inside LCFS only a few important atomic processes are involved, one dimensional codes give reasonable agreement with sophisticated 2D modelling in many cases.

To estimate the importance of the neutral particle source term in the particle balance equation, we used the one dimensional kinetic transport code Kn1D [80]. Kn1D computes the neutral atomic and molecular hydrogen (or deuterium) distribution functions (f_H, f_{H_2}) in a slab-like spatial geometry with specified plasma profiles. The model geometry in Kn1D consists (in increasing values of x) of a wall surface, a local limiter shadow, a plasma scrape-off layer (SOL) region and a core plasma (Fig.4.2). The numerical algorithm includes charge exchange collisions, electron-impact ionization and dissociation, elastic self-collisions (atomic and molecular), and a variety of elastic cross-collisions (atom-ion, atom-molecule, molecule-ion).

4.3 Particle sources in TCV

TCV does not have a neutral beam heating system and therefore there are only two sources of neutrals in limited discharge: the flux of neutral atoms from the walls and the radiative recombination of the plasma bulk ions. The DNBI has an insignificant total source rate $\sim 10^{19}$ s^{-1} and was not yet available for most of the experiments described in this work.

4.3.1 Kn1D simulations for TCV

In defining the Kn1D geometry for TCV discharges the following assumptions were made. A limiter configuration with an inner wall as a limiter surface was chosen (see Fig. 4.3). In this case the neutral hydrogen recycling form a wall tends to be ionized inside the LCFS. Accordingly the SOL length was chosen to be equal to zero. The outer wall was assumed to serve as a wall in the Kn1D geometry and the length of limiter shadow was taken equal to 2 cm.

The background plasma electron density $n_e(\rho)$ and electron temperature $T_e(\rho)$ profiles
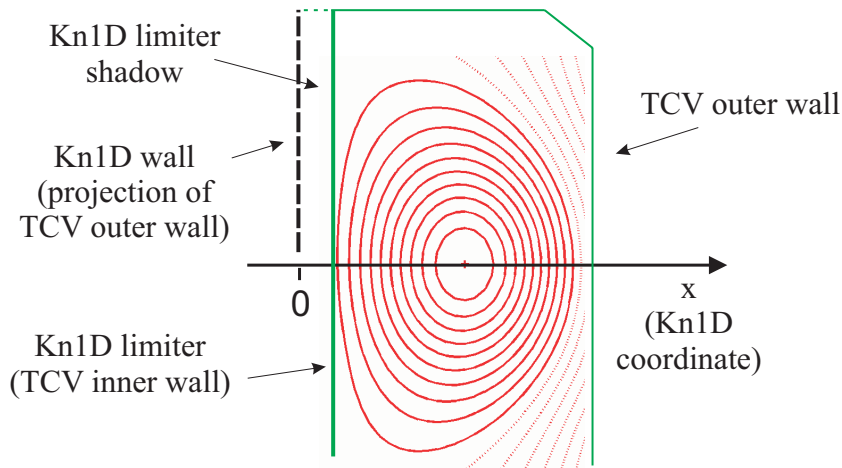
Figure 4.3: *Magnetic flux surfaces, contour of vessel (continuous line) and the elements of Kn1D geometry for a limited TCV discharge.*

inside the LCFS were taken from Thomson scattering measurements. Outside the LCFS, the temperature and density profiles were assumed to have an exponential decay leading to wall temperatures of the order of $10 - 20$ eV and densities $2 - 3$ times below the values at LCFS in accordance with Langmuir probe data [81]. Ion temperature profiles in the plasma bulk were approximated using data from charge exchange spectroscopy [82]. Outside the LCFS, an exponential decay of ion temperatures similar to that of the electron temperature decay was assumed. All profiles were remapped to the 1D coordinate along the axis x on Fig. 4.3 using the discharge equilibrium data.

The result of a Kn1D simulation as a function of distance along the x axis (Fig. 4.3) for a TCV Ohmic L-mode discharge is shown on Fig. 4.4. This discharge has a very low central electron density $n_e(0) \sim 8 \cdot 10^{18}$ m^{-3} and represent practically the lowest density of the TCV operational domain. The densities of molecular deuterium and of neutral atoms, the temperature of neutral atoms and the atomic ionization rate are shown on Fig. 4.4 by dashed lines. The atomic ionization rate plotted on Fig. 4.4d corresponds to the term $n_e n_0 S_{ion}$ in Eq. 4.1. Profiles of electron and ion temperatures are shown in Fig. 4.4 by solid lines. It is seen that the heating of the electrons by the Ohmic current and strong decrease of energy exchange between ions and electrons at low density results in a large difference, more than a factor of four, between ion and electron temperatures.

As it was predicted by a simple estimation at the beginning of this chapter, the density
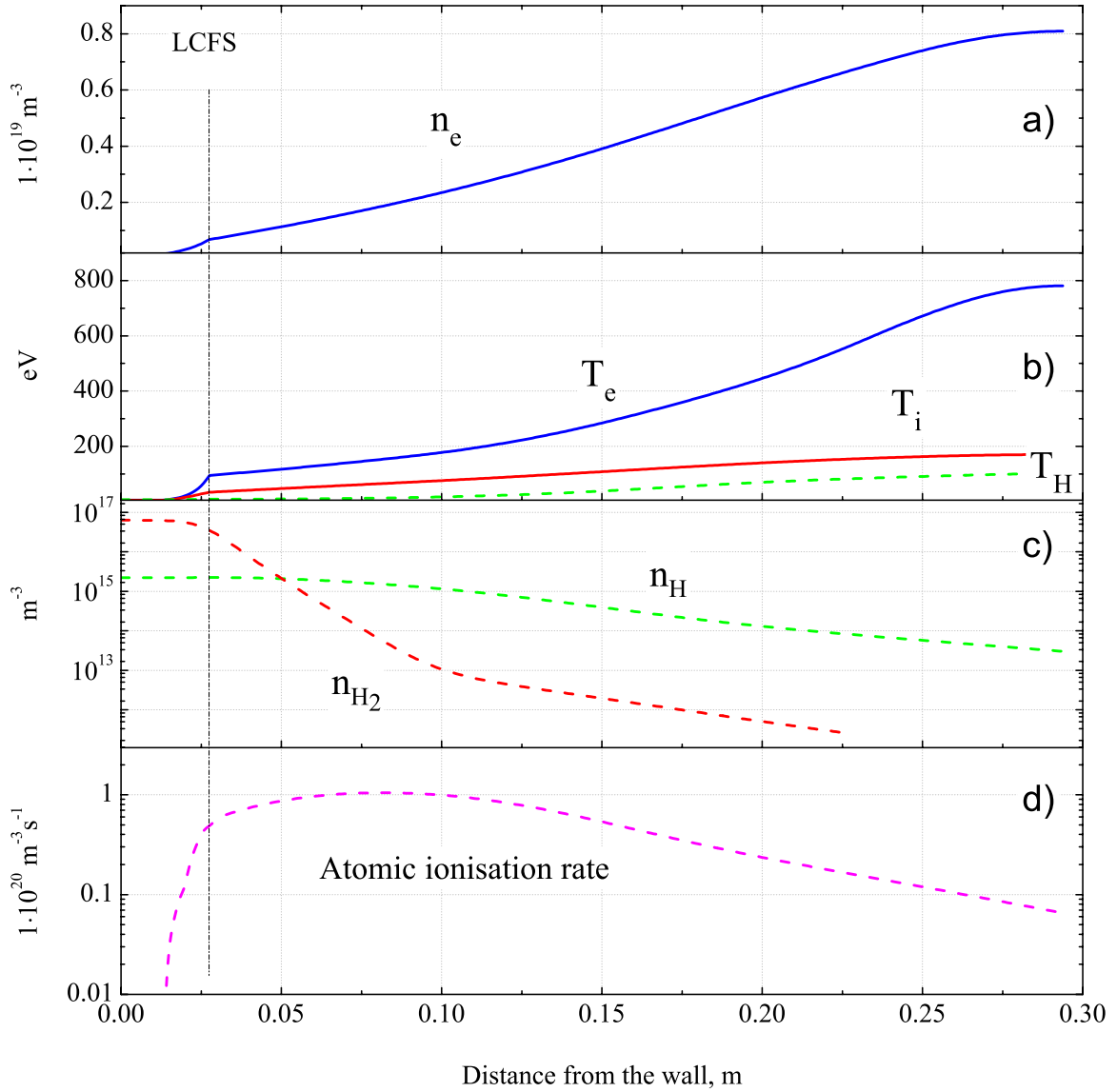
Figure 4.4: *Experimental profiles of electron density* **a)** *and electron and ion temperatures* **b)** *for the low density Ohmic discharge #25667 as functions of distance from the wall. The results of a Kn1D simulation for temperature of atomic deuterium* **b)**, *densities of molecular and atomic deuterium* **c)** *and atomic ionization rate* **d)** *are plotted by dashed lines. The dash-dotted vertical line indicates the position of the LCFS in 1D geometry.*

of molecular atoms drops down very rapidly with the distance from the limiter and the corresponding flux can be neglected over most of the cross section. The main part of the neutral flux inside LCFS is due to atomic neutrals and as seen from the changes of the simulated temperature of atoms, neutral particles penetrate in a diffusive-like manner increasing their energy in successive charge exchange processes. This increase of the energy

of neutrals leads to slower changes of the atomic ionization rate $n_e n_0 S_{ion} \simeq \nabla(n_0 v_0)$ with respect to the decrease of n_0.

The application of the results of calculations performed in the slab-geometry to real two dimensional geometry is not straightforward and can be performed only to some extend. In the case of TCV, we assumed that the results of the simulations using the geometry depicted in Fig. 4.3 provide the upper limit for the source term in the plasma bulk. The main argument is that in real 2D geometry the volume of central regions is much smaller than the volume of edge regions and the number of particles reaching the plasma core (from single localized limiter) will be smaller than the predicted flux for the central region in slab geometry.

To understand the importance of particle flux term in the particle balance equation simulated particle flux due to the edge source

$$\Gamma_{source} = \int (n_e n_0 S_{ion} - n_e^2 S_{rec}) dr \qquad (4.4)$$

was compared with an outward diffusive flux $\Gamma_D = -D\nabla n_e$, where ∇n_e is a gradient of experimental profile and D is diffusion coefficient. D was chosen to be a parabolic function $D = \rho^2 + 0.1 \ m^2/s$ with a non zero value at the centre. In steady state conditions and in absence of convection the total flux $\Gamma = \Gamma_D + \Gamma_{source}$ should be equal to zero.

To make a comparison we performed several simulations with different values of pressure at the wall P_{wall} which is a free parameter in Kn1D. In an ideal situation, this value should correspond to the vessel pressure. However in a real experiment, the complexity of walls and limiter geometry and uncertainties in molecular-atomic processes in SOL do not allow us to determine this absolute density of the neutral molecules at the wall with sufficient accuracy. Some constraints can come from a comparison of measured H_{alpha} emission with the Kn1D simulation but the poloidal asymmetry of the observed H_{alpha} emission make this comparison quite ambiguous.

In Fig. 4.5 a comparison of Γ_D obtained using experimental density profiles and Γ_{source} calculated by Kn1D is shown. The curve a) correspond to an exact match of Γ_{source} and Γ_D at the edge, which implies the absence of a radial pinch at $\rho = 1$ in steady state. Similarly two other curves correspond to situations when inward (curve b) or outward (curve c) pinches are present at LCFS.
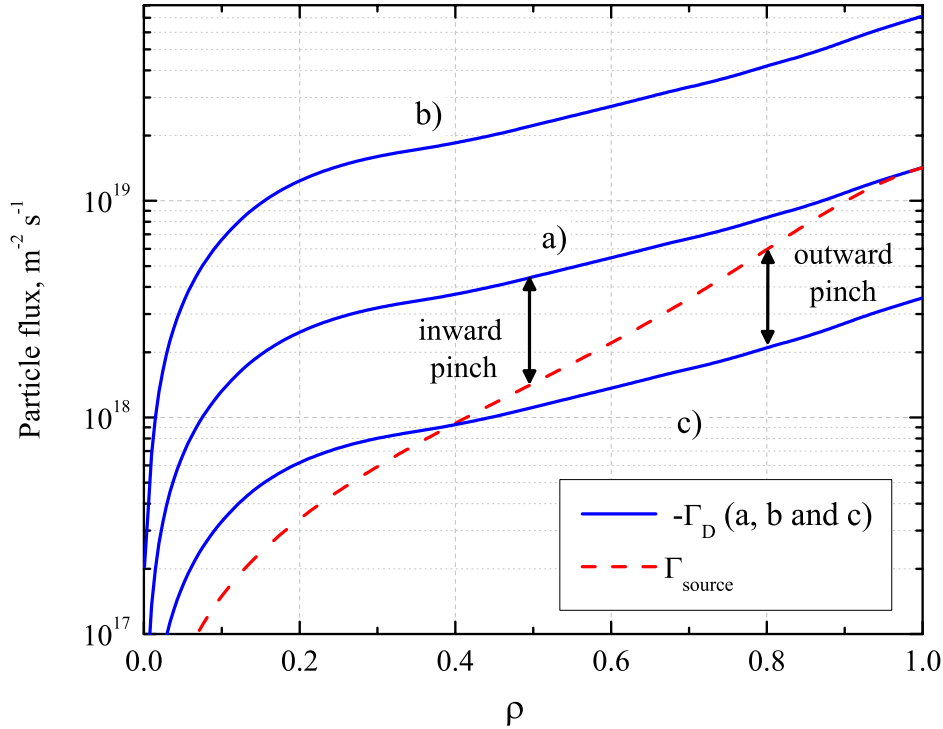
Figure 4.5: *Kn1D Simulation of particle flux Γ_{source} and electron diffusive flux from experimental electron density gradient assuming $D = \rho^2 + 0.1$ for the low density discharge in Fig.4.4. Lines a) b) and c) represent Γ_D for different values of $V(\rho = 1)$ assumed. In steady state, the difference between Γ_{source} and $-\Gamma_D$ require the presence of inward or outward pinch as shown by arrows.*

Due to the large difference in the slope of Γ_D and Γ_{source}, it is not possible to satisfy the particle balance equation without invoking convective processes. It is clearly seen that for the case of curve a) in Fig. 4.5, Γ_D and Γ_{source} match only at the edge. At $\rho \sim 0.6$ source flux due to ionization of neutral particles is smaller by a factor of 2.5 than the diffusive flux. In the plasma centre this difference is close to a factor 10. Therefore neutral particle penetration from the edge cannot be responsible for density profile steepness and an additional inward pinch term is needed to compensate the diffusive flux in steady state conditions.

It has to be noted that the absolute values of D chosen for the diffusive flux has no influence on the results of the comparison because of the above mentioned renormalization of Γ_{source}. However the profile of D is important. Measurements of D are difficult and were not available for this work. Taking into account the fact that measured by perturbative

technique, profiles of diffusion coefficient in L-mode tokamak discharges usually rises more slowly than ρ^2 [20,83–85] the choice of a parabolic function gives the lower limit on plasma particle flux profile and therefore increase the influence of edge particle source. If the profile of D is flatter than ρ^2 the difference between Γ_D and Γ_{source} would be even more important than in the example presented in Fig. 4.5. We should note, however, that with a steeper than ρ^2 profile of D, the Γ_D and Γ_{source} may be comparable over the entire discharge.

If an inward pinch is present at the LCFS (curve b) in Fig. 4.5), the difference between Γ_{source} and Γ_D becomes more significant than for the case of curve a) not only at the edge, but in the bulk as well. The example of curve c) shows that if an outward pinch is present at LCFS it must change direction at some point inside the plasma in order to keep the total flux zero at each radial position. The point of pinch reversal would depend on the values of the pinch at the edge, the diffusion coefficient, the plasma density and temperature profiles etc. We are not aware of any physical mechanism which can produce such a behaviour of the pinch velocity.

The previous example shows that at low densities the concentration of the neutral particles n_0 and as a consequence particle source $S_p \sim n_0 n_e < \sigma v >_{ion}$ in the plasma bulk is determined by CX process. The mean free path of the neutrals after charge exchange depends on the energy of the plasma ions, which in turn is determined by the plasma ion temperature. Additionally, a higher energy of neutral particles increases the associated flux (see Eq.4.2). Therefore it is important also to analyze discharges with high ion temperature.

Ohmic heating gives energy to the electrons and the ions are heated via electron-ion collisions. In the absence of transport an increase of ion temperature is determined by

$$\frac{dT_i}{dt} = \frac{T_e - T_i}{\tau_{ei}}$$

where τ_{ei} is the ions-electrons energy equipartition time

$$\tau_{ei} = \frac{3\sqrt{2}\pi^{3/2}\epsilon_0^2 m_i}{e^4 m_e^{1/2} \ln \Lambda} \cdot \frac{T_e^{3/2}}{n_i Z^2}$$

Here m_e and m_i are the electron and ion masses, Z is ion charge and Λ is Coulomb logarithm. The local power transmitted from electrons to ions can therefore be estimated
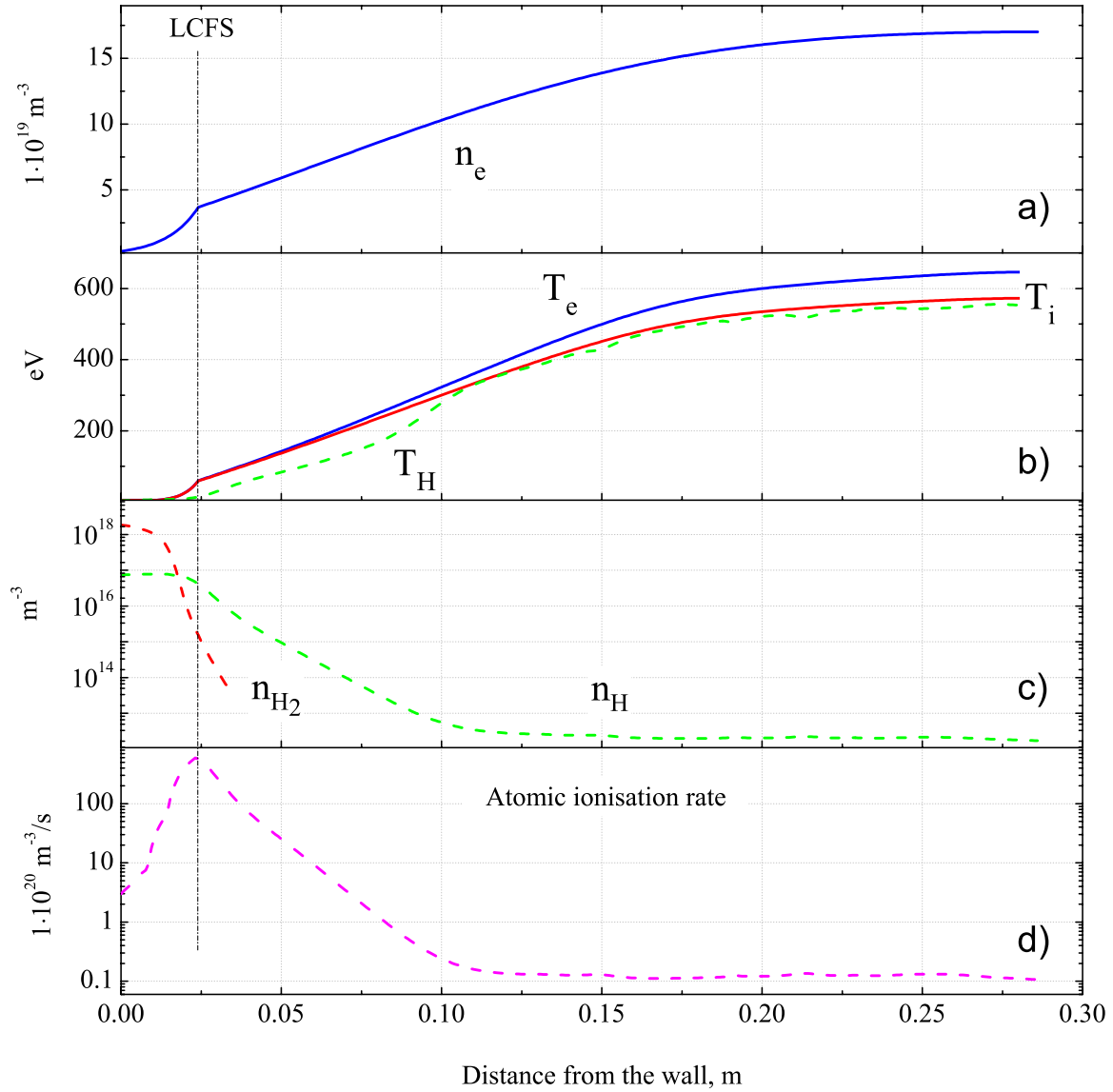
Figure 4.6: *Experimental profiles of electron density* **a)**, *electron and ion temperatures* **b)** *for the high density Ohmic discharge #25174 as functions of the distance from the wall. The results of Kn1D simulation for temperature of atomic deuterium* **b)**, *densities of molecular and atomic deuterium* **c)** *and atomic ionization rate* **d)** *are plotted by dashed lines. The dash-dotted vertical line indicates the position of LCFS in projected 1D geometry.*

as

$$P_{ei} = \frac{3}{2} n_i \frac{dT_i}{dt} \propto n_e^2 \cdot \frac{T_e - T_i}{T_e^{3/2}}$$

The transfer of energy to ions is more efficient for plasmas with high electron density and this fact is confirmed by ion temperature measurements in TCV.

To perform a simulation with Kn1D we chose a discharge close to the maximum density available on TCV: $n_e(0) \sim 1.7 \cdot 10^{20} \ m^{-3}$. The electron temperature was measured to be 650 eV at maximum and ion temperature was estimated from CSXR measurements [82] to be as high as 580 eV at the centre.
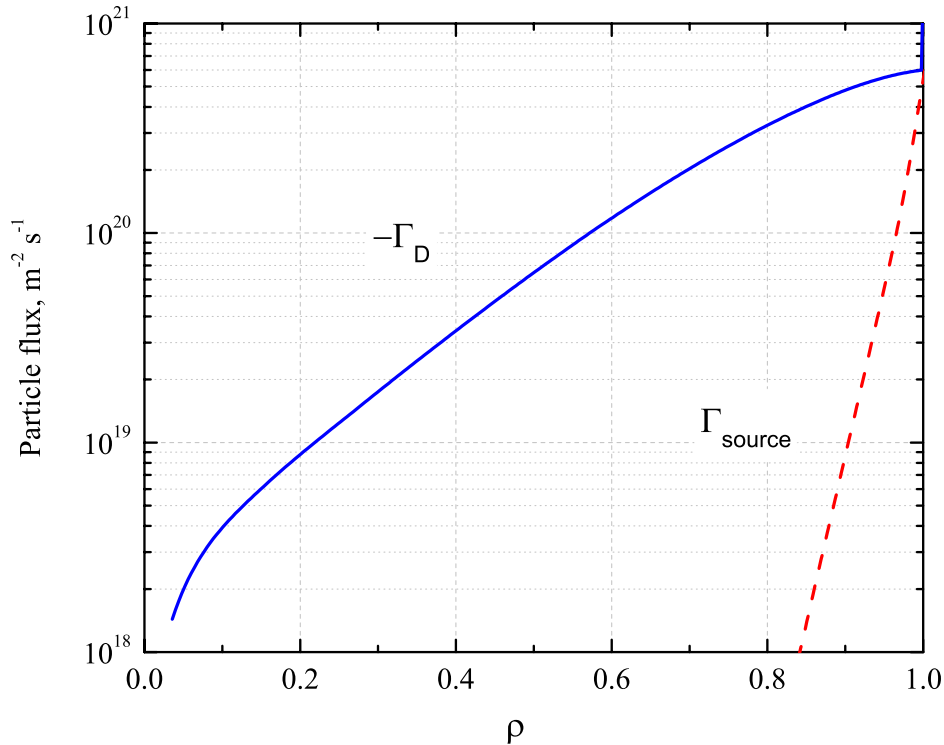

Figure 4.7: *Kn1D Simulation of particle flux Γ_{source} and electron diffusive flux from experimental electron density gradient assuming $D = \rho^2 + 0.1$ for the high density discharge in Fig. 4.6*

The results of the simulation are presented in Fig. 4.6 where all definitions are the same as for Fig. 4.4. The density of molecular deuterium drops by two orders of magnitude already in the limiter shadow and the associated flux can be completely neglected inside the LCFS. As in the case of the low density discharge, neutral atoms penetrate in a diffusive like manner increasing their temperature practically to 580 eV in the plasma centre. However the increase of the CX rate due to the high temperature cannot compensate for the strong decrease of the mean free path due to the density increase. The density of neutral atoms drops exponentially by four order of magnitude in first ten centimeters inside the LCFS and remains nearly constant from that point up to the centre. This con-

stancy of the neutral concentration is explained by recombination. The neutral particle concentration resulting from recombination is determined by the following expression

$$n_0 \simeq \frac{<\sigma v>_{rec}}{<\sigma v>_{ion}} \cdot n_i \qquad (4.5)$$

For electron temperatures of order of 500 eV the ratio $<\sigma v>_{rec} / <\sigma v>_{ion} \simeq 2 \cdot 10^{-8}$ and for ion densities $n_i \simeq 1 \cdot 10^{20}~m^{-3}$, the concentration of neutral atoms due to recombination, $n_0 \simeq 5 \cdot 10^{12}~m^{-3}$, is comparable with concentration of wall neutrals transported to the plasma bulk by CX process (see. Fig. 4.6C). From this point the concentration of the neutral particles in plasma does not depend anymore on the neutral flux from the wall since the later becomes several orders of magnitude weaker than the flux from recombination of plasma ions.

The results of a comparison of the outward diffusive flux with the particle flux created by neutral atoms is presented on Fig 4.7. The low electron density gradient in this particular discharge leads to the decrease of the plasma ion flux from the edge to the centre by more than two orders of magnitude. The particle flux created by neutrals still remains significantly low. In the central regions of the plasma, where recombination is important, the particle source flux becomes zero (Eq. 4.5 and Eq. 4.1). These results indicate that the particle source from the edge cannot account for density peaking in TCV high density discharge.

Other important domains of TCV operation are Ohmic H-mode discharges and discharges with ECH heating. Ohmic H-mode discharges on TCV have central densities higher than $6 \cdot 10^{19}~m^{-3}$ and the conclusions of the simulation presented on Fig. 4.6 and 4.7 are valid. ECRH discharges are characterized by high electron temperatures (several keV) and low central electron densities (typically $1 \div 3 \cdot 10^{19}~m^{-3}$). In these conditions the electron-ion coupling is strongly reduced and ion temperatures remain low ($T_i(0) \sim 200 - 400~keV$) [82]. Therefore, the neutral penetration is similar to the neutral penetration in the low density discharge presented in Fig. 4.4 and Fig. 4.5.

It has to be noted that due to the complexity of the problem, the inaccuracy of 1D simulations and followed-up mapping on 2D discharge geometry the results of the simulations presented in this section are quite approximative and need to be confirmed by experimental observations.

4.3.2   Experimental evidence of neutral penetration on TCV

As predicted by the simple formula for the mean free path of edge neutrals and observed in the more complex diffusive like behaviour, the penetration of the neutrals is dependent on the absolute value of electron density. Kn1D simulations performed for plasma parameters taken from shot #25174, show that at fixed profiles of electron temperature and for fixed plasma shape, ratio of $-\Gamma_D/\Gamma_{source}$ at $\rho_{pol} = 0.7$ is an exponential function of the central density in the range $n_e(0) = 0.8 \cdot 10^{18} - 6 \cdot 10^{19} \ m^{-3}$

$$\frac{-\Gamma_D(0.7)}{\Gamma_{source}(0.7)} \approx e^{0.8 \cdot n_e(0)/10^{19}}$$

For central densities higher than $6 \cdot 10^{19} \ m^{-3}$ the recombination starts to play a role and the dependence on the $n_e(0)$ disappears. However, for such densities the ratio $-\Gamma_D/\Gamma_{source}$ at $\rho_{pol}(0.7)$ is already close to 100 and therefore Γ_{source} can be neglected. As a result, one experimental test for the importance of edge neutrals in the formation of electron density gradients is a comparison of profiles with different central densities.

Two examples of normalized profiles of electron density for Ohmic L-mode discharges with similar plasma current and shape are shown in Fig. 4.8A and B. All discharges have practically same peaking of electron density at fixed current, completely independent of the absolute values of the density. Even the low density discharge, which represents a typical target for ECRH scenarios, shows no additional peaking in comparison with the very high density discharge (Fig. 4.8). Therefore we can conclude that the experimental data show no evidence for the importance of edge neutral penetration, thereby confirming the conclusion drawn from Kn1D simulations.

Another way of experimentally assessing the effect of the edge source is a comparison of the electron density peaking in deuterium and helium plasmas. The ionization cross-section is higher in He than in H and the charge-exchange cross-section is much lower. This combination of these properties should lead to a significant reduction of the fast CX neutral flux and hence of deep fuelling.

Helium can exist as an neutral atom, as an ion with charge $+1$ or it can be completely ionized. Charge exchange is possible on both stages: He^+ and He^{++} and the respective atomic processes are called single and double charge exchange. The rate coefficients of the
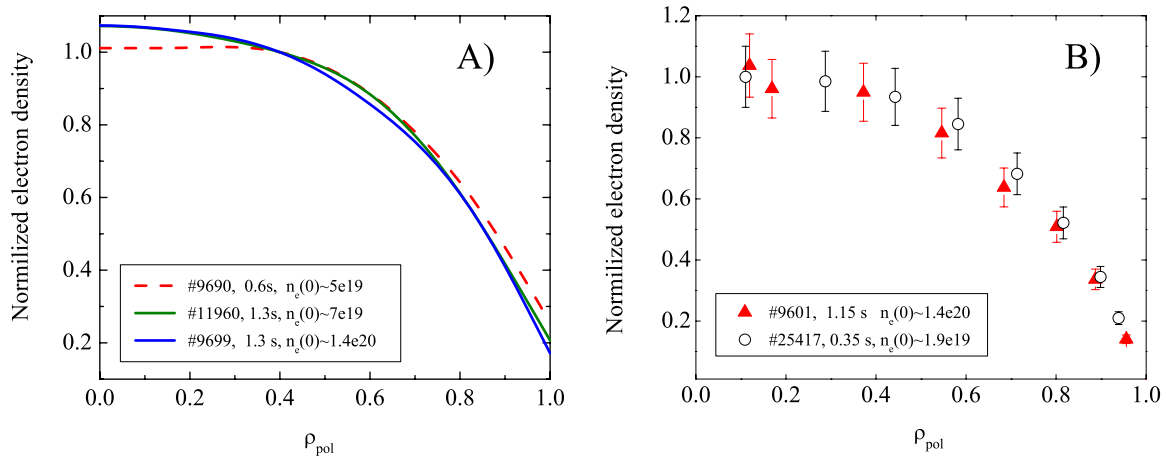
Figure 4.8: *A) Fitted TS electron density profiles in three Ohmic L mode discharges normalized to the values at inversion radius (plasma current 0.3 MA) B) TS measurements mapped to ρ_{pol} grid and normalized on central value for two discharges with plasma current 0.22 MA.*

processes in He are shown on Fig. 4.9. The double CX rate coefficient is more than four times lower in He than in H (see Fig. 4.1 for comparison). At the same time cross-section of ionization of the atoms is only 1.5 times smaller in He than in H. Therefore the ratio $< \sigma v >_{CX} / < \sigma v >_{ion}$ for He is equal to 1/5 at 100 eV that is 10 times lower than the same ratio in H. It means that CX chains are practically absent in the plasmas, and no significant deep fuelling is to be expected.

We did not have at our disposal a transport code for atoms and ions able to treat a pure He plasma and in order to understand the difference in neutral penetration between H and He discharges we performed the following reasoning. Neutral atoms with an initial density n_0 (left of the diagram 4.10), directed towards the plasma core from the edge can be ionized, experience charge exchange with fast plasma ions and create fast neutral atoms or penetrate as cold neutrals into the plasma. The branching ratios for the different processes are determined by the corresponding rate coefficients. Assuming a fixed electron density, ion and electron temperatures along the penetration path, we can estimate the decay of the initial concentration and the final concentration of fast neutral particles which contribute to the density peaking at plasma core. The reactions
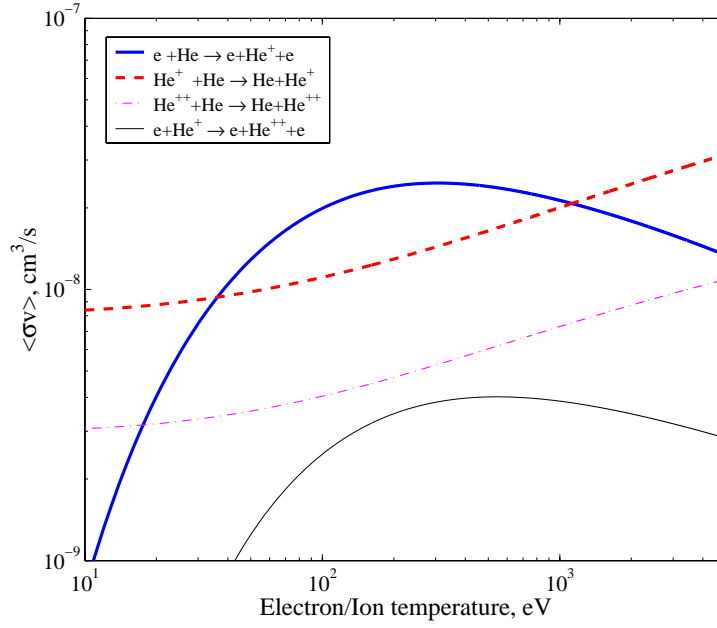
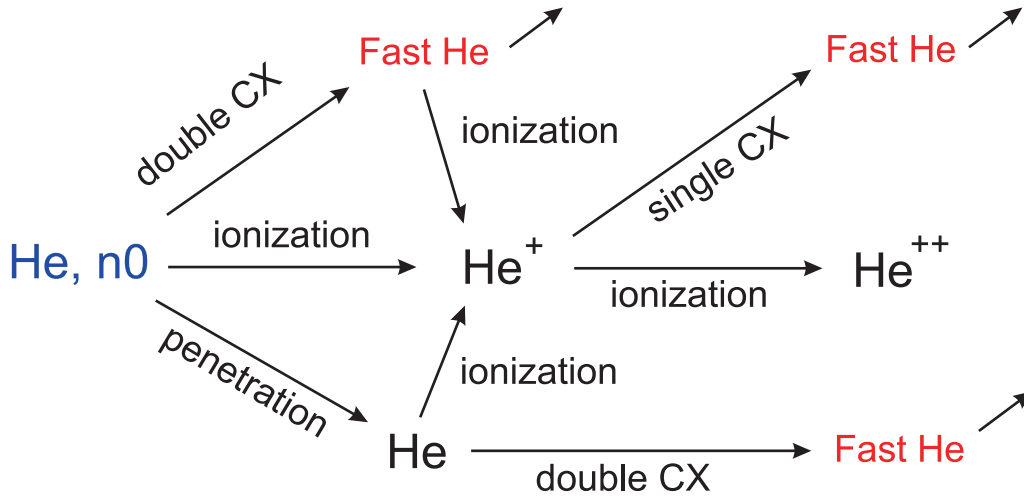Figure 4.9: *Reaction rate coefficients for important atomic processes in He plasmas*

Figure 4.10: *Schematic representation of He penetration*

corresponding to the left part of the diagram are the following:

| Double CX: | $He^{++} + He \rightarrow He + He^{++}$ | $\nu_{doubleCX} = n_e \cdot < \sigma v >_{doubleCX} /2$ |
| Ionization of He: | $e + He \rightarrow e + He^{+} + e$ | $\nu_{ion} = n_e \cdot < \sigma v >_{ion}$ |

where the last column represents the corresponding rates and $n_{He^{++}} = n_e/2$ was assumed. For ion and electron temperatures of about 200 eV typical for Ohmic L-mode TCV discharges in the region $\rho_{pol} \simeq 0.8 - 0.9$ the total ionization rate exceeds the rate of double charge exchange by factor of 5 and therefore the probability of ionization is four

times higher than creation of fast neutral via CX. Assuming an exponential decay of the densities with the distance and taking into account the relations

$$-dn_0(x) = dn_{H++}(x) + dn_{0fast}(x),$$

$$\frac{dn_{0fast}(x)}{dn_{H++}(x)} = \frac{\lambda_{ion}}{\lambda_{CX}}$$

we can estimate the densities of n_{He^+} ions and fast neutrals n_{01fast} at a distance $x_1 = \lambda_{CX}$:

$$n_{0fast} = \frac{n_0 \lambda_{CX}}{\lambda_{ion}\left(1 + \frac{\lambda_{CX}}{\lambda_{ion}}\right)} \left\{1 - \exp\left(-\frac{x}{\lambda_{CX}} - \frac{x}{\lambda_{ion}}\right)\right\} \sim 0.15 \cdot n_0 \qquad (4.6)$$

$$n_{He^+} = \frac{n_0}{\left(1 + \frac{\lambda_{CX}}{\lambda_{ion}}\right)} \left\{1 - \exp\left(-\frac{x}{\lambda_{CX}} - \frac{x}{\lambda_{ion}}\right)\right\} \sim 0.6 \cdot n_0 \qquad (4.7)$$

Since the density of He^{++} at $\rho_{pol} \simeq 0.8 - 0.9$ is significantly higher than the density of He^+ produced by the edge neutrals, the single CX process and the resulting density of fast neutrals (top right of the Fig. 4.10) can be completely neglected. At this stage, the fast neutral can be produced only by double CX on the cold neutrals having penetrated from the edge or fast neutrals created from the preceding double CX. The probability distribution between ionization products (ions) and double CX products (neutrals) can be again estimated using Eq. 4.6 and Eq. 4.7.

Summarizing above we can see that at temperatures about $200 \ eV$ and at the distance $2\lambda_{CX}$ less than 20% of initial neutral concentration n_0 will give rise to fast neutrals and more than 80% will be ionized. For comparison, in deuterium plasma at the same distance more than 80% of initial cold atoms will create fast ions in charge exchange reactions. Thus, the different atomic physics in He and H plasmas results in significant difference in formation of fast CX neutrals and should lead to the difference in profiles of electron density in identical discharges performed in He and H if neutrals originating from the edge contribute to the density peaking.

He plasmas with ratios of $He/(He + D)$ higher than 90 % at high electron density were obtained in TCV [86]. Ohmically heated, diverted configurations were performed with a steady state flat top of $1 \ s$. The electron density profiles, remapped on ρ_{pol} for two He discharges with different current and central densities, together with their
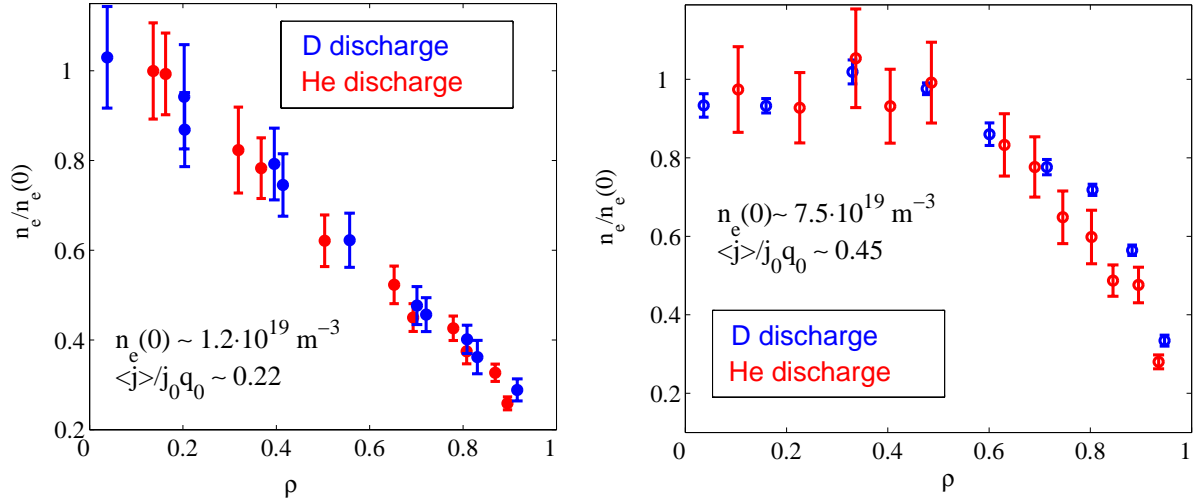
Figure 4.11: *Comparison of the density profiles (left - low density discharge, right - high density discharge) measured by TS in TCV Ohmic He and D plasmas.*

deuterium counterparts are shown on Fig. 4.11. Assuming that the source term in Eq. 4.1 is important and taking into account the analysis presented above one should expect flatter density profiles in He discharges than in D discharges. Evidently, both examples, representing high density and low density discharges, show no sign of flattening of profiles when He is the working gas, thus proving again the insignificance of edge neutrals for the formation peaked density profiles.

4.4 Particle sources in JET

The large size of JET ($a \simeq 0.85\ m$) would require a multi-step CX chain, which would results in neutral energies, after CX with hot plasma ions, as high as the ion temperature. Auxiliary heating on JET leads to ion temperatures comparable to the electron temperatures, attaining several keV at the plasma centre and high ion temperatures can be obtained even at low densities by neutral beam injection. Compared with TCV, the increase of the flux due to the energy increase might compensate the decrease of neutral densities due to the large machine size.

The next sections present the results of Kn1D simulations performed for JET, as well as experimental results indicating the unimportance of edge source in density peaking. The presence of an additional source of neutral particles due to the neutral heating beams

is also discussed.

4.4.1 Kn1D simulations for JET L-mode plasmas

JET has a complex scrape-off layer with multiple non toroidally symmetric limiters used during the OH phase. Moreover, most JET discharges have a diverted configurations. These conditions make one dimensional simulations of edge plasma very inaccurate. However, since the main interest of the study is the particle source term inside LCFS the following simplifications in the construction of the 1D geometry were made. The lengths of the SOL and the limiter shadow were chosen to be equal to 5 *cm* and the distance along the shortest chord from the limiter to the plasma centre was chosen as a grid for Kn1D. In fact, the details of the geometry outside the LCFS influence the shape of calculated particle source only a few cm inside the LCFS and for large machines such as JET, the inaccuracy in the definition of the geometry does not affect the results in plasma bulk.

The electron temperature profiles are taken from LIDAR TS measurements and the ion temperature was taken from CXS measurements [54]. The density profile was obtained using the SVD-I method described in chapter 2. The density outside the LCFS was assumed to decrease exponentially with a distance according to [87]. All profiles were remapped to a one dimensional coordinate along the chord passing from edge to the plasma centre in the midplane using the equilibrium code EFIT [56].

Fig. 4.12 shows experimental density and temperature profiles and simulation results for an L-mode JET discharge in limiter phase heated only with the LH system (this discharge is characteristic of experiments presented in chapter 6). According to the LIDAR measurements the central density is $n_e(0) \sim 1.3 \cdot 10^{19}~m^{-3}$ and the central electron temperature is 3 keV. The ion temperature inferred from the CXS measurements is lower than the electron temperature. Vertical lines on the Fig. 4.12 mark the LCFS and limiter position in the chosen 1D geometry for Kn1D.

The simulation shows that the large scale of JET with respect to TCV results in complete ionization of molecular hydrogen already in the SOL region. The rate of decrease of the neutral density with distance is similar to the rate obtained for TCV. This results in smaller concentration of the neutral hydrogen at JET than on TCV at the same ρ.
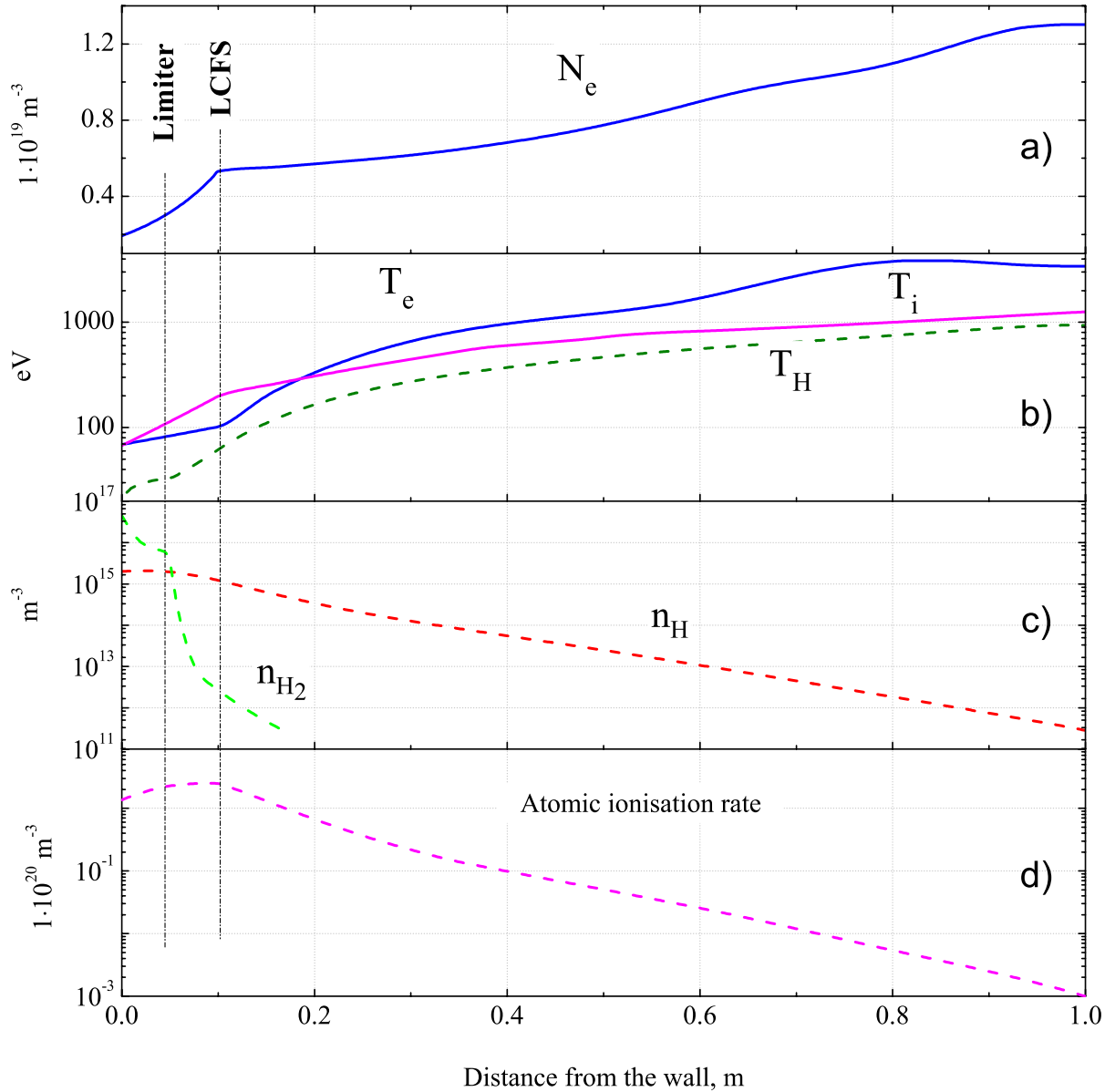
Figure 4.12: *Experimental profiles of electron density* **a)** *and electron and ion temperatures* **b)** *for the JET L-mode discharge #25667 as functions of distance from the wall. The results of a Kn1D simulation for temperature of atomic deuterium* **b)**, *densities of molecular and atomic deuterium* **c)** *and atomic ionization rate* **d)** *are plotted by dashed lines. The dash-dotted vertical line indicates the position of the limiter and LCFS in 1D geometry.*

Diffusive like penetration via charge exchange of neutral atoms on energetic plasma ions increases the neutral ion temperature up to 1 keV in the plasma centre.

A comparison of Γ_D and Γ_{source} similar to the one performed for TCV is shown in Fig.
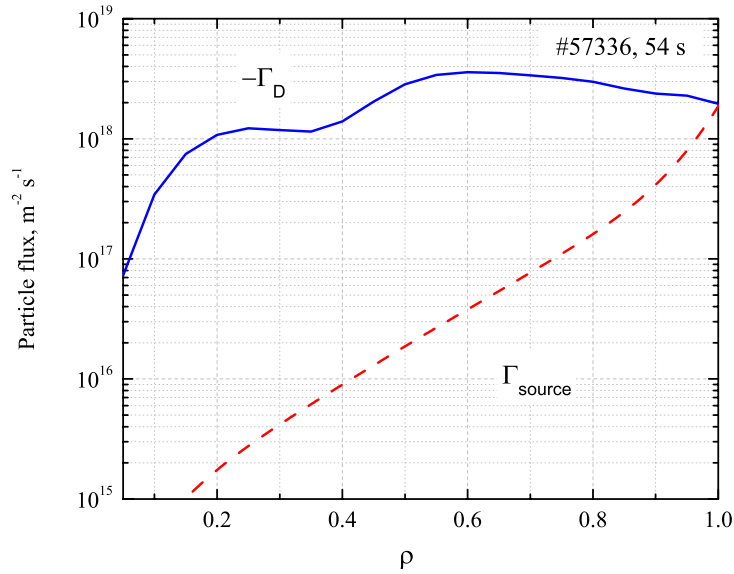
Figure 4.13: *Kn1D Simulation of JET particle flux* Γ_{source} *and electron diffusive flux from experimental electron density gradient assuming* $D = \rho^2 + 0.1$

4.13. The difference between the outward plasma particle flux and the flux created by neutrals coming from the edge is more than one order of magnitude, even in the vicinity of plasma edge and increases toward the centre despite the strong decrease of the diffusive flux. This confirms the unimportance of Γ_{source} in particle balance equation for this type of the discharges.

The results of simulations for high electron and ion temperature JET discharge have to be taken with caution because of limitation of Kn1D atomic cross section data to 800 eV beyond which reaction rates are taken as constants. Nevertheless, this restriction does not alter the results since changes in the cross sections for ionization and charge exchange could not account for orders of magnitude difference between Γ_D and Γ_{source} in L-mode discharge. This limitation, however, will strongly influence the results of the simulations in H-mode discharges because of the pedestal region characteristic for H-mode. In the narrow edge localized pedestal electron and ion temperatures rise from hundreds of eV to a few keV, well above the 800 eV Kn1D limit and hence simulations are not reliable already in the edge region. In order to understand the importance of the source term in H-mode plasmas we relied on the experimental evidence presented in the next section.

4.4.2   Experimental evidence of neutral penetration on JET

In Fig.4.14A two electron density profiles measured by LIDAR TS in the H-mode phase of two discharges are shown. The high density discharge # 52823 has a plasma current $I_p = 2.5 \ MA$, edge safety factor $q_{95} = 4$ and main magnetic field $B_t = 2.7 \ T$. Only NBI heating with a power of 15.8 MW was used. The low density discharge #59301 was heated using 6 MW of ICRH power in addition to 8.9 MW of NBI power. The plasma parameters are the following: $I_p = 1.5 \ MA$, $q_{95} = 4$, $B_t = 1.7 \ T$. In both discharges the profiles of electron temperature measured by LIDAR TS are practically identical as shown in Fig. 4.14B. Profiles of ion temperatures (not shown) measured by CXRS are very similar to the electron temperature profiles. Because of the differences in Z_{eff} the two discharges had the same effective collisionality. The difference in the absolute values of the density leads to a strong difference in the particle source from the edge or from heating beams. The profile of the particle source from heating beams was calculated by the PION beam stopping code and plotted by a solid line on Fig. 4.14D. The high density discharge has significantly lower values of atomic ionization rate in the core than the low density discharge and the profile is also different. At the same time the normalized profiles of the electron density (Fig.4.14C) for both discharges are practically identical. The similarity of the electron density profiles is also confirmed by SVD-I method. The identical peaking for the same T_e and T_i, while the density differs by a factor of nearly 3 unambiguously establishes the unimportance of the particle source both from the edge neutrals and from heating beams. A systematic study, presented in chapter 6, shows that in H mode, the collisionality, not density or neutral mean free path is the main scaling parameter for density peaking.

Comparison of He and D plasmas

As in the case of TCV, a pure He plasma in JET is expected to modify the properties of neutral penetration and would give an indication of the importance of multistep CX fuelling processes. We compare electron density profiles from similar JET discharges which were measured in deuterium and helium plasmas. Helium discharges with a purity of nearly 90% were created in the plasma current range $1 - 2.5 \ MA$ with neutral heating
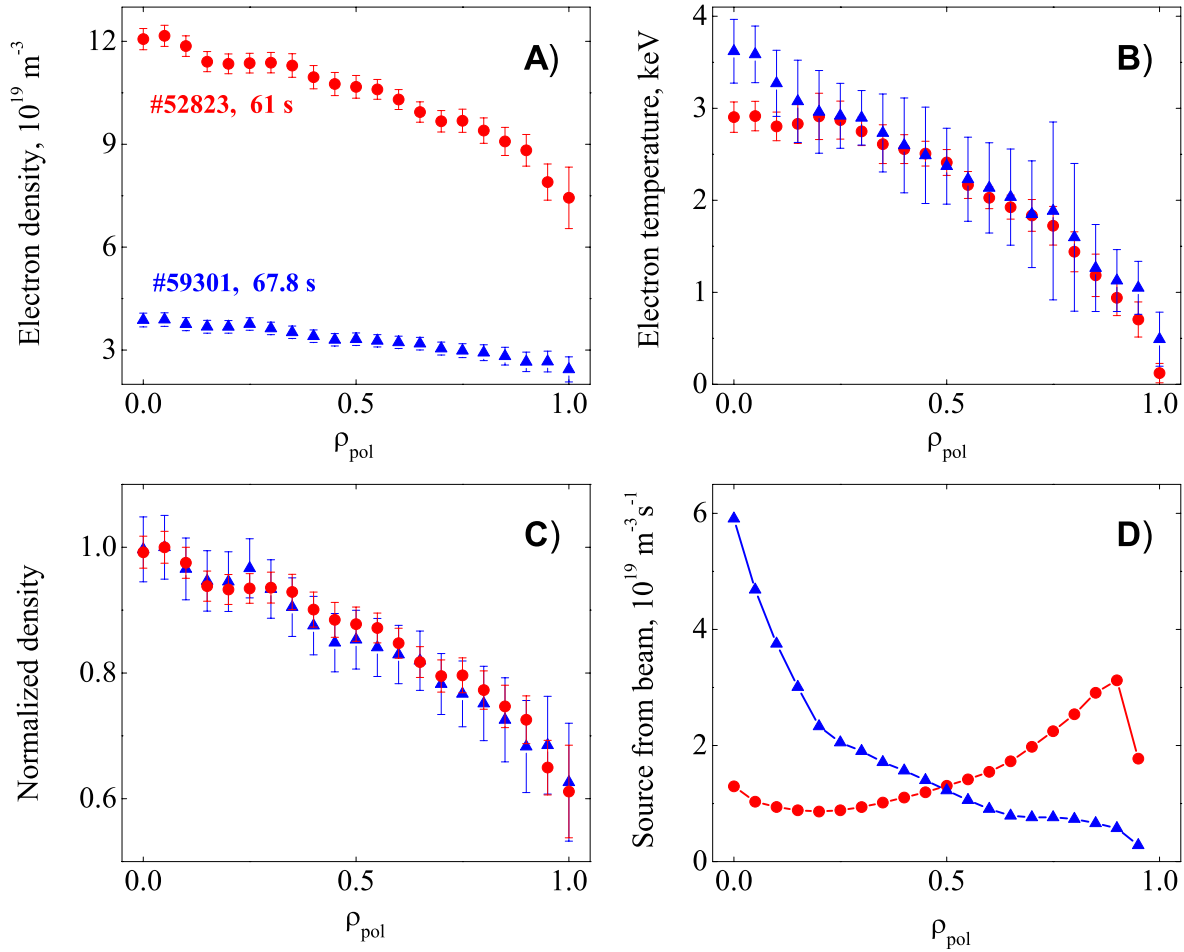
Figure 4.14: *Comparison of two H-mode discharges with different values of central densities.* **A)** *and* **B)** *Electron density and electron temperature profiles from Lidar TS measurements.* **C)**. *Electron density profiles normalized on central density values.* **D)** *Profiles of particle sources from neutral heating beams.*

beam powers up to 12 MW [88]. He discharges were chosen to match as closely as possible previous, well characterized D discharges. This allowed to select about 50 pairs of density profiles with very similar discharge conditions and as only difference the working gas. ELMing H - and L - mode phases are equally presented in the selection. Examples of electron density profiles in He and D in L-mode high current discharge and in low current H-mode discharges are presented in Fig. 4.15 and Fig. 4.16 respectively. Details of the profiles in He and D, obtained with the SVD-I method, are in very good agreement with a slight indication of additional peaking in He. Density profile peaking factor defined as $n_e(0)/ < n_e > s$, where $<>$ is the volume average and $n_e(0)$ is central density, in He
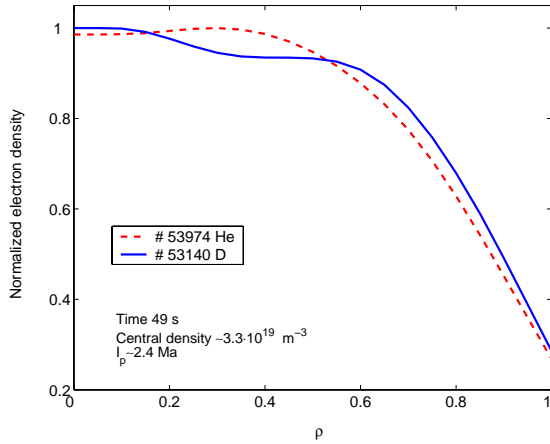
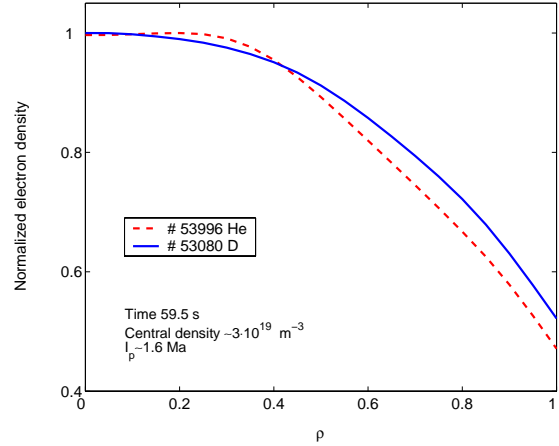Figure 4.15: *Comparison of electron density profiles in He and D of L-mode high current discharge*

Figure 4.16: *Comparison of electron density profiles in He and D of H-mode low current discharge*
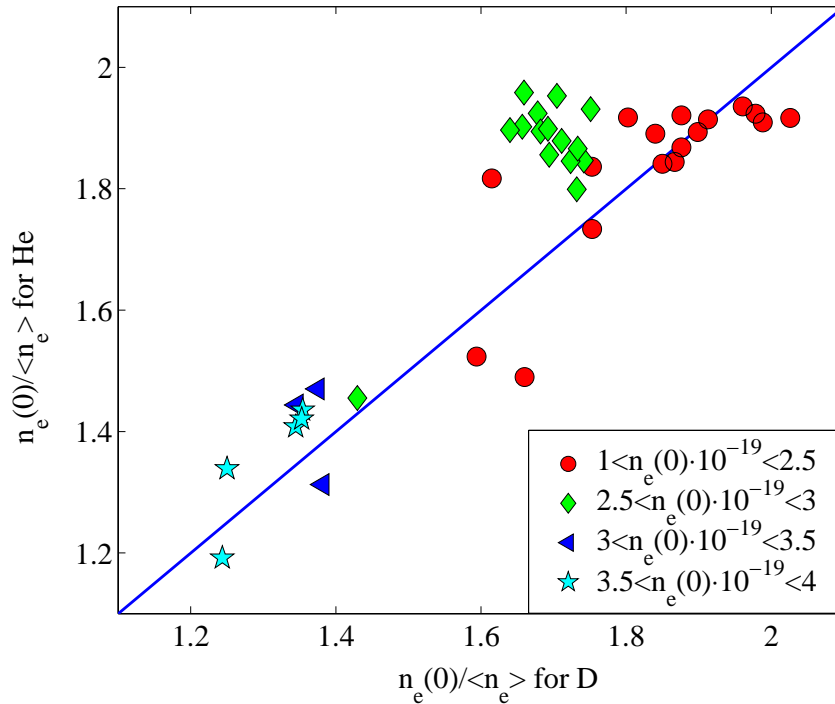

Figure 4.17: *Electron density profile peaking in He discharges compared with peaking in identical D discharge. The line indicates identical profile peaking. The symbols refer to the classes of central density.*

discharges as a function of peaking factor in D discharges is presented in Fig. 4.17. The diagonal line corresponds to an exact matching of the profile peaking. The central density in the selection is distinguished by classes of symbols and varies by a factor of two from

$n_e(0) \sim 2 \cdot 10^{19} \ m^{-3}$ to $n_e(0) \sim 4 \cdot 10^{19} \ m^{-3}$. It is clearly seen that density peaking in some of He discharges is slightly higher than in D discharges as it was noticed in individual profile comparisons. The comparisons of individual profiles and the independence of peaking on the working gas show the penetration of CX edge neutrals cannot account for density peaking.

4.5 Summary

The analysis presented above and more so the experimental evidence, show that for TCV and for JET, the region over which the source term due to edge neutrals is important is restricted at all densities and examined discharge conditions, to the outermost few cm of the discharge and can be ignored in the particle balance equation for the core plasma. These results indicate that a recently voiced claim that density peaking in JET H-modes may be due to edge fulling [89], appears to be misguided.

Chapter 5

Electron density profile behaviour in TCV

5.1   Introduction

This chapter is devoted to an overview of experimental observations of the electron density profiles in TCV plasmas in a very wide range of discharge conditions. In order to understand the density behaviour, we created a database of about 1000 samples taken in the steady state phase of more than 600 discharges. The investigation presented here includes Ohmically heated L-mode plasmas, plasmas with electron cyclotron resonance heating (ECRH) and plasmas with a substantial fraction of electron cyclotron current drive (ECCD). Special cases, such as discharges with density pumpout and discharges with electron internal transport barriers are also discussed.

The electron density and the electron temperature profiles were obtained from a repetitively pulsed Thomson scattering system [30]. The measurements were mapped and fitted as smooth functions of the flux surfaces given by the LIUQE equilibrium code [90].

Conventionally the profiles are characterized by a profile peaking factor which is defined as $n_e(0)/ < n_e >$ where "$<>$" means volume average and $n_e(0)$ stands for central density. A flat profile has $n_e(0)/ < n_e > = 1$ with the peaking factor increasing as the density profile becomes steeper. The common definition of the profile peaking includes a normalization on the value of central density which is not very convenient for analyzing sawtoothing discharges. The sawtooth instabilities result in a periodical flattening of the profile inside the sawtooth inversion radius and lead to a scatter of the core Thomson
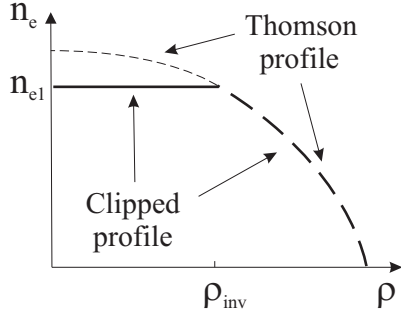
Figure 5.1: *"Clipped" density profile (bold line) together with measured density profile. The two profiles are coincident for $\rho > \rho_{inv}$, where ρ_{inv} is inversion radius determined from the TCV soft-x ray tomography system.*

measurements taken at random times in the sawtooth cycle. In order to reduce these uncertainties in the analyzed profiles, we introduced a "clipped" density profile peaking factor, shown on the Fig. 5.1 and defined as follows $n_{e1}/ < n_e >$ (standard peaking will be refereed as $n_{e0}/ < n_e >$ or $n_e(0)/ < n_e >$). In the "clipped" peaking factor definition n_{e1} is the electron density at the sawtooth inversion radius, $n_e = n_{e1}$ for $\rho < \rho_{inv}$ and $n_e = n_e$ for $\rho \sim \rho_{inv}$. We may consider those as representative of the profile just after the sawtooth crash when the central part of the profile is flatted. Therefore by using "clipped" profile peaking factors we were only concerned with the profiles in the confinement zone, where they can be considered as being in a steady state, since density profiles in the range $\rho_{inv} < \rho < 1$ have no significant changes during the sawtooth cycle.

5.2   Ohmic L-mode discharges

5.2.1   Stationary conditions

A database of Ohmic L-mode discharges consists of about 300 profiles taken in steady state phase from a wide variety of positive shear ($\partial q/\partial \rho > 0$), limited configuration discharges in TCV: $0.7 \cdot 10^{19} \leq n_e(0) \leq 16 \cdot 10^{19} \ m^{-3}$, $2.3 \leq q_{95} \leq 13$, $1 \leq \kappa_a \leq 2.6$, $-0.5 \leq \delta_a \leq 0.7$, $0.1 \leq \nu^*_{75} \leq 16$, $0.5 \leq \nu_{eff75} \leq 25$, where κ_a and δ_a are the elongation and the triangularity at the last closed flux surface, q_{95} is the safety factor evaluated at 95% of poloidal flux, $n_e(0)$ is the central electron density, ν^*_{75} is the electron collisionality parameter (Eq. 3.5) and ν_{eff75} (Eq. 3.10) is the effective collisionality for drift mode growth rate at 75% of the poloidal flux.

Fig. 5.2A shows a representative normalized experimental density profiles in Ohmic L-mode plasmas. The discharge # 9588 ($I_p = 450 \ kA$, $n_e(0) \simeq 8.5 \cdot 10^{19} \ m^{-3}$, $T_e \simeq 800 \ eV$)
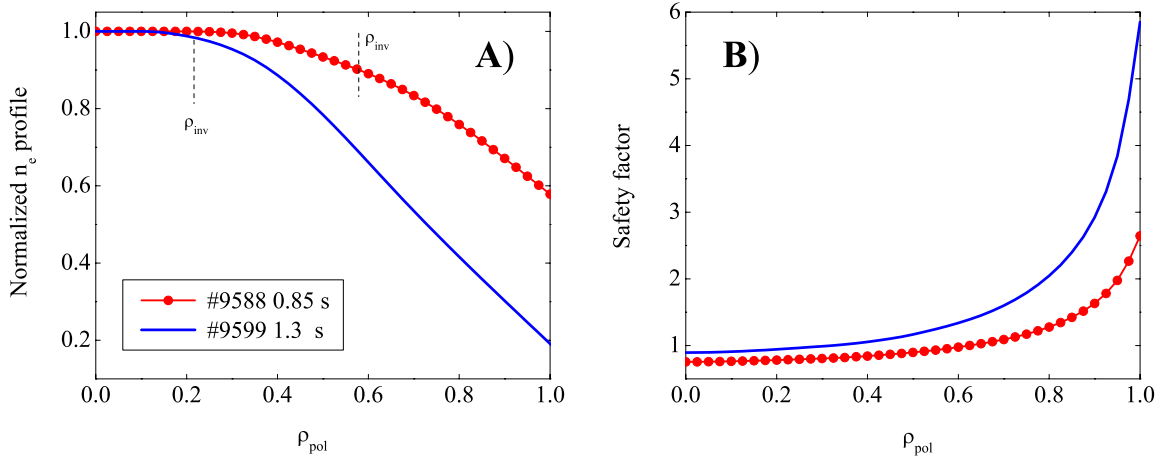
Figure 5.2: **A)** *Typical normalized electron density profiles observed in TCV Ohmic L-mode discharges. Approximate location of the sawtooth inversion radius are marked by vertical lines.* **B)** *Corresponding profiles of safety factor.*

has a density peaking factor $n_{e1}/ < ne >= 1.17$ and discharge 9599 ($I_p = 200$ kA, $n_e(0) \simeq 8.4 \cdot 10^{19}$ m^{-3}, $T_e \simeq 800$ eV) has a highly peaked profile with $n_{e1}/ < n_e >= 2.27$. The corresponding profiles of the safety factor for these discharges are shown in the Fig. 5.2B. The steeper profile of safety factor corresponds to the more peaked density profile. The scaling of the normalized density gradient defined as $R/L_n = R(dn_e/dr)/n_e$ (where R is the major radius) and evaluated in the confinement zone is shown on Fig. 5.3. The normalized gradient is clearly correlated with the edge safety factor and increases with q_{95}. These examples show that the density profiles in TCV are indeed peaked and suggest that this peaking depends on the plasma current profile.

We found that the density peaking widths correlate best with the parameter $< j > /(j_0 \, q_0)$. Here $< j >$ is a cross-sectional average toroidal current density, j_0 and q_0 respectively the current density and the safety factor on the plasma magnetic axis. Since $q_a = j_0 q_0/ < j >$ in a circular plasma [4], the parameter $j_0 q_0/ < j >$ represents a generalization to arbitrary cross sections of the edge safety factor q_a, which was previously found to provide a good scaling parameter for sawtooth inversion radii and temperature and pressure profiles in circular cross section. This is important for TCV, where the central elongation can vary from $\kappa_0 \simeq 1$ up to $\kappa_0 \simeq 2$.
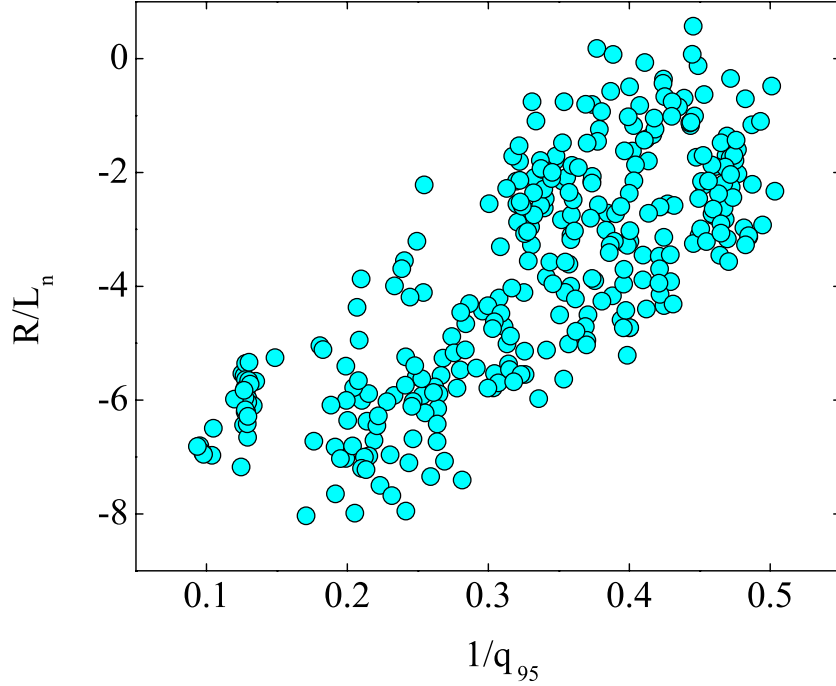
Figure 5.3: *Normalized inversed electron density gradient length evaluated at $\rho_{pol} = 0.7$ as a function of the inversed edge safety factor.*

In the case of elongated flux surfaces, Ampère's equation gives

$$j_0 = \frac{B_0(\kappa_0 + 1/\kappa_0)}{\mu_0 R_0 q_0}$$

where k_0, B_0 and R_0 are respectively the elongation, the toroidal magnetic field and the major radius at the magnetic axis. As a results, the parameter $j_0 q_0$ can be evaluated without separate knowledge of q_0 or j_0.

The scaling of the "clipped" profile widths with parameter $<j>/(j_0 q_0)$ is shown in Fig. 5.4. The density profile peaking correlates strongly with $<j>/(j_0 q_0)$ becoming broader while $<j>/(j_0 q_0)$ increases and therefore as q_{95} decreases. The observed relationship can be summarized as

$$\frac{n_{e1}}{<n_e>} \sim \frac{1}{<j>/j_0 q_0 + 0.22} \tag{5.1}$$

with standard deviation

$$\sigma = \sqrt{\frac{1}{N} \sum_N \left(\frac{n_{e1}}{<n_e>}\Big|_{experiment} - \frac{n_{e1}}{<n_e>}\Big|_{fit} \right)^2} \approx 0.04$$
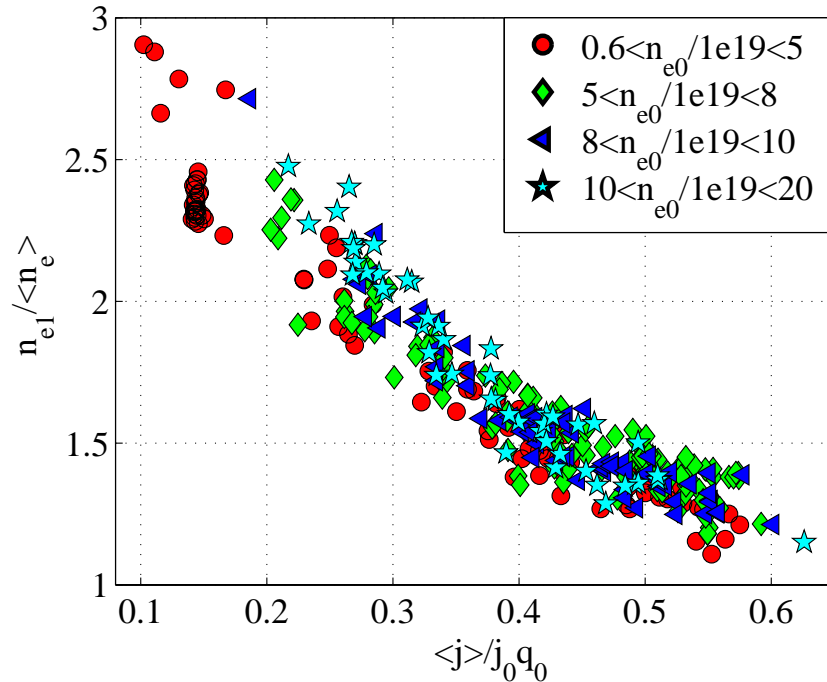
Figure 5.4: *Scaling of electron density inverse peaking factor for Ohmic L-mode discharges. Symbols refer to the classes of the central densities.*

The fact that the profiles widths give much less scatter than the gradient dependence can be explained by the spatial averaging involved in the definition of the peaking via the volume average $< n_e >$ and by the avoidance of the effect of sawtooth activity. The later limits the peaking of the profile inside of the inversion radius which also scales with $< j > /(j_0 q_0)$ [91]. As a result, the sawteeth create trapezoidally shaped profiles with a central plateau width proportional to $< j > /(j_0 q_0)$. It has to be stressed, that the effect of sawtooth "clipping" is limited since it cannot explain the scaling of the local gradients in the confinement zone (Fig. 5.3) which are only marginally affected by the sawtooth crash.

In order to demonstrate that $< j > /(j_0 q_0)$ provides the best scaling for the profile width, we performed a liner regression between $< n_e > /n_{e1}$ and other parameters which reflect the current profile peaking. Besides q_{95} and $< j > /j_0$, the internal inductance calculated by LIUQE and defined as

$$l_i = \frac{\int B_\theta^2 dV}{\oint B_\theta^2 dl} \frac{\oint dl}{\int dV},$$ (5.2)

where B_θ is a poloidal magnetic field, V is the volume and l is the contour of the LCFS,

	1	2	3	4	5	6	7	8	9
c_0	0.22 ±0.01	0.24 ±0.02	0.16 ±0.06	0.36 ±0.05	0.11 ±0.02	0.22 ±0.02	0.24 ±0.01	0.29 ±0.03	0.24 ±0.04
$< j > /(j_0 q_0)$	1 ±0.03					0.86 ±0.1	1.02 ±0.03	0.91 ±0.04	0.97 ±0.04
$1/q_{95}$		1.14 ±0.05							
$1/l_i$			0.47 ±0.06						
$< j > /j_0$				0.84 ±0.16					
$< T_e > /T_{e1}$					1 ±0.05	0.13 ±0.12			
$< n_e > /10^{20}$							−0.05 ±0.02		
$10^7 \tau_e |V_{loop}|/I_p$								−0.03 ±0.01	
$\log(\nu_{75}^*)/10$									−0.02 ±0.04
$\sigma \cdot 100$	3.88	4.5	9.2	10.3	5.02	3.86	3.82	3.78	3.88

Table 5.1: *Results of linear regression for the parameter $< n_e > /n_{e1}$. Intervals are given for the 90% confidence level. Columns #1−#5 correspond to the two parameter regression and columns #6 − #9 represents the results of the tree parameter regressions. Dataset contains 313 samples.*

is a measure of peakedness of the current profiles. Regressions #1 − #4 in Table 5.1 show that between $< j > /(j_0 q_0)$, l_i, $1/q_{95}$ and $< j > /j_0$, the parameter $< j > /(j_0 q_0)$ indeed correlates the best with "clipped" density profile width.

The results of the density profile broadening with the $< j > /(j_0 q_0)$ for TCV saw-toothing Ohmic discharges were reported in [91]. Since in sawtoothing discharges the central safety factor does not exceed unity, it was suggested in [91] that the parameter $< j > /j_0$ rather than $< j > /(j_0 q_0)$ may determine the density profile peaking for all q_0. Here we present the results over a larger range of the discharge conditions, including discharges with central safety factors above the internal kink mode stability limit $q = 1$. At high values of the edge safety factor (usually $q_{95} > 6$ for TCV) the central values of

q are often greater than one, the sawtooth activity is normally absent and the profiles in the centre have their "natural" shape determined by the plasma confinement properties rather than by the sawtooth instabilities. Table 5.1 indicates a significantly lower degree of a correlation between density profile and $< j > /j_0$ than with $< j > /(j_0 q_0)$. We should note, however, that the value of central safety factor was not directly measured and values of j_0 obtained from equilibrium reconstruction LIUQE [90] may be inaccurate.

In order to understand the particle transport in TCV, we studied different plasma parameters which can influence the density peaking. The analysis performed in [91] showed the density peaking to be independent of the plasma shape. In this study we found that the absolute value of the electron temperature as well as of the ion temperature have no influence on density peaking. At the same time, since in Ohmic discharges the electron temperature profile width is strongly correlated with $< j > /(j_0 q_0)$ [91], the density peaking is correlated with the electron temperature width $T_{e1}/ < T_e >$ (or the temperature gradient length) in the same way as with $< j > /(j_0 q_0)$ (see Table 5.1 regression #5). Nevertheless, the correlation of the density peaking with $< j > /(j_0 q_0)$ is better than with $< T_e > /T_{e1}$ (compare regression #1 and #5 in Table. 5.1). An addition of $< T_e > /T_{e1}$ to the regression

$$\frac{< n_e >}{n_{e1}} = c_1 \frac{< j >}{j_0 q_0} + c_2 \frac{< T_e >}{T_{e1}} + c_0$$

very slightly decreases the standard deviation (see column #6). The strong correlation of $< T_e > /T_{e1}$ and $< j > /(j_0 q_0)$ in stationary, inductively heated discharges makes a separation of the contribution of these two effects on density profile peaking very uncertain.

The different symbols in Fig. 5.4 refer to classes of central electron density, demonstrating that the profile widths and hence the profiles themselves are practically independent of the absolute value of the density. At fixed $< j > /(j_0 q_0)$ there is, however, a slight tendency to have lower peaking at the lowest densities, as confirmed by the negative coefficient for $< n_e >$ in the three parameter regression #7 in Table 5.1. This cannot be explained by variations of the penetration depths of neutrals, since the other quantities being constant, an increased penetration depth would be expected to lead to more peaked profiles. Therefore the overall behaviour of the peaking is in agreement with the conclusion of the previous chapter about the insignificance of the particle source in the particle
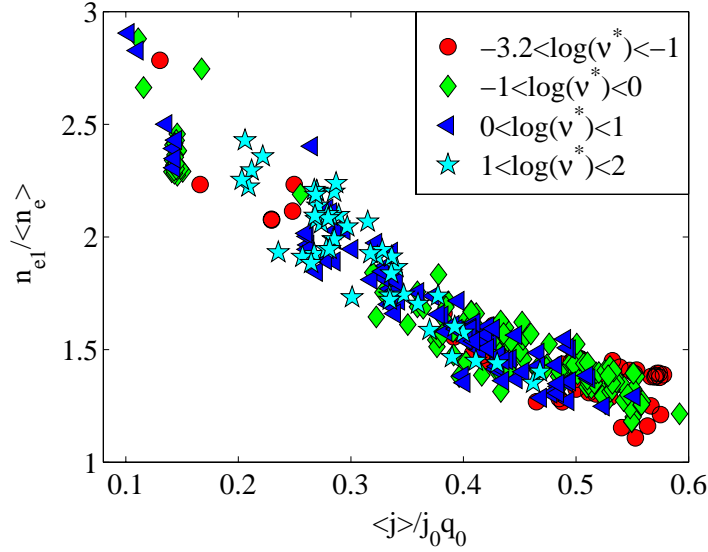
Figure 5.5: *Scaling of electron density peaking factor for Ohmic L-mode discharges. The symbols refer to the class of logarithm of effective collisionality ν^* evaluated at $\rho \sim 0.75$.*

balance and indicates the presence of an inward particle pinch.

In order to understand the importance of Ware pinch on the density peaking we constructed the parameter

$$\tau_e \cdot V_{loop} \cdot \frac{1}{I_p} \propto \frac{1}{\chi_e} \cdot E_\parallel \cdot \frac{1}{B_p} \propto \frac{V_{Ware}}{D} \qquad (5.3)$$

where V_{loop} is the loop voltage, related to the parallel electric field E_{II} as $V_{loop} = 2\pi R E_{II}$ (R is the major radius), I_p is the plasma current proportional to the poloidal magnetic field B_p and

$$\tau_e = \frac{3}{2} \frac{\int T_e n_e dx^3}{P_{OH}} = \frac{3}{2} \frac{\int T_e n_e dx^3}{I_p V_{loop}} \qquad (5.4)$$

is the electron energy confinement time inversely proportional to the electron heat conductivity coefficient χ_e by analogy with Eq. 3.1. In Eq. 5.3 we assumed a direct proportionality between D and χ_e in accordance with the results in Refs [20, 84, 92]. In steady state the effect of V_{Ware}/D on $\nabla n_e/n_e$ is additive (see Eq. 3.15) and therefore the dependence of the density peaking on $\tau_e V_{loop}/I_p$ is expected to reflect the influence of the neoclassical Ware pinch on the density peaking. The three parameter regression #8 in Table 5.1, with $\tau_e V_{loop}/I_p$ taken in addition to $< j > /(j_0 q_0)$, has a slightly lower σ than in the regression #1. The coefficient for $\tau_e V_{loop}/I_p$ is negative signifying an increase of

the density peaking when the parameter $\tau_e V_{loop}/I_p$ (and therefore Ware pinch) increases. However this effect is small, leaving only a secondary role in total inward convection to the neoclassical Ware pinch.

As it was shown in chapter 3, the collisionality parameter ν^* determines the transport regime and corresponding transport coefficients in the case of neoclassical transport. It is also closely related to ν_{eff} (see Eq. 3.10), which is a fundamental parameter for drift wave growth rates. The three parameter linear regressions #9 in Table 5.1 with the logarithm of ν_{75}^* as a secondary parameter, show that despite of the correlation of ν_{75}^* with $< j > /(j_0 q_0)$, ν_{75}^* has no noticeable influence on the density peaking. To illustrate this independence in Fig. 5.5 we presented the density peaking dependence on $< j > /(j_0 q_0)$ resolved into classes of logarithm of ν_{75}^*.

5.2.2 Density response to plasma current modulation

In order to verify whether the observed correlation of the density peaking and parameter $< j > /(j_0 q_0)$ is peculiar only to the steady state or if it holds also in non stationary conditions, we performed plasma current modulation experiments.

An example of total plasma current variation in Ohmic L-mode discharge is shown in Fig. 5.6A. The changes of plasma current from about $120 \ kA$ to $200 \ kA$ with an average frequency of $30 \ Hz$, leading to a variation of the edge safety factor from 9 to 4. The response of the electron density peaking on the current modulation obtained using SVD-I inversion with three topos is shown in Fig. 5.6A. The density profile becomes flatter as the current profile becomes flatter as a result of the decrease in the edge safety factor, in agreement with observations in steady state conditions. To clearly reveal this concordance we plotted in Fig. 5.6B as solid line the evolution of the profile peaking during the modulation experiment, together with the scaling observed in steady state (dots). For all six modulation cycles shown, the initial high peaking at $< j > /(j_0 q_0) \simeq 0.15$, decreases during the positive current ramp and goes up during the negative ramp following on the way back practically the same trajectory. Evidently, the general behaviour of the peaking during the modulations remains the same as in steady state, following, with small deviation the line $1/(< j > /(j_0 q_0) + 0.22)$. One possible explanation for this
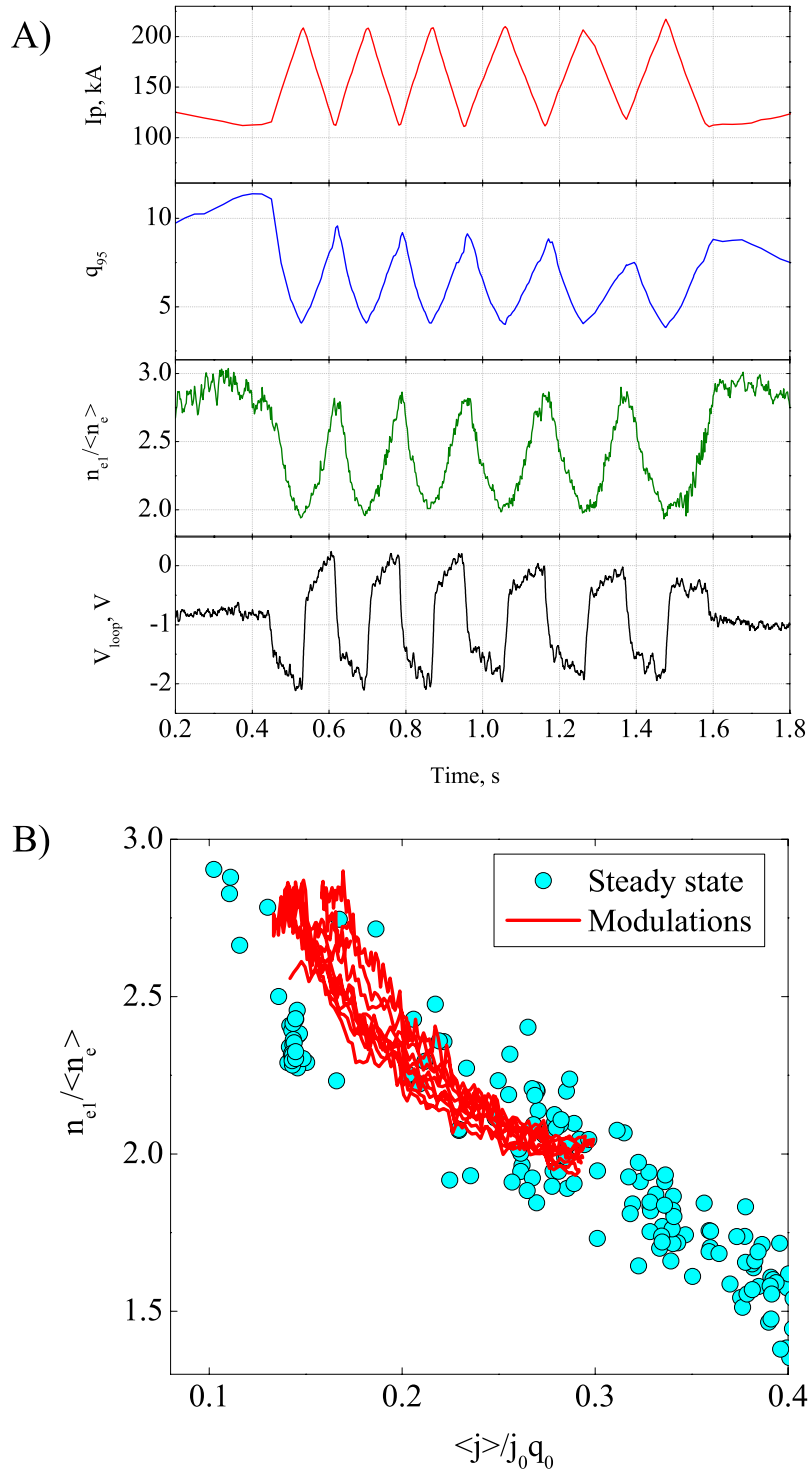
Figure 5.6: **A)** *Temporal behaviour of measured plasma current, safety factor calculated at 95% of the poloidal flux, measured surface loop voltage and clipped density profile peaking* **B)** *Density profile peaking in Ohmic L-mode steady state discharges (dots, as Fig. 5.4) together with the traces of the peaking changes in the modulation discharge.*

deviation is the fact that during the modulations which are faster than current diffusion time ($\sim 150\ ms$) the parameter $< j > /(j_0\ q_0)$ may not be appropriate for describing the current profile width. Another uncertainty can be related to a fallibility of the SVD-I reconstruction as results of incompleteness of the base functions due to limited number of the Thomson density profiles measurement available during the modulation phase. However, the same dependence of the inversed peaking on $< j > /(j_0 q_0)$ is observed in other discharges with a different timing of modulations and as a consequence with a different initial matrix of Thomson n_e profiles used for SVD-I.

It is interesting to note that the changes of the density peaking are as fast as the current modulation with the maxima of the peaking corresponding nearly exactly to the minima of the plasma current (or maxima of edge safety factor). This indicates that if the density profile is fully determined by the current profile, the particle transport during the modulation has to be faster than a plasma current diffusion time.

The total changes in peaking during the modulation cycle exceed the uncertainties of the $n_{e1}/ < n_e >$ scaling with the current width in steady state and cannot be explained only by changes of the absolute values of density. During the modulation, the temperature profile, as in the case of steady state, closely follows the current profile, becoming broader as the current profile flattens. Because of this correlation it seem to be difficult to separate a possible influence of the temperature on the density profile from the effect of the plasma current profile.

A comparison of the time traces of the loop voltage and density peaking on Fig. 5.6A reveals a phase shift corresponding to half of the modulation period. The loop voltage at the plasma surface obtained from magnetic measurements has a minimum at $-2\ V$ during the current increase phase and a maximum $+0.2\ V$ during the negative current ramp. According to the neoclassical theory, the inward Ware pinch, which is proportional to the loop voltage, would lead to a more peaked density profile at the minimum loop voltage. The experiments, however show that the density becomes broader at the positive current ramp in a contradiction with the behaviour expected from the neoclassical pinch. Nevertheless, to clarify the role of the neoclassical convection an additional modelling of the profile of Ware pinch is needed.

5.3   Electron density profiles in ECRH discharges

The experimental observations in ECRH heated discharges in TCV show that additional heating affects the electron density profile. In general, in the absence of MHD activity or strong internal transport barriers (ITB), additional electron heating leads to a broadening of Ohmic target plasmas profiles.

As an example, the temporal behaviour of the plasma current, ECRH power and density peaking in TCV L-mode discharge are shown on Fig. 5.7. The plasma current and the edge safety factor remain nearly constant during heating phase of the discharge. Variations of the central density do not exceed 20% around the average of $2.5 \cdot 10^{-19} \ m^{-3}$.

In the Ohmic phases, at the beginning and at the end of the discharge, the density profiles are peaked, in agreement with the scaling described in the previous section. The addition of 1.3 MW of ECRH power with a broad deposition profile ($\rho_{pol} \approx 0.1 - 0.7$ according to TORAY-GA) decreases the peaking by about 30%. The power step up to 2.6 MW at $t = 0.7 \ s$ with a similar deposition profile increases the central temperature up to 6 keV, but does not lead to further significant changes of the density profile width. The overall behaviour shows that the density profiles in the presence of ECRH heating become broader in comparison with the Ohmic target profiles.

From Fig. 5.7 it is seen that the absolute value of the central temperature, at least when it is higher than few keV, does not have an influence on the density profile, since no major changes of the density peaking are observed when the absolute value of the temperature changes from 4 keV to 6 keV at the second power step. This stiffness of the density profile is even more striking in the discharges with improved central electron confinement with weak electron internal transport barriers (eITB). In eITB discharges the low shear is believed to result in a suppression of the turbulence in the plasma core inducing a local reduction in the transport coefficients and the formation of a transport barrier revealed by steep localized density and/or temperature gradients [48–50]. The TCV weak eITB regime is characterised [93–95] by the confinement enhancing factor

$$H_{RLW} = \frac{\tau_e}{\tau_{RLW}} < 2.5$$

where τ_e is the electron energy confinement time and τ_{RLW} is confinement time predicted
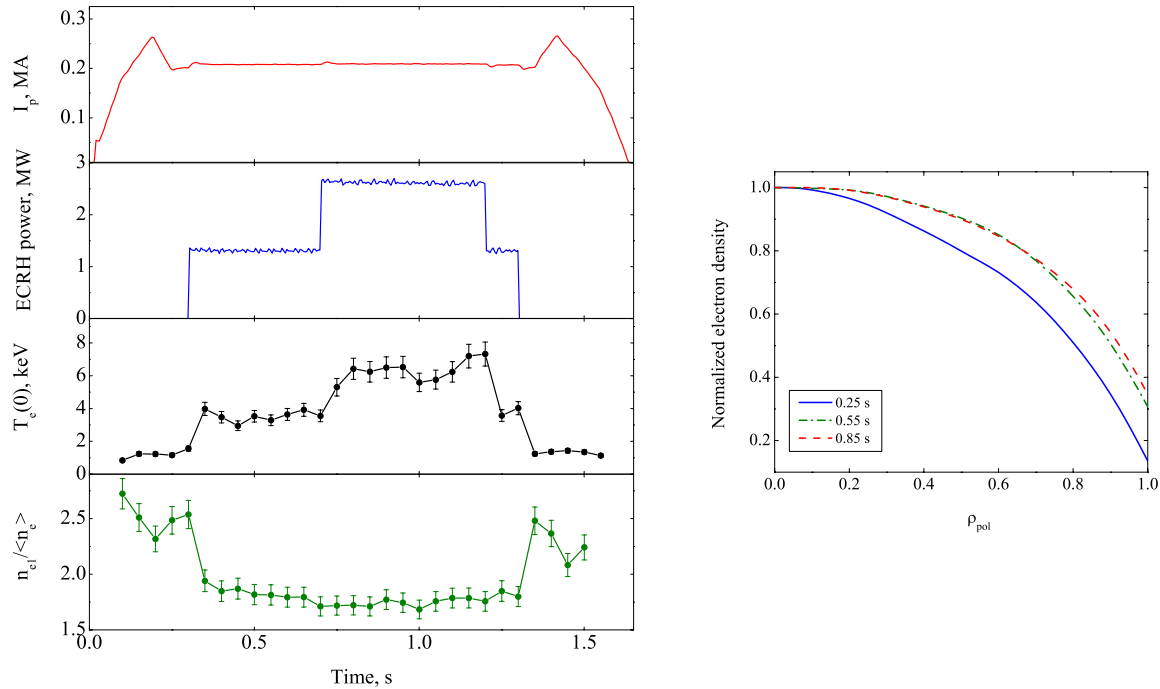
Figure 5.7: *Left: Temporal behaviour of plasma current, ECRH power, central electron temperature and electron density peaking in ECRH L-mode discharge #18224. Right: Normalized fits of TS electron density profiles for three time moments.*

by the semi-empirical Rebut-Lallia-Watkins scaling [96]. In discharge #24712 we selected for illustration, a target plasma with plasma current $I_p = 0.14\ MA$, elongation $\kappa \simeq 1.56$, triangularity $\delta \simeq 0.56$, $q_{95} \simeq 8$, preheated with off-axis ECRH ($\rho_{dep} \simeq 0.7$, power density $5.1\ MW/m^3$) and after adding on-axis counter ECCD heating with a power density about $36\ MW/m^3$ a quasi-stationary, weak eITB regime with and $H_{RWL} \simeq 2.2$ was obtained. In Fig. 5.8 the profiles of the electron density and electron temperature in the preheating phase are compared with those in the weak eITB phase. The electron temperature profile in eITB phase (later profile in Fig. 5.8) is stiff outside the eITB and is strongly peaked in the centre, with the maximum temperature exceeding more than 5 times the maximum of the temperature in L-mode. The electron density in contrast, shows a very stiff behaviour, remaining unchanged not only in confinement zone but also in the central region.

A comparison of the different ECRH power steps in the example on Fig.5.7, especially the lack of density response to the power increase from $1.3\ MW$ to $2.6\ MW$, indicates that the absolute value of the power does not have a noticeable influence on the density
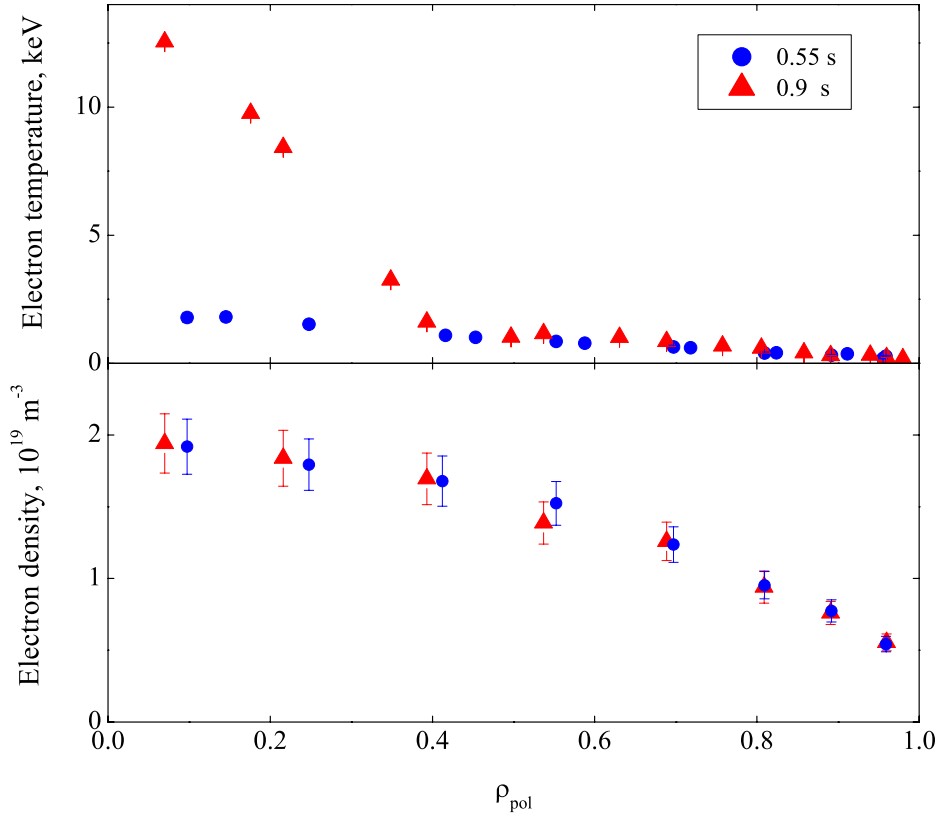
Figure 5.8: *Electron temperature (top) and electron density (bottom) TS profiles in two phases of discharge #24712. The profiles at 0.9 s correspond to weak ITB regime. Smaller number of points on density profiles than number of temperature measurements is caused by absence of correct absolute calibration for some of the TS channels*

profile. However, in this example the deposition location is very broad and changes during the discharge. In order to illustrate the rigidity of the stationary density profiles to the increase of the heating power for a narrow deposition location and with the same deposition profile, we selected two off-axis heated discharges, #25405 and #25417, with similar plasma shape, a similar line average density ($1.1 \cdot 10^{-19}$ m^{-3} and $1.4 \cdot 10^{-19}$ m^{-3} respectively) and an identical plasma current $I_p \sim 0.22$ MA. The discharge #25405 has 0.75 MW of ECRH power coupled to the plasma and the discharge #25417 has a power of 2.4 MW. According to TORAY-GA calculations in both discharges power was deposited at $\rho_{pol} \simeq 0.5$ (Fig.5.9 bottom) and in both discharges the fraction of current drive can be neglected. The electron temperature profiles shown in Fig.5.9 on a logarithmic scale at the top of the figure have similar normalized dimensionless gradients $R/L_{T_e} = R(dT_e/dr)/T_e$
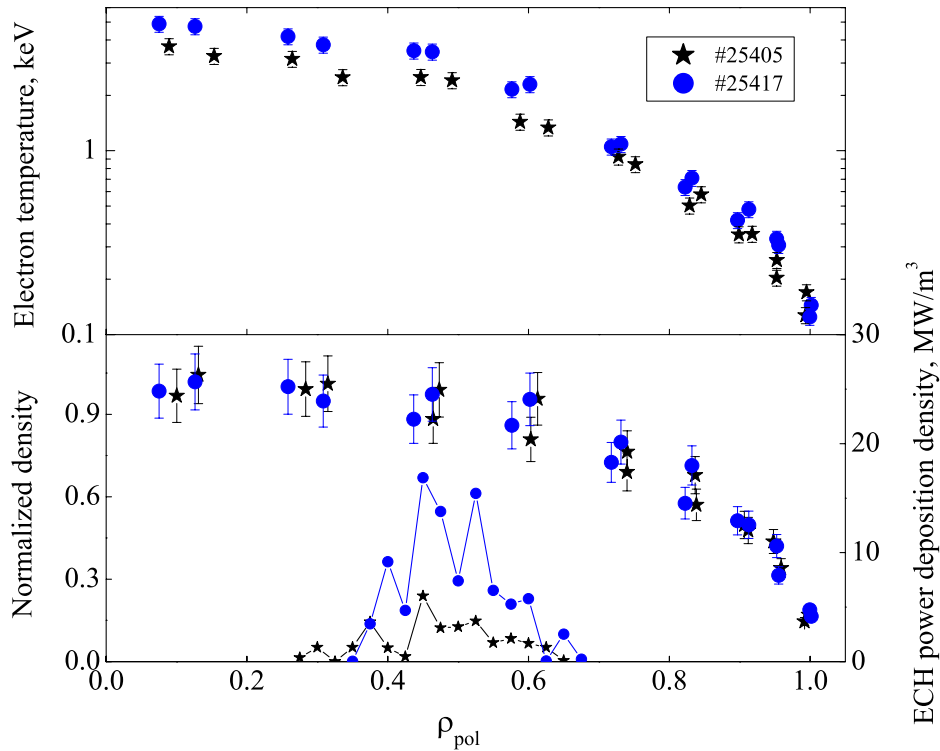
Figure 5.9: *Electron temperature TS profiles on a logarithmic scale, normalized profiles of electron density from TS and deposition profiles from TORAY-GA for discharges #25405 and #25417.*

(where R is the major radius). The normalized density profiles shown on the bottom of the figure are practically identical for both discharges, confirming the stiff behaviour of density in response to the strong increase of the heating. We should note, however, that minimum ECRH power tested in this work was equal to 0.45 MW and therefore we cannot exclude any dependencies which might occur at lower power.

The observed independence of the density peaking on the absolute value of the temperature as well as its independence on the absolute level of deposited power leads to an important conclusion about the relation between the heat and the particle transports. The heat balance shows a significant increase of electron heat conductivity in response the temperature or heating power increase. The stiffness of the density profiles as a response to the increased heat diffusion indicates that if there is a direct link between the heat and particle transport diffusion $D/\chi_e = const$ as suggested for example in Refs. [84, 92, 97], the pinch velocity must change in respond to ECRH in order to keep the same steady
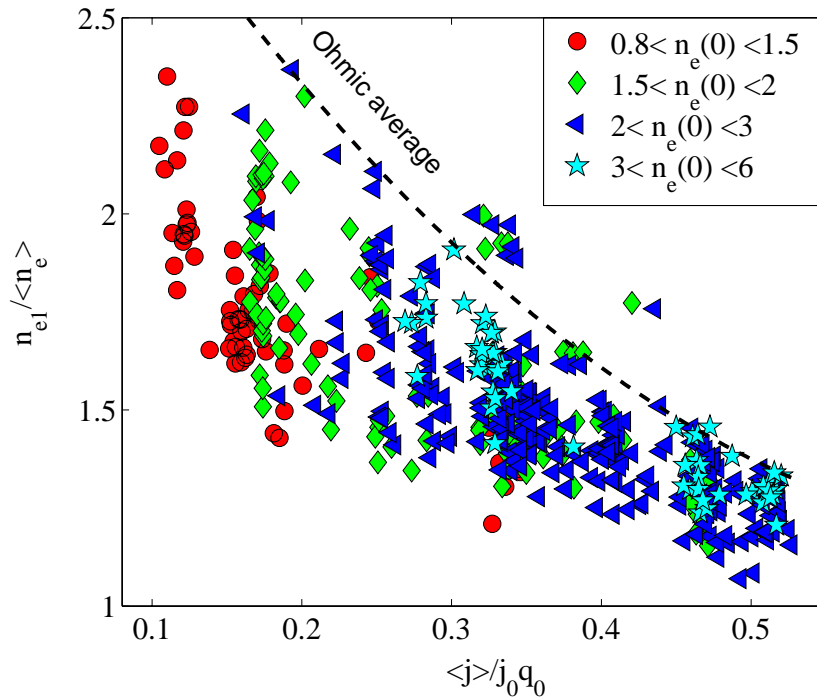
Figure 5.10: *Scaling of electron density peaking in ECRH discharges with edge safety factor $< j > /(j_0 q_0)$. Symbols separate classes of central densities.*

state density profile ($\nabla n/n = V/D$).

A broad study of the electron density peaking dependence on plasma parameters in ECRH plasmas was performed using profiles from a database containing about 600 profiles from ECRH discharges with additional heating provided by up to 6 gyrotrons operating at a frequency of 82.7 GHz corresponding to the second electron cyclotron frequency harmonic in TCV. The ECRH database covers a range of $0.9 \cdot 10^{19} \leq n_e(0) \leq 3 \cdot 10^{19}$ m^{-3}, $0.02 \leq \nu_{75}^* \leq 1$, $1.2 \leq \kappa_a \leq 2.3$, $3 \leq q_{95} \leq 20$. All discharges were limited L-modes in steady-state, with ECRH powers up to 2.7 MW (up to thirteen times the power of the Ohmic target discharges). The majority of the discharges presented in the database are on- and off-axis ECRH discharges with a fraction of current drive calculated by TORAY-GA of less than 10% of total plasma current. However, we included in the analysis some cases with substantial electron cyclotron current drive, both in co- and counter directions.

The dependence of the density peaking width on the parameter $< j > /(j_0 q_0)$ in ECRH discharges is shown in Fig. 5.10. The average peaking of the Ohmic target discharges obtained from Fig. 5.4 is plotted as a dashed line. As seen from the figure, the ECRH

leads in general to a broadening of the density profile. At fixed $< j > /(j_0 q_0)$ the peaking can be as low as 60% of the peaking in the Ohmic target discharge. However in some isolated cases, the ECRH can increase the peaking above the Ohmic target value.

We found a general dependence of the peaking on current profile width (Fig. 5.10), similar to the Ohmic case, where on average, higher peaking of density correlates with a higher peaking of the plasma current profile,

$$\frac{n_{e1}}{< n_e >} = \frac{1}{0.72 < j > /(j_0 q_0) + 0.44} \tag{5.5}$$

At the same time, the significant vertical scatter of the data at fixed $< j > /(j_0 q_0)$, which is well beyond the errors, estimated to be less than 15%, indicates that $< j > /(j_0 q_0)$ is no longer the only scaling parameter. Among other parameters such as V_{loop}, $< n_e >$, ν_{75}^*, $< T_e > /T_{e1}$, P_{ECRH}, ρ^*, tested using two parameter linear regressions, none was found to provide a statistical meaningful alternative to $< j > /(j_0 q_0)$. The possibility of dependence in addition to $< j > /(j_0 q_0)$ was studied using three parameter regression in the form (example for V_{loop})

$$\frac{< n_e >}{n_{e1}} = c_1 \frac{< j >}{j_0 q_0} + c_2 V_{loop} + c_0 \tag{5.6}$$

and the results are presented in Table 5.2.

A remarkable decrease of σ, more than 25 %, is observed when ρ_{dep} is chosen as a secondary parameter in these multiple linear regression (regression # 4). Here, the ρ_{dep} corresponds to the maximum of the deposition profile calculated by TORAY-GA. Only discharges with narrow deposition profiles were taken into account, thus ρ_{dep} is meaningfully representative of the heating location. This particular dependence of the density profile peaking on the deposition location is illustrated in Fig. 5.11. In discharges presented the density profiles broadens as deposition location is moved towards the centre. It is interesting to note that the normalized gradient of the density outside $\rho_{pol} = 0.8$ is independent on ρ_{dep} and the main changes of the profiles occur for $0.2 < \rho_{pol} < 0.6$ i.e. in the region where the gradient of the electron temperature has maximum changes.

In order to discriminate the dependencies on ρ_{dep} in the database, we scaled out the dependence of $n_{e1}/ < n_e >$ on $< j > /(j_0 q_0)$ by dividing the density peaking by the
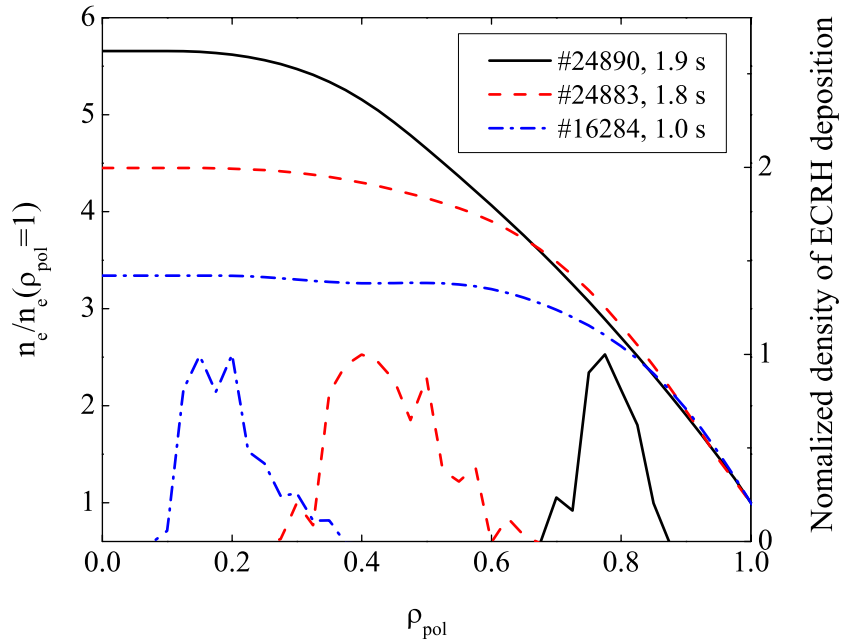
Figure 5.11: *Fits of TS electron density profiles normalized to the edge value, together with the profiles of ECRH power density (calculated by TORAY-GA) in three L-mode discharges performed at a plasma current $I_p \approx 0.21\ MA$. Discharge #24890 has central density $n_e(0) \simeq 2.1 \cdot 10^{19}\ m^{-3}$, #24883 has $n_e(0) \simeq 1.2 \cdot 10^{19}\ m^{-3}$ and #16284 has $n_e(0) \simeq 2 \cdot 10^{19}\ m^{-3}$.*

average density peaking from Eq. 5.5. The relation of this quantity $peaking/peaking_{avg}$ and the ECRH power deposition location is shown in Fig. 5.12. It is clearly seen that the density peaking decreases when deposition becomes more central, depending almost linearly on ρ_{dep}. The lowest peaking in ECRH L-mode discharges is observed for on-axis deposition. At the same time, for far off-axis heating, the peaking can be slightly higher than the average Ohmic peaking, although the quality of the data does not allow to unambiguously prove this surplus of peakedness. The symbols in the Fig. 5.12 correspond to classes of different central electron temperature. The trend to have a lower peaking at higher temperatures is most likely related to the difficulty of obtaining high central temperatures with off-axis heating rather than to a particular relation between density peaking and central temperature. This is confirmed by the fact that discharges with very different temperatures can have the same density peaking. The density peaking was also found to be independent of the value of the average temperature gradient in the region $0.2 < \rho_{pol} < 0.5$, estimated using TS temperature profiles.

	1	2	3	4	5	6	7
c_0	0.44 ±0.01	0.45 ±0.01	0.44 ±0.02	0.45 ±0.02	0.44 ±0.01	0.41 ±0.02	0.4 ±0.02
$<j>/(j_0 q_0)$	0.72 ±0.04	0.79 ±0.06	0.73 ±0.04	0.9 ±0.1	0.72 ±0.04	0.74 ±0.09	0.71 ±0.04
$<T_e>/T_{e1}$		−0.07 ±0.07					
$10^6 \tau_e |V_{loop}|/I_p$			0.05 ±0.09				
ρ_{dep}				−0.2 ±0.02			
$<n_e>/10^{20}$					−0.02 ±0.09		
$P_{ECRH},\ MW$						0.02 ±0.01	
$\log(\nu_{75}^*)$							−0.02 ±0.01
$\sigma \cdot 100$	4.91	4.89	4.91	4.14	4.91	4.79	4.78

Table 5.2: *Results of linear regression for $<n_e>/n_{e1}$ in ECRH discharges. Intervals are given for the 90% confidence level. Dataset contains 525 samples.*

The symbols in the Fig. 5.10 refer to classes of the central density. It is seen that samples with the same central densities are spaced over the entire range of the observed density peaking. An apparent prevalence of low density discharges at low current is circumstantial and related to peculiarities of the TCV scientific program. The lack of a relation between the absolute value of the density and density peaking is confirmed by the regression #5 in Table 5.2. Thus, as in the case of the Ohmic discharges and in agreement with the results of chapter 4, we can conclude that the penetration of edge neutrals is not responsible for the observed density peaking and must be due to an inward pinch.

The separation by the ratio of the ECRH power to the power in Ohmic target discharges shown in Fig 5.13A and B confirms the independence of peaking on the absolute value of the ECRH power. On both graphs a predomination of the high ECRH power points in the on-axis region of deposition locations and in the low plasma current range is related to the TCV experimental program and not to a specific power dependence.
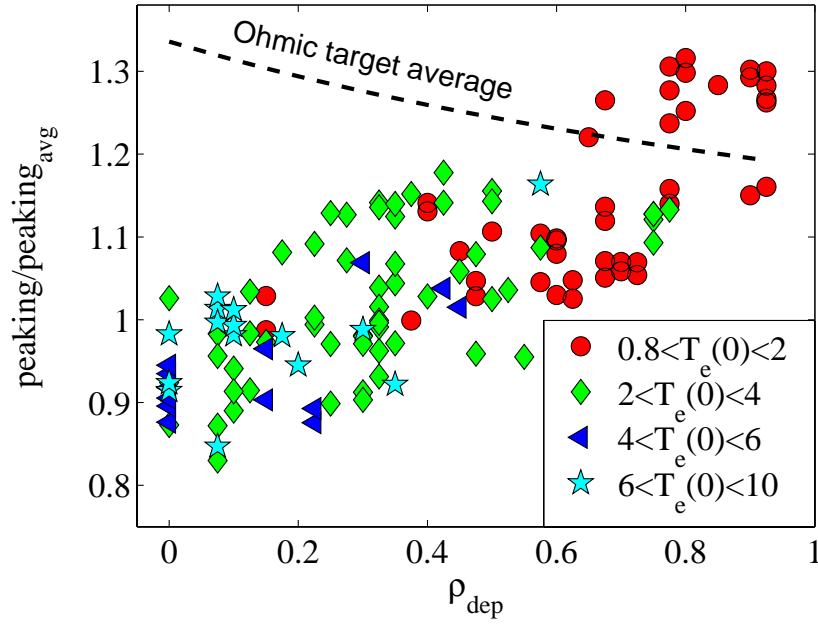
Figure 5.12: *Scaling of the parameter peaking/peaking$_{avg}$ with ρ_{dep} (see definitions of ρ_{dep} in the text) in ECRH discharges. Symbols refer to the classes of the central temperatures in keV.*

Indeed, as seen in both figures, discharges with P_{ECRH}/P_{OH} differing by an order of magnitude can still have the same density peaking. A similar conclusion holds not only for the ratio P_{ECRH}/P_{OH} but for P_{ECRH} alone as is shown by regression #6 in Table 5.2.

The dependence of the density peaking on the loop voltage measured at the plasma surface is shown by the classes of symbols on Fig. 5.13C. Since in the majority of ECRH heated discharges an important fraction of the plasma current is still Ohmic current, the loop voltage itself correlates with $< j > /(j_0 q_0)$. The correlation of $n_{e1}/ < n_e >$ with V_{loop} is significantly lower, which indicates the lack of direct importance of V_{loop} in density peaking. The three parameter regression with $\tau_e V_{loop}/I_p$ (Eq. 5.3) as secondary parameter shows no evidence of the Ware pinch influence on the density peaking (regression #3 in Table 5.2).

The dependence of the density peaking on $log(\nu^*_{75})$ is shown by the classes of symbols on Fig. 5.13D indicating that, as in the case of Ohmic discharges, during ECRH $log(\nu^*_{75})$ and $n_{e1}/ < n_e >$ are not directly correlated. Three parameter regression #7 in Table 5.2 show very weak secondary effect $log(\nu^*_{75})$ which at the limit of statistical significance.

Since we did not find any important dependencies other than on $< j > /(j_0 q_0)$ and

on ρ_{dep} we summarised the observations in the following empirical scaling of the density peaking in ECRH L-mode discharges

$$\frac{n_{e1}}{<n_e>} = \frac{1}{0.9 <j>/j_0 q_0 - 0.2 \cdot \rho_{dep} + 0.45} \qquad (5.7)$$

It has to be noted, that the ρ_{dep} dependence may reflect effects which we were not able to address in this study. For example, the current profile modifications caused by additional heating cannot be described by a single parameter such as the edge safety factor or the current profile width defined as $<j>/(j_0 q_0)$. In this case, even if the density profile is fully determined by the current profile, a dependence additional to $<j>/(j_0 q_0)$ dependence would appear in the experimental scaling. To determine the origins of the electron density peaking in ECRH discharges, measurements of the current profile would be needed.

5.3.1 Effects of density pumpout and of strong eITB

In this section we will illustrate the consequence of two phenomena which can lead to density profiles which are very different from those discussed above. The detailed analysis of these cases lies outside the scope of this thesis.

One of these effects is known as 'density pumpout' was observed tokamaks [98–100] in a variety of plasma conditions. There is some confusion as to the terminology. At ASDEX Upgrade, the word 'pumpout' is used to describe a reduction of the peakedness with $\nabla n_e \leq 0$ [101]. We shall refer to 'pumpout' only when sufficiently strong outward convection leads to positive ∇n_e [100].

The 'pumpout' phenomenon causes inverted sawteeth of the central density in sawtoothing discharges and leads, in the absence of sawteeth, to steady state hollow density profiles. Fig. 5.14A shows a typical example of the stationary TCV electron density and the temperature profiles during density pumpout. This discharge, performed at 180 kA of plasma current, was centrally heated with 2.5 MW of ECRH power. The density profiles in the pumpout phase are hollow enough to allow the density gradient reversal in the core to be confirmed by the Thomson scattering system. At the same time the profile of the electron temperature remains peaked (Fig. 5.14A). The density profiles in
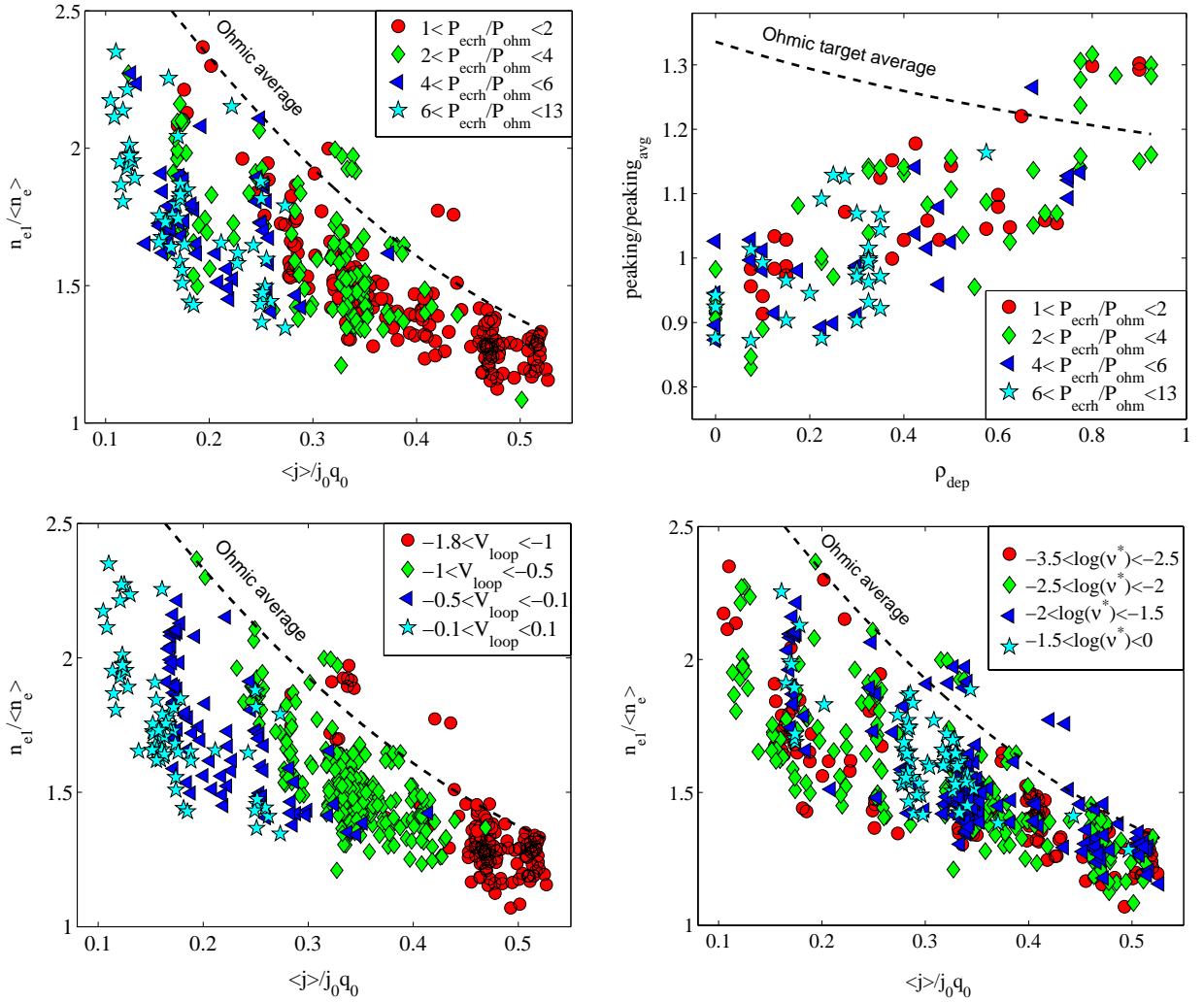
Figure 5.13: *Density peaking in ECRH discharges as a function of $<j>/(j_0q_0)$ (top left) and ρ_{dep} (top right) resolved in the classes of the ratio of ECRH power to Ohmic power in the target: P_{ECRH}/P_{Ohm}. Density peaking in ECRH discharges as a function of $<j>/(j_0q_0)$ resolved in the classes of V_{loop} (bottom left) and $\log\nu^*$ evaluated at 75 % of poloidal flux (bottom right)*

.

the discharges with pumpout have visibly lower peaking than average ECRH discharges falling out from the general scaling as it is shown in Fig. 5.14C and D. From Fig. 5.14D it is seen also that density pumpout is observed on TCV only with centrally deposited electron cyclotron heating and electron cyclotron current drive, in accordance with earlier observations in TCV [100].

Among the proposed explanations for density pumpout one is based on neoclassical
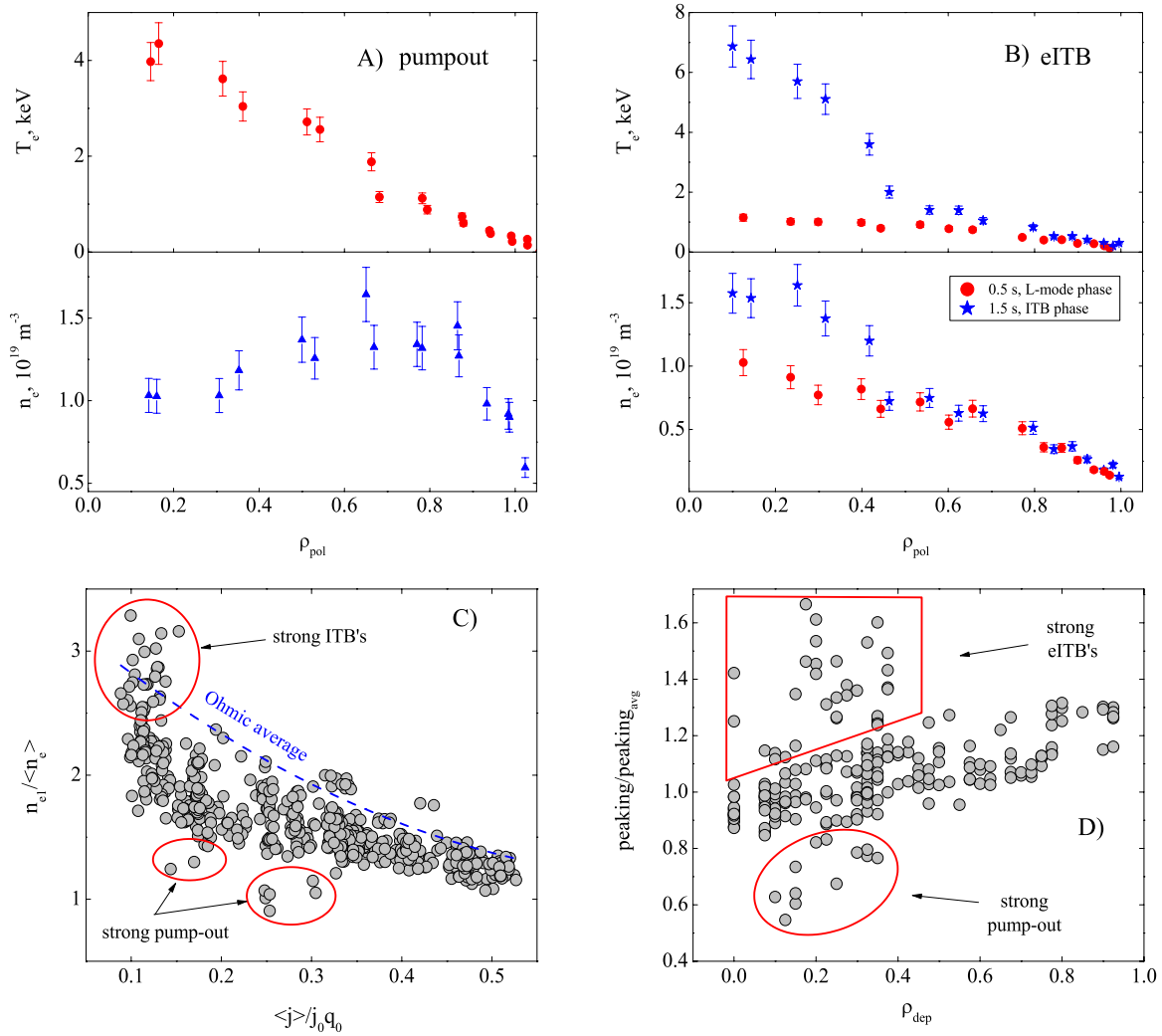
Figure 5.14: **A)** *Profiles of the electron temperature and the electron density in the discharge with density pumpout #18505 at 1 s. This discharge has quasi-permanent m=1 MHD mode visible on SXR diagnostic.* **B)** *Profiles of the electron temperature and the electron density in the discharge with eITB #26033. Scaling of the density peaking with $< j > /(j_0 q_0)$* **(C)** *and ρ_{dep}* **(D)**. *Discharges with eITB's and with density pumpout are encircled.*

transport processes involving locally trapped particles in the presence of m=n=1 MHD modes [100], as indeed observed in the example of Fig. 5.14A. The presence of MHD activity may be responsible for the observed striking difference between the peaking obeying the general scaling and peaking in discharges with the pumpout.

Another effect, which leads to an increase of the density peaking, is caused by a strong electron internal transport barrier. The presence of strong eITB's involves a significant

reversal of the central magnetic shear. In TCV strong eITB are obtained in low current discharges (usually $I_p < 120\ kA$) using central ECCD [93, 102]. During strong eITB's in TCV the confinement enhancing factor H_{RLW} is usually higher than 2.8 [93] in contrast to the weak eITBs described in section 5.3 for which $H_{RLW} < 2.5$. Fig. 5.14B shows an example of density and temperature profiles in a discharge with a plasma current $I_p = 110$ kA in which a combined effect of on-axis ECH and off axis co-ECCD (1.3 MW) created an eITB at $\rho_{pol} \simeq 0.5$ with $H_{RLW} \simeq 3.5$. The local change of ∇T_e from $\rho_{pol} \simeq 0.5$ during the eITB phase of the discharge is clearly observed. A local change of the density gradient, with an increased profile peakedness, although less pronounced, is observed on the electron density profile. Once the eITB is formed, the gradients of the density profiles remain constant for as long as the duration of the power pulse, typically over 300 energy confinement times.

As in the case of pumpout, the peaking of the density during strong eITB departs from the general scaling for ECRH discharges. As seen from Fig. 5.14, discharges with eITB's are more peaked even than Ohmic target discharges, reaching $n_{e1}/ < n_e > \sim 3.5$ in extreme cases. All the points on this scaling which have strong eITB's, are located in the low current region because of the limitation of the TCV current drive system to produce strong reversal of the shear at high plasma current. The peaking in strong eITB discharges seems to be independent of $< j > /(j_0 q_0)$ or ρ_{dep} and the scatter of the data is most likely related to the eITB strength controlled by many parameters such as heating power, counter ECCD deposition radius, the toroidal angle of the central heating beams etc.

5.4   Testing the pinch models

It is widely accepted that peaked electron density profiles in tokamak plasmas results from an inward particle pinch [9]. However, the nature of this pinch remains unknown. To explain peaked density profile behaviour in TCV discharges, the three pinch mechanisms, thermodiffusion, turbulent equipartition and the Ware pinch have been tested. For this purpose, the particle balance equation with an anomalous diffusion coefficient D and an

apparent convective inward pinch velocity V

$$\Gamma_e = -D\nabla n_e + V n_e$$

where Γ_e represents the total flux of electrons and V contains all non-diagonal terms of the transport matrix, was expanded under steady-state conditions according to the formalism of each model:

$$\frac{1}{n_e}\frac{\partial n_e}{\partial\rho} = \frac{1}{<|\nabla\rho|>}\frac{V_{Ware}}{D(\rho)} + c_q\frac{1}{qH}\frac{\partial qH}{\partial\rho} + \alpha\frac{1}{T_e}\frac{\partial T_e}{\partial\rho} \tag{5.8}$$

In this equation c_q and α are equipartition and thermodiffusion coefficients respectively, V_{ware} is the neoclassical Ware pinch velocity, q is the safety factor and $<>$ means an average over the flux surface. The geometrical factor $H = B_0 dVol/(2R_0 d\rho)$, where Vol, B_0 and R_0 are the plasma volume, toroidal flux, toroidal magnetic field and major radius at the magnetic axis respectively, is equal to unity in the large aspect ratio limit [19]. The particle source term was omitted in the Eq. 5.8 in accordance with the results of chapter 4 and with the observations presented in sections 5.2 and 5.3. We assumed all plasma parameters to be constant on the flux surfaces, labelled by ρ. The main goal of the study is to find the empirical transport coefficients, of the above form, which best fit the observations.

5.4.1 The Ware pinch in stationary Ohmic discharges

The drift velocity corresponding to the neoclassical Ware pinch is equal to $V = f_t f_\nu V_{Ware}$ (see section 3.3.1). In order to derive $\nabla n/n$ from the particle balance equation in steady state one has to choose the value of D, which a priori is unknown. However, it was suggested that there might be a relation between heat and particle diffusiveness [20, 83, 84, 92, 97]. Therefore, the particle diffusion coefficient is usually chosen to be proportional to the heat diffusion coefficient. For example ASDEX reports [92] that, at least in some cases, it is sufficient to invoke the Ware pinch together with a diffusion coefficient which is typically 1/4 of the electron heat diffusivity to explain the observed density peaking.

To estimate the contribution of the neoclassical pinch to the density peakedness, we selected a particular Ohmic L-mode discharge with $<j>/(j_0 q_0) \simeq 0.4$ and relatively high electron density. According to the calculations performed in chapter 4, high density

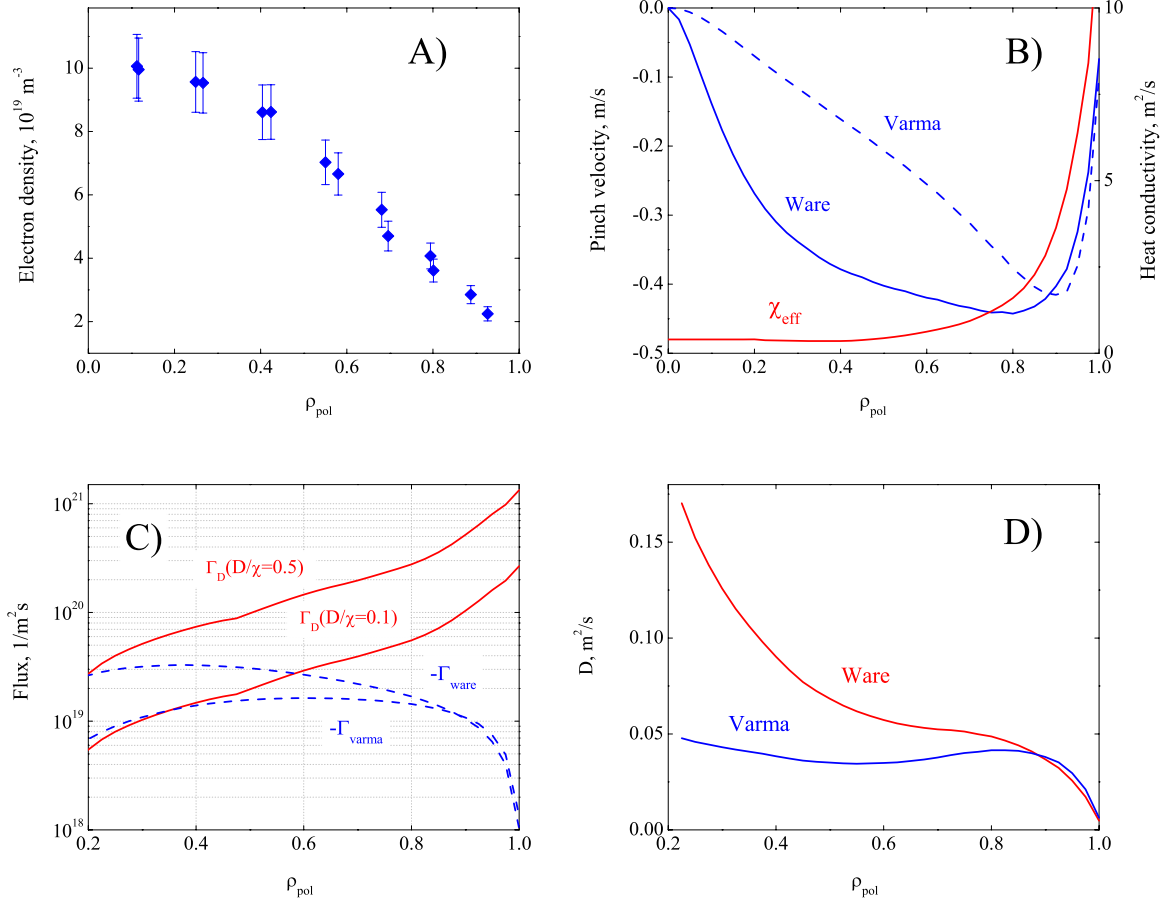Figure 5.15: **A)** *Experimental density profile in the Ohmic L-mode discharge #11103 at 0.7 s ($< j > /(j_0 q_0) = 0.29$, $n_{e1}/ < n_e >= 2.23$).* **B)** *Radial profiles of Ware and Varma pinches as well as profile of effective heat conductivity.* **C)** *Particle fluxes corresponding to pure diffusion for different values of D/χ_{eff} (solid lines) and inward convection due to Ware and Varma pinches (dashed lines).* **D)** *Profiles of D expected in steady state under the assumption that Ware or Varma pinches are the only convective mechanisms.*

ensures the insignificance of edge neutrals, even near the boundary. Fig. 5.15A shows the steady state density profiles in this discharge, as measured by Thomson scattering. The profiles of the Ware pinch, the Varma pinch calculated using the magnetic measurements and the profiles of the effective heat diffusion coefficient χ_{eff} obtained from the power balance

$$\chi_{eff} = \frac{Q_{tot}}{n_e \partial T_e/\partial \rho < |\nabla \rho| >}$$

are shown in Fig. 5.15B. The Varma pinch, is similar to the Ware pinch in magnitude at the plasma edge, but decreases faster towards the centre. A comparison of the convective

fluxes $\Gamma_{Ware} = V_{Ware} \cdot n_e$ and $\Gamma_{Varma} = V_{Varma} \cdot n_e$ with diffusive fluxes $\Gamma_D = -D\nabla n_e$ calculated with different values of D/χ_{eff} assumed are shown in Fig. 5.15C. The sawtooth inversion radius, for this discharge estimated to be at $\rho_{pol} \simeq 0.4$ provides a sufficient width of the confinement zone where the comparison of the fluxes is meaningful. It is seen that for the ratio $D/\chi = 0.5$, the diffusive outward fluxes is significantly higher than Γ_{Ware} or Γ_{Varma} in the confinement zone. The difference by more than order of magnitude at $\rho_{pol} = 0.8$ cannot be explained by uncertainties, related to the neoclassical pinch calculations. A reduction of the ratio D/χ_{eff} down to 0.1 makes the fluxes Γ_D and Γ_{Ware} equal only at $\rho_{pol} \simeq 0.5$ with Γ_D still noticeably higher outside this radial position. To compensate for the observed difference in the fluxes for an admitted value of $D/\chi_{eff} = 1/4$, an anomalous pinch strongly exceeding the neoclassical pinch is therefore needed in the confinement zone.

We can obtain the same conclusion by reversing the argumentation. Assuming the profile of the pinch velocity, one can find the profile of the diffusion coefficient from the $\Gamma_{total} = 0$ condition:

$$D = \frac{V \cdot n_e}{\partial n_e / \partial \rho < |\nabla \rho| >}$$

The profiles of D obtained in this way for the case of the Ware and Varma pinches are shown in Fig. 5.15D. The resulting values of D are very small and would imply that the characteristic times for the evolution of the density profile (n_e or n_D) are 20 times slower that the energy confinement times, which is at odds with experimental observations (see section 5.2.2). The corresponding ratio D/χ has to be as low as 0.025 at $\rho_{pol} = 0.8$, much lower than values obtained for on ASDEX in Ohmic H-mode shots [92,103]. Moreover, the increase of the D profiles toward the centre is also at odds with experimental observations in L-mode plasmas [83–85], which are lowest in the centre and increase towards the edge.

The comparison of the diffusive and neoclassical pinch fluxes over the whole Ohmic database, assuming values of $0.1 \leq D/\chi \leq 0.5$ reveals a systematic difference between these fluxes in the confinement zone similar to one presented in Fig.5.15C. Nevertheless, we cannot exclude the influence of the Ware pinch in the central region of the plasma, where D is lowest.

The comparison of the neoclassical pinch flux with the diffusive flux in Ohmic TCV

plasmas shows that the neoclassical Ware pinch may account for the electron density peaking in the confinement zone only if the corresponding steady state diffusion coefficient is of order of 0.05 m^2/s. However, the combination of such a low D and the Ware pinch is unable to produce the experimental density variations in the plasma current modulation experiments presented in section 5.2.2.

5.4.2   The Ware pinch in ECRH discharges

ECRH heating leads to an increase of the electron temperature and as a result to the decrease of V_{loop}. The additional heating power leads also to the increase of the effective heat conductivity χ_{eff}. Consequently, under the assumption of a proportionality of the particle diffusivity and the heat conductivity, ECRH decreases the ratio V/D and therefore the density peaking.

Assuming the direct connection between heat and particle diffusion we can estimate the particle fluxes corresponding to the particle diffusion and the neoclassical particle convection. Fig. 5.16A represents the experimental density profile in an L-mode discharge with 1.6 MW of off-axis ($\rho_{dep} \simeq 0.6$) ECRH heating. The profiles of Ware and Varma pinches as well as profile of χ_{eff} calculated from power balance with power deposition taken from TORAY-GA are shown in Fig. 5.16B. Compared to the Ohmic discharge in Fig. 5.15, Γ_{Ware} at $\rho_{pol} \simeq 0.8$ is decreased by more than an order of magnitude. As a result, the difference between Γ_D and Γ_{Ware} plotted in Fig. 5.16C becomes even more striking than in the Ohmic discharge.

In order to match the experimental profile in steady state, the diffusion coefficient calculated from the steady state density profile using the Ware or Varma pinches must be extremely low (Fig. 5.16D). To reproduce such D the D/χ_{eff} ratio has to be about order of magnitude lower than the same ratio in Ohmic discharges. The fact that such values of D are far below the values observed in tokamak experiment corroborates the inability of the neoclassical Ware pinch to reproduce the peaking observed in TCV ECRH plasma. Moreover, the strong decrease of the diffusion coefficient from Ohmic to ECRH is inconsistent with the decrease of confinement observed in TCV when ECRH power is applied [104]. Therefore, independently of the assumption on D and χ_{eff} relation,
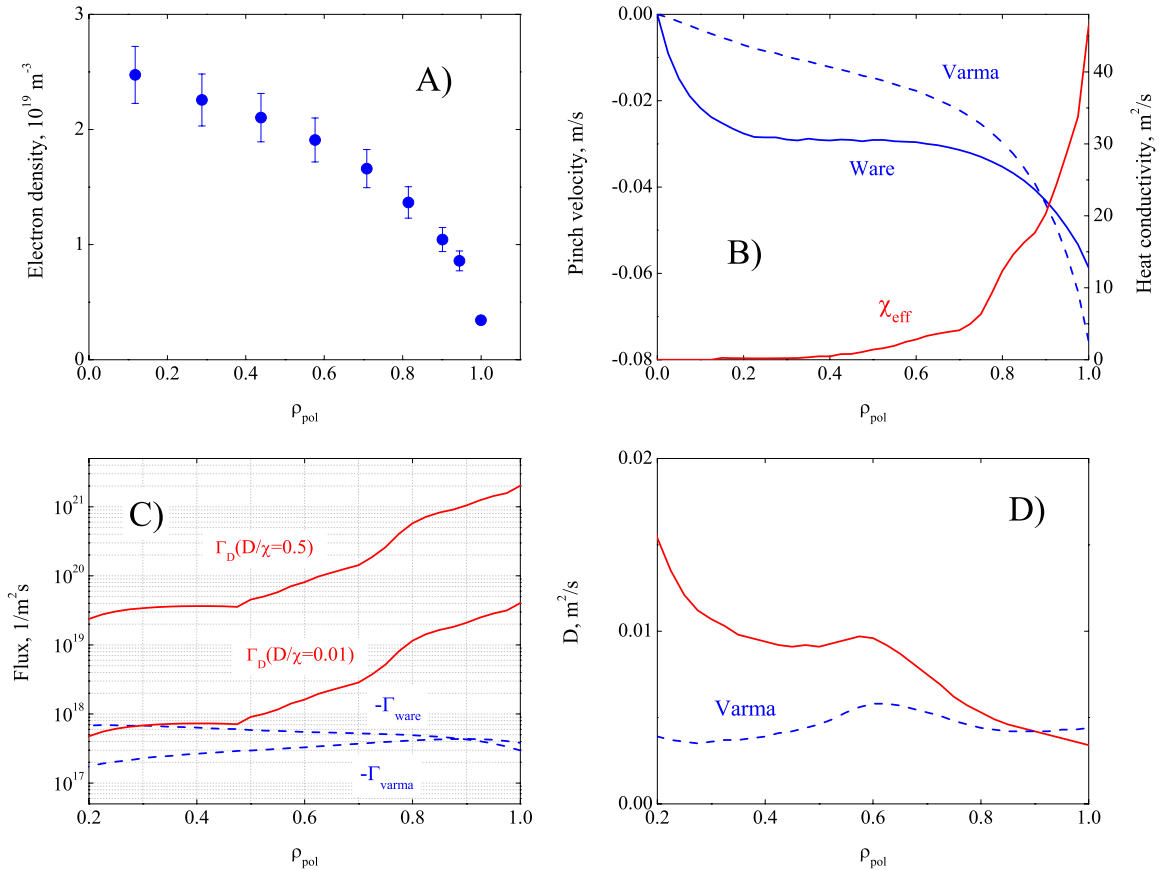
Figure 5.16: **A)** *Experimental density profile in Ohmic L-mode discharge #25410 at 1.9 s (1.6 MW of off-axis heating, $<j>/(j_0 q_0) = 0.26$, $n_{e1}/<n_e>= 1.75$).* **B)** *Radial profiles of Ware and Varma pinches as well as profile of effective heat conductivity.* **C)** *Particle fluxes corresponding to diffusion for different values of D/χ ratio (solid lines) and inward convection due to Ware and Varma pinches (dashed lines).* **D)** *Profiles of D expected in steady state if Ware or Varma pinches are assumed.*

an anomalous pinch mechanism is needed for explaining peaked density profiles in TCV ECRH discharges.

A further unambiguous test of the inapplicability of the Ware pinch in TCV discharges was obtained by investigating discharges with fully sustained current drive. In these discharges, there is no Ohmically driven current and hence there is no parallel electrical field [105].

In discharge #23585 the plasma current has been driven entirely by co-ECCD, in steady state, with 0.9 *MW* of injected power [105]. Time traces of plasma current, total injected ECRH power, current in the Ohmic transformer, loop voltage, and density

peaking are presented on Fig.5.17A. The gyrotrons were aimed at the axis and at $\rho_{pol} \simeq 0.3$ in order to achieve a sawtooth-free, MHD-quiescent discharge.
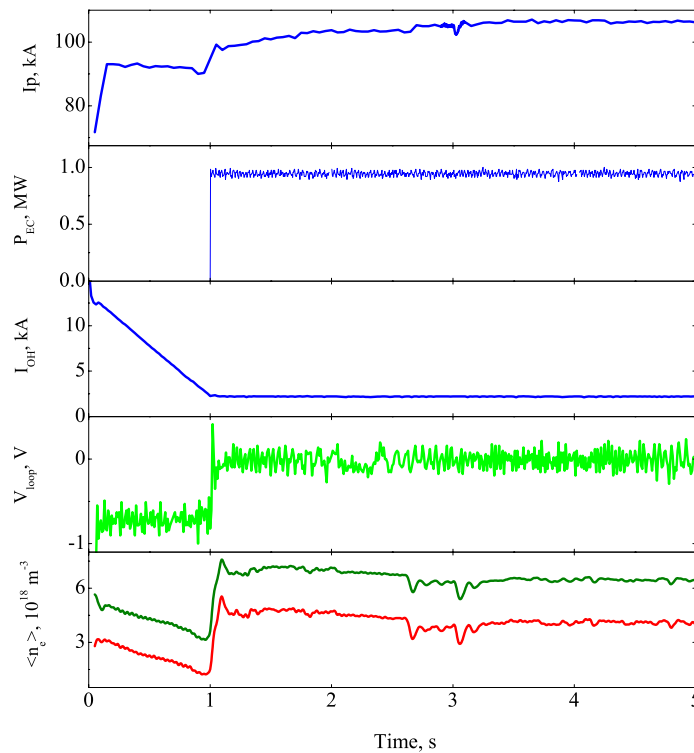

Figure 5.17: *Temporal behaviour of plasma current, ECRH injected power, current in ohmic transformer, loop voltage and line average density from the central and the edge channels of FIR interferometer in the discharge with full electron cyclotron current drive (ECCD) #23585.*

During the phase from 0 to 1 s the current in the Ohmic transformer (I_{oh}) changes, producing an inductive current in the plasma. From 1 s, right after the switch on of 0.9 MW of co-ECCD until the end of the discharge the current in the Ohmic transformer remains constant. A constant current I_{OH} in the Ohmic transformer indicates that all the current in the plasma is driven by ECCD. Accordingly the loop voltage drops from 0.8 V in magnitude in the Ohmic phase to 0, although the accuracy of the measurements of V_{loop} is not better than few mV.

The temporal behaviour of the chord average densities measured by FIR for a chord passing through the centre and one passing through the edge plasma region, are shown on the bottom on Fig. 5.17. No visible difference is observed between the Ohmic phase and the full ECCD phase. The steady state phase lasts about 4 s which significantly exceeds
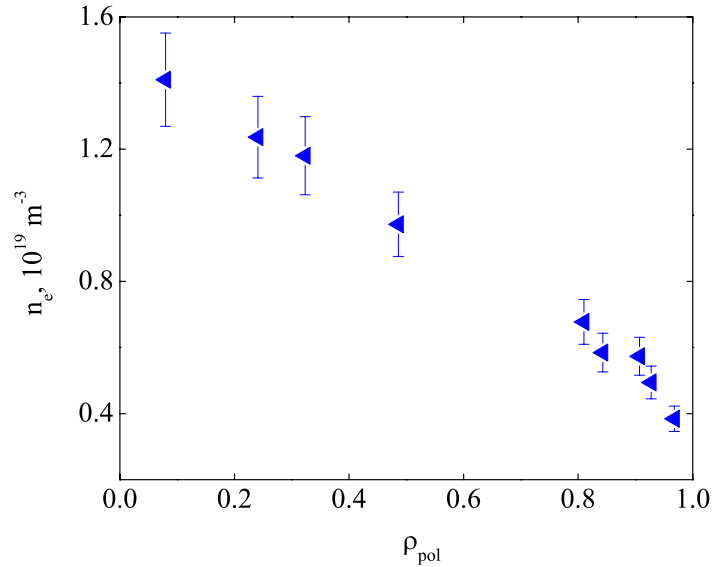
Figure 5.18: *The electron density profile measured by Thomson scattering during ECCD phase (Fig. 5.17, 4.5 s)*

the current resistive diffusion times ($\sim 0.4\ s$). According to the Ware pinch model, the density profile should become completely flat. However, the density profiles remained peaked throughout the discharge i.e. for 10 current redistribution times with $V_{loop} = 0$. Fig. 5.18 shows an example of the profile observed during the fully non inductively driven current phase. Although the parallel electric field is absent during the ECCD phase, the density profile in this discharge does not change appreciably in comparison with a similar ECRH discharge where V_{loop} is about -0.5 V.

A study of several different discharges from the ECRH database, similar to one presented in Fig. 5.16, shows that in medium to high ECRH power discharges, the contribution of the Ware pinch is completely negligible in the confinement zone and is likely to be unimportant in the central region.

5.4.3 Testing the turbulent equipartition

It was shown previously in Ohmic L-mode discharges, that in TCV the total number of the particles within a given flux surface N increases roughly linearly with poloidal flux Ψ i.e. $\partial N / \partial \Psi \approx const$, irrespective of other discharge parameters (see figures 10 and 11 in ref. [91]), suggesting TEP to be responsible for the density peaking. Fig. 5.19A shows

examples of experimental Ohmic density profiles, together with the profiles obtained from TEP predictions using the q profiles given by the equilibrium reconstruction code. In the majority of the analysed Ohmic discharges, the whole density profile in the confinement zone can be fitted by TEP with a single value of η close to 1. The scaling of the density peaking with the parameter $<j>/(j_0q_0)$ predicted by TEP with different values of η is shown in Fig. 5.19B by lines. Agreement with the experiments is reached in TCV Ohmic discharges if $\eta \simeq 1$ suggesting that if TEP is the dominant pinch mechanism, trapped and passing particles should give a similar contribution to the particle transport in all Ohmic TCV discharges. This value of η is somewhat higher than that obtained in L-mode discharges in DIII-D where TEP alone can explain the observed peaking if $\eta \simeq 0.7$ [19,20].

Fig. 5.19C and Fig. 5.19D illustrate that TEP also provides sufficient peaking in the case of ECRH heating. For the density profiles in TCV ECH discharges, a good fit of the scaling can be obtained if η is in the range $0.4 - 1$ as shown in Fig. 5.19D by lines for three values of η. Since, at fixed $<j>/(j_0q_0)$, the density peaking scales with ρ_{dep} it can be suggested that at each fixed ρ_{dep}, it is possible to find a corresponding η, which provides the correct scaling of the profile widths with $<j>/(j_0q_0)$. According to the observations, η has to decrease with ρ_{dep} and these changes of η may in principle be related to the modification of the current profile or shear by ECRH.

Although the agreement between TEP and experiment is remarkably good in the Ohmic case, it is not satisfactory in the case of ECH heating if a single value of η is assumed. It has to be noted that ECRH density peaking predictions in the framework of TEP based on safety factor profiles derived from equilibrium reconstruction LIUQE can serve only as an indication, since no reversal of shear is allowed by LIUQE. For a reliable study of TEP role in ECRH discharges the profiles of plasma current are crucial.

5.4.4 Testing the thermodiffusion

It has already been reported that in Ohmic TCV discharges the temperature profiles are correlated with the current profile [106]. In this case, turbulent thermodiffusion (TTD) can provide an alternative interpretation of the observed density profile scaling. The profile details in L-mode Ohmic discharges and a TTD fit are compared in Fig. 5.20A. The
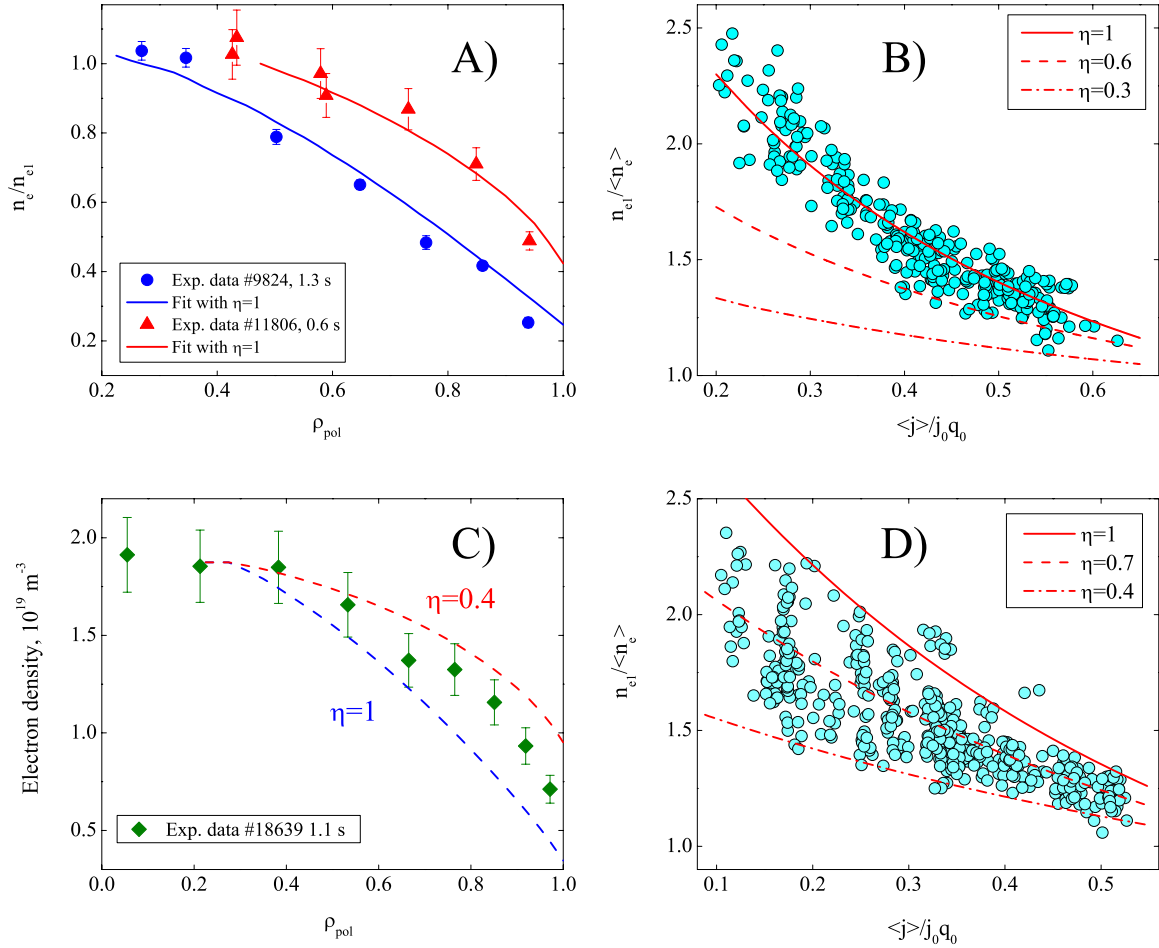
Figure 5.19: **A)** *Experimental density profile for Ohmic L-mode discharges (dots) and profiles predicted by TEP (lines). Profiles are normalized to the density values at the inversion radius.* **B)** *Scaling of electron density peaking widths for Ohmic discharges (dots) and average widths predicted by TEP with different values of η (lines).* **C)** *Experimental density profile in an ECH discharge (dots) and profiles predicted by TEP with two different values of η (lines).* **D)** *Experimental scaling of electron density peaking factor in ECH discharges (symbols) and average widths predicted by TEP with three different values of η*

experimental Ohmic density profile widths and those calculated using TTD are presented in Fig. 5.20B. These examples show that TTD alone provides sufficient peaking for the majority of TCV Ohmic discharges if α is in the range $0.4 - 0.65$, which is in a good agreement with the value $\alpha \simeq 0.5$ found on ASDEX for Ohmically heated discharges [107]. However, the experimental widths decrease with $< j > /(j_0 q_0)$ faster than the widths obtained from TTD with a single, fixed value of α. This means that α must itself be allowed to scale with $< j > /(j_0 q_0)$ in order to reproduce the observations. Such a scaling suggests a relation with the q profile or shear.

In the case of ECH heating, we can roughly separate two classes. The first class corresponds to those discharges where the additional heating does not modify the radial behaviour of the temperature profile. In the second class, two main regions of the temperature profile with different gradients are observed. For the majority of the discharges of the first class, TTD provides a reasonable fit of density profiles with single value of α close to 0.5 (Fig. 5.20C). The experimental density and temperature profiles in the second class of discharges are presented on Fig. 5.20D. For this example, the gradient of the temperature changes significantly at $\rho \simeq 0.6$, however concomitant changes of the density profile are not observed. It is clear that with a single value of α TTD cannot fit the experimental density profile and changes of α at $\rho \simeq 0.6$ are needed. For this particular discharge TTD provides a good description of the density profile if $\alpha \simeq 0.2$ for $\rho < 0.6$ and $\alpha \simeq 0.55$ for $\rho > 0.6$ (Note that TEP provides a good fit to the density profile in Fig. 5.20D for $\eta \simeq 0.8$). Values of α close to 0.5 in the zone of low temperature gradient are found in practically all discharges with changes of the temperature gradient. For some cases α can be as low as 0.1 in the zone with a high temperature gradient. Such extreme cases can be attributed to discharges with an improved central electron confinement (weak eITB). In order to explain the broadening of the density profiles during on-axis heating, α in the central region would have to depend on ρ_{dep}. However, since no dependence of the density peaking on the absolute value of the temperature and on the temperature gradient was found, the form of such a dependence is unclear.

To summarise, we conclude that TCV density profile peaking in the case of Ohmic discharges can be determined by thermodiffusion alone if α itself scales with $< j > / (j_0 q_0)$.
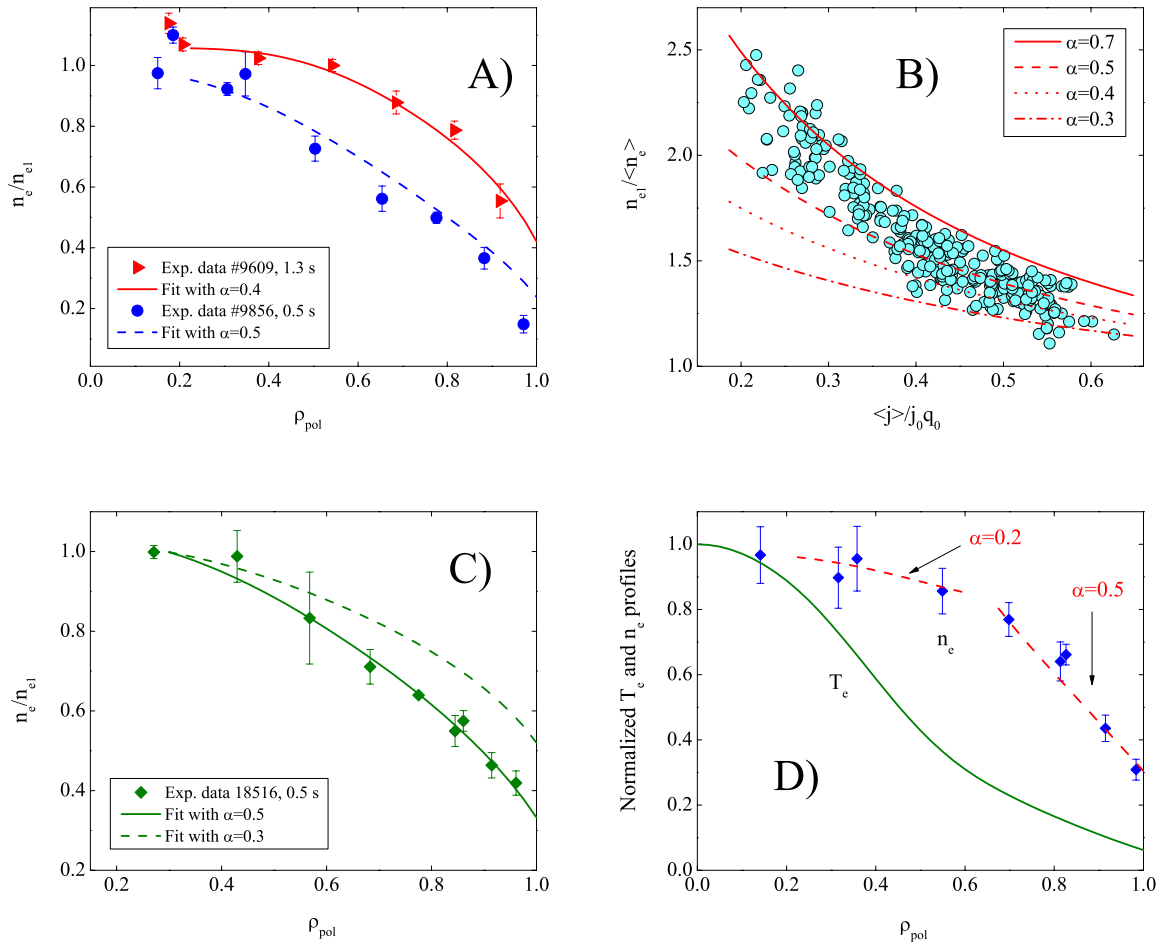
Figure 5.20: **A)** *Experimental density profiles in Ohmic L-mode discharges (dots) com-pared with TTD predictions. Profiles are normalized to the density values at the inversion radius.* **B)** *Experimental scaling of electron density inverse peaking factor for Ohmic L-mode discharges (symbols) and scaling predicted by TTD with four different values of* α. **C)** *Experimental density profile in ECH discharge (dots) and profiles predicted by TTD with different values of* α. *Profiles are normalized to the density values at the in-version radius.* **D)** *Experimental normalized density and temperature profiles in counter ECCD discharge # 15733 at time 1 s. ECH power is 0.9 MW, $< j > /(j_0 q_0) = 0.3$, $< n_e > /n_{e1} = 0.63$, inversion radius $\rho \simeq 0.35$. Dashed line is TTD prediction with $\alpha \simeq 0.2$, dashed line is TTD with $\alpha \simeq 0.5$. Profiles are normalized to the values at the plasma centre.*

In the ECH discharges, TTD provides sufficient peaking for the majority of the cases although changes of α along the radius are needed in order to explain the resilience of density profiles to changes in temperature scale length.

5.5   Mixed interpretations

A natural next step of the present analysis is an attempt to use interpretations based on combinations of different mechanisms. A mixed model should explain the scaling of the density peaking with $< j > / (j_0 q_0)$ in both Ohmic and ECRH discharges and also predict the profile flattening in ECRH discharges.

In Ohmic discharges all three mechanisms Ware, TEP and TTD may in principle contribute to shaping of the density profile. The strong correlation of the current peaking with the peaking of the electron temperature profile makes the separation of the effect of the TEP and TTD very difficult and therefore many linear combinations of TEM, TTD and Ware provide a fit for the Ohmic density profiles. The particular dependence of density peaking on ρ_{dep} during ECRH, together with its independence on V_{loop}, shows that changes of Ware pinch, alone or in combination with constant TEP and TTD, cannot explain the density flattening in ECRH discharges and changes of coefficients for TTD and TEP are needed. At the same time the uncertainties in the choice of particular combinations of TEP and TTD remain when ECRH is applied. One possibility is the coexistence of TEP and inward TTD in Ohmic discharges. In this case the flattening of the density profiles in the presence of ECRH may be attributed to the decrease of TTD inward contribution (decrease of α at fixed η). Another possibility is inspired by the observation of the density flatting in response to strong central electron heating in ASDEX Upgrade [101, 108]. The phenomenon has been attributed to the destabilisation of TEMs, producing an outward thermodiffusive flux ($\alpha < 0$) proportional to the mode growth rate [101]. At the same time, according to [101], the curvature pinch is expected to exist in any experimental plasma conditions for large enough shear. Therefore we can suggest for TCV the existence of pure TEP and Ware in Ohmic discharges and an outward TTD contribution which appears when ECRH is applied and where the electron temperature is increased. The difficulty for both models with inward and outward TTD

is to find the dependence of α on plasma parameters. Experimental observations show no dependence of the density flattening, neither on the value of the central temperatures, $\nabla T_e / T_e$ or on the value of ECRH power applied. Since these parameters are supposed to be connected with the strength of TEM instability, the cause for the changes of α, necessary to characterise the experimental behaviour, is unclear.

5.6 Summary

Electron density profiles in TCV are observed to be peaked. It is also noted in a wide variety of steady-state TCV tokamak discharges, that the electron density profile peaking depends on the current profile peaking via the current profile width parameter $< j > / (j_0 q_0)$, irrespective of the electron density, plasma shape and other parameters. The presence of ECRH heating leads in general to a flattening of the density profile. Slightly steeper profiles than with pure Ohmic heating are observed during far off-axis ECRH. The dependence of the profile widths in Ohmic target plasmas is modified in ECRH discharges by an additional dependence on deposition location, e.g. central heating results in profile broadening. There are exceptions to this behaviour: density pumpout effects and eITBs produce density profiles which clearly depart from the scaling observed in MHD quiescent L-mode ECRH plasmas.

Any single pinch model, which can be considered as a good candidate responsible for TCV electron density profile peaking should not only predict the profile details and peaking scaling with $< j > /(j_0 q_0)$ in Ohmic cases but also explain the scaling of the peaking with ρ_{dep} in ECRH discharges. The conclusion we can make at this point is that none of the three mechanisms presented above can alone predict all of the observed features of TCV density profile behaviour.

The analysis presented indicates that the neoclassical Ware or Varma pinches alone cannot account for the density gradient in the confinement zone in OH plasma. At the same time, the comparison of the neoclassical inward and diffusive outward fluxes in ECRH indicates, that unless the diffusion coefficient is extremely low, the contribution of the Ware pinch to the density peaking during ECRH is insignificant. The density peaking, in full ECCD discharges with $V_{loop} = 0$, unambiguously demonstrates the presence

of an anomalous pinch, in agreement with results obtained in Tore Supra [12]. The role of neoclassical pinches appears to be small however in this study we cannot accurately quantify to which extend they contribute to the total inward convective flux. The regressions suggest its effect on $\nabla n_e / n_e$ to be on average less that 10 % in Ohmic plasmas. A more precise conclusion requires the availability of the experimental profiles of diffusion coefficient.

The density profiles in Ohmic discharges can be fitted by TEP alone if η is about 1. In the case of ECRH heating, TEP matches the experimental profiles well, however a decrease of η is required to follow the flattening of the profiles in response to the changes of the heating location. In Ohmic discharges TTD alone provides sufficient peaking for the majority of the discharges if $0.4 < \alpha < 0.6$, but an additional scaling of α is needed to explain the observed scaling of density widths with the parameter $< j > /(j_0 q_0)$. In ECH discharges, the modification of the temperature gradients by heating, together with the stiffness of the density profiles, leads to the necessity of changes of α with radius. TTD fits the density profiles in the ECH discharges with values of α from 0.1 to 0.5 depending on the temperature profiles.

It is reasonable to hypothesize that all three presented mechanisms are present in Ohmic discharges and that TEP and TTD play a role in ECRH discharges. However, more detailed information about the diffusion coefficient in both ECRH and Ohmic regimes and plasma current profile during ECRH would be needed in order to asses their relative role.

Chapter 6

Electron density profile behaviour in JET

6.1 Introduction

A substantial database modelling analysis of density peaking in Ohmic and ECH plasmas in TCV, which was based mainly on Ohmically relaxed, sawtooth discharges, did not allow us to determine whether TEP or anomalous thermodiffusion was the major contributor, because in these discharges the overall shear (or current profile peaking) remained correlated with the degree of peaking of the electron temperature profile, as well as with the sawtooth inversion radius, all of which scale with the current profile peaking parameter $< j > /(j_0 q_0)$. We therefore investigated a series of sawtooth-free lower hybrid current driven (LHCD) JET L-mode discharges, which produced a range of current profiles for a fixed value of $< j > /(j_0 q_0)$. These profiles are very different from those accessible in sawtoothing regimes, and span the range from normal shear to substantially reversed shear. They allow us to test whether the peaking of the density profile follows the peaking of the current profile, as expected for TEP, or whether it follows the electron temperature profile, as expected for anomalous thermodiffusion.

Despite of the physical significance of the results obtained in the L-mode regime, it is not possible to directly extrapolate the findings to reactor plasmas, since ITER is expected to operate in H-mode [109]. The recent discovery in ASDEX Upgrade [26] of a collisionality dependence of the density peaking in H-mode discharges therefore also stimulated a study of parametric dependencies of density peaking in JET H-mode discharges.

The data from L- and H-modes were used to assemble a profile database of about 160 timeslices for L-mode and about 300 timeslices for H-mode taken in quasi-stationary conditions. Density profiles were evaluated from the JET multichannel far infrared interferometer with the SVD-I and LBF-I methods (see chapter 2). The agreement within 10% of $n_e(0)/ < n_e >$ from the two methods provides an estimate of the reconstructional errors.

6.2 Experimental observation of density peaking in L-mode

The data for this study were obtained from a series of LHCD L-mode discharges in JET, with LHCD powers in the range 0 (Ohmic) to 3.65 MW, part of which were produced to demonstrate the safety factor profile control using the JET real-time control system [47]. Full current drive with $V_{loop} \approx 0$ was obtained at the highest powers available, as shown in the example of Fig. 6.1, for otherwise similar discharges with $q_{95} \cong 8$, $0.8 \cdot 10^{19}$ $m^{-3} \leq n_e \leq 1.4 \cdot 10^{19}$ m^{-3} and central electron temperatures in the range $1.7 \leq T_e(0) \leq 6.3$ keV, depending on LH power. In these plasmas electrons and ions are poorly coupled. The central ion-to electron temperature ratio, $T_i(0)/T_e(0)$, obtained from charge exchange spectroscopy using sporadic brief neutral beam pulses, dropped from 0.5 under Ohmic conditions, to 0.2 with full power LHCD. LHCD drives an off-axis current, thereby broadening the current profile and, for sufficient power, producing a hollow current profile [47]. This range of LH powers allowed the creation of a variety of magnetic shear profiles, ranging from normal at low power to strongly reversed at the highest power levels. Examples of the corresponding safety factor profiles are shown in Fig. 6.2 and were obtained by EFIT equilibrium reconstructions, which used Faraday rotation data from the JET interfero-polarimeter as a constraint [51].

Despite having reversed shear profiles, these plasmas did not produce internal transport barriers, presumably because of the lack of centrally deposited auxiliary power. Electron temperature and density profiles from LIDAR Thomson scattering (LTS), normalized to the central values, are shown in Fig. 6.3 and appear to be little or not affected by the
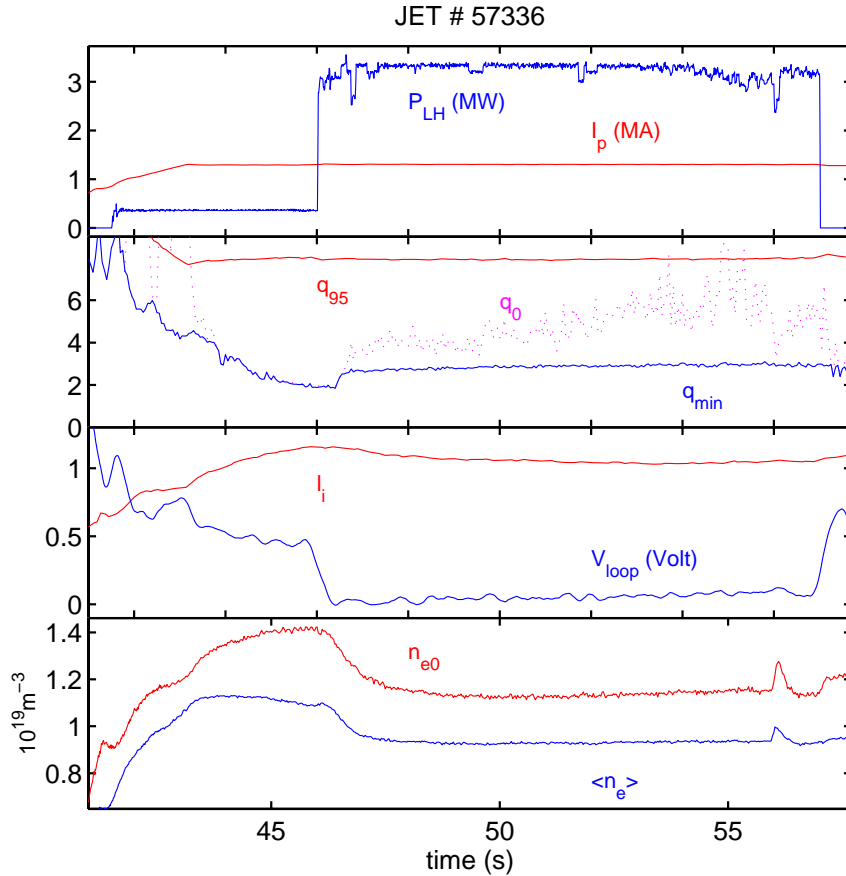
Figure 6.1: *Evolution of a JET LHCD discharge with $V_{l}oop \cong 0$. Top pane: time dependence of plasma current and LHCD power. Second pane: q_{95}, axial safety factor and minimum of safety factor profile from polarimetry. Third pane: Internal inductance and toroidal loop voltage. Bottom pane: Axial and average electron densities from interferometry.*

differences in shear. The profiles shown are averaged over 1 s in stationary conditions in order to improve the rather poor signal-to-noise ratio of the LTS diagnostic at these low densities, for which uncertainties in the individual data points are of the order of 20%.

The fact that the density profiles remain peaked for $V_{loop} \cong 0$ shows that a pinch mechanism other than the Ware pinch must be responsible.

Fig. 6.4 shows, that for constant $< j > /(j_0 q_0)$, density peaking depends on overall shear, expressed as $< j > /j_0$, in normal shear plasmas defined by $q_{min} = q_0$. This relationship can be expressed approximately as

$$\frac{n_{e0}}{< n_e >} \sim \frac{1}{0.88 \cdot < j > /j_0 + 0.29} \qquad (6.1)$$
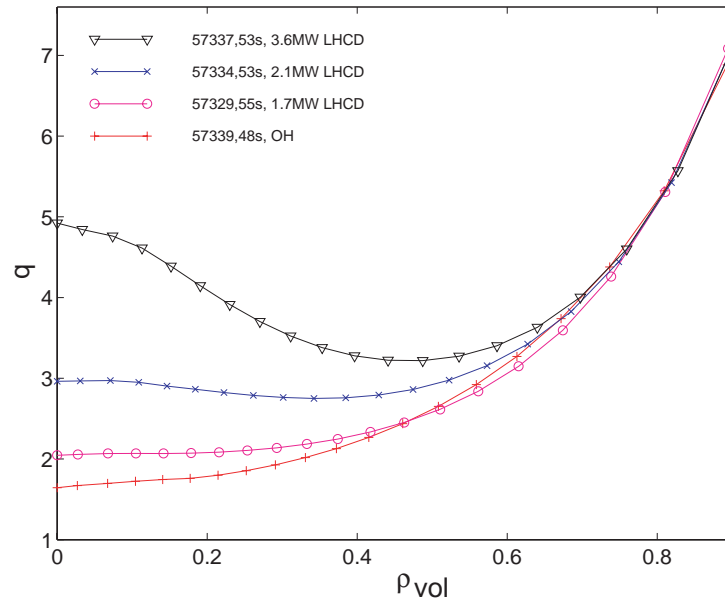
Figure 6.2: *Safety factor profiles from interfero-polarimetry, obtained with different levels of LHCD.*
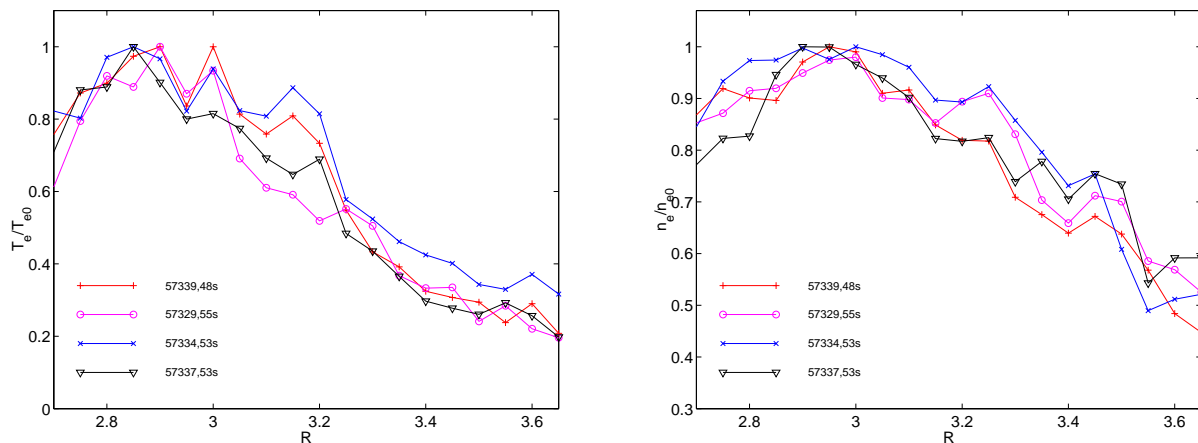
Figure 6.3: *Electron temperature (left) and electron density (right) profiles from LIDAR Thomson scattering corresponding to times in Fig. 6.2, averaged over 0.8 s. Errors bars on individual measurements are some 20%. The magnetic axis is at $R \cong 2.95$ m.*

The symbol types in the figure refer to electron temperature peaking $T_{e0}/ < T_e >$ from LIDAR TS, showing, that within the range of variation of this parameter, no dependence is discernible in the dataset.

It is interesting to note that the values of the peaking observed in JET L-mode normal shear discharges as well as its dependence on $< j > /j_0$ is very close to the values and

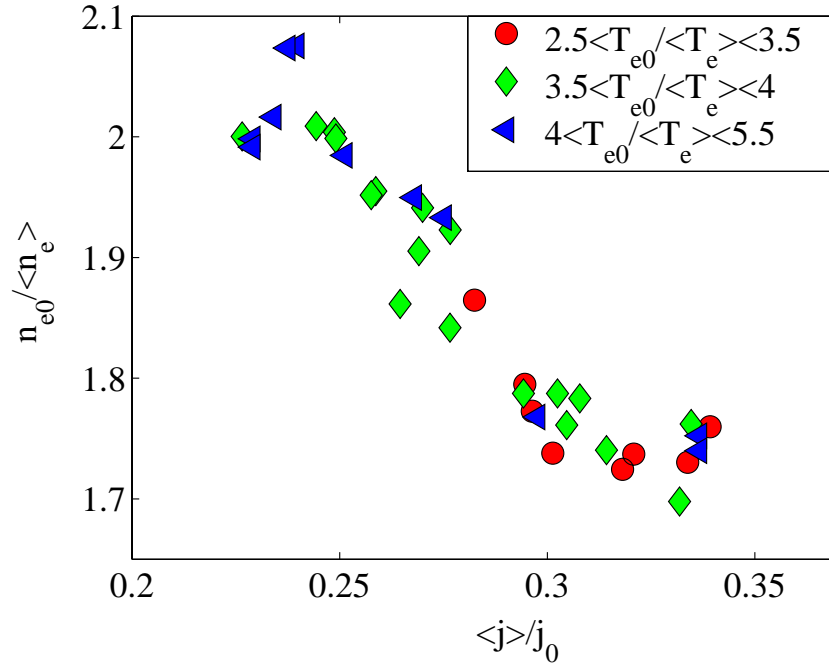Figure 6.4: *Dependence of density peaking on the peaking of the current profile at constant q_{95} in normal shear discharges. Symbols refer to classes of electron temperature profile peaking parameter.*

peaking behaviour observed in TCV sawtoothing L-mode discharges (see Fig. 5.4), for which the parameter $<j>/(j_0 q_0)$ is practically identical to $<j>/j_0$ ($q \simeq 1$).

When reversed shear discharges are included in the analysis, $<j>/j_0$ ceases to be a suitable scaling parameter (Fig. 6.5) as already expected from the observation that the central portions of the density profiles are insensitive to shear reversal (Fig. 6.3 right). The various symbols in Fig. 6.5 refer to classes of the reversal parameter q_{min}/q_0, as determined using the real-time polarimeter inversion routines of the JET real-time control system [57]. The best data alignment is obtained with the internal inductance, l_i (Eq. 5.2), which can be determined independently of the equilibrium reconstruction. As a filter for data quality, the present dataset was restricted to reconstructions that yielded values for l_i, which, up to a systematic deviation (0.1), were consistent with the evaluation based only on the corresponding Shafranov integral. In order to conserve consistency with the TCV data presented in chapter 5, we have plotted $n_{e0}/<n_e>$ versus $1/l_i$ in figure
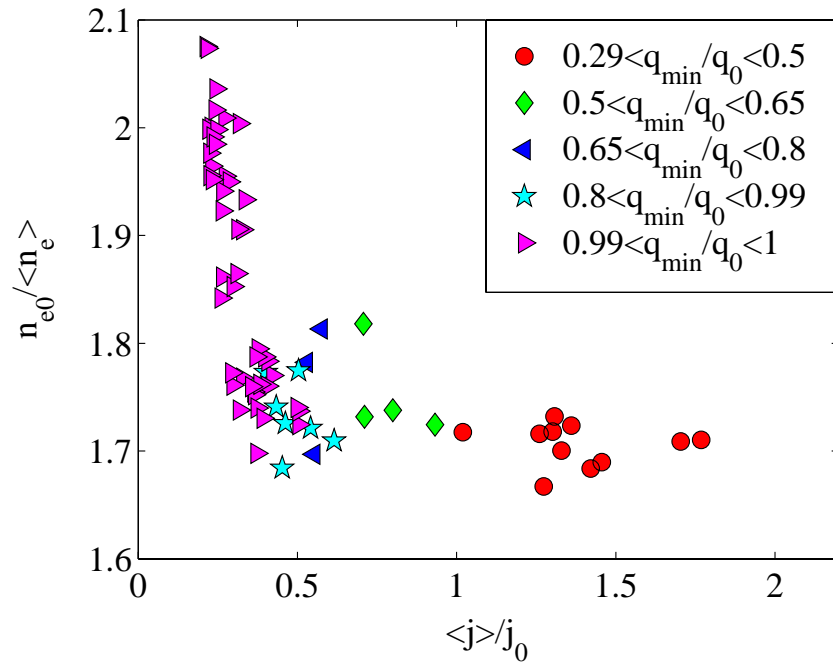
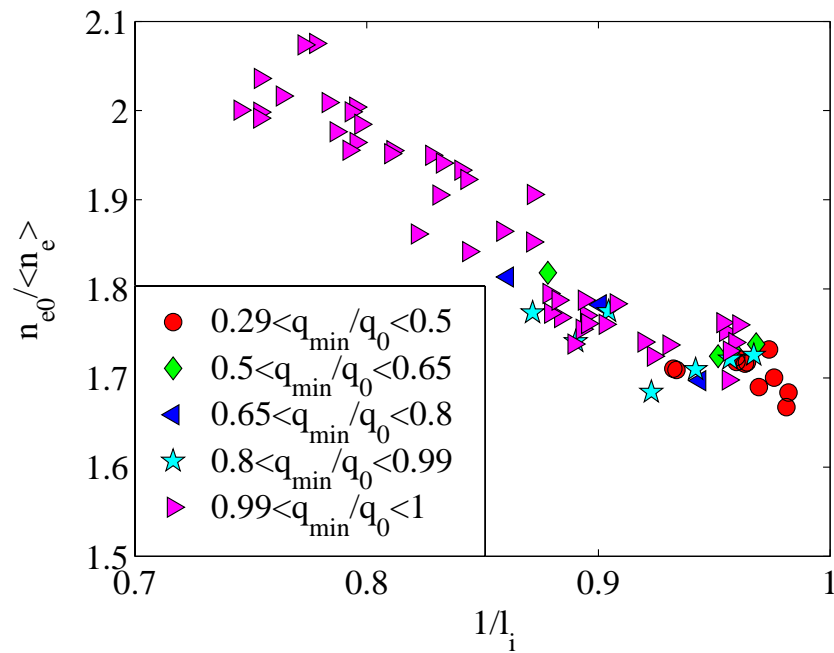Figure 6.5: *Electron density peaking versus current density peaking (normal and reversed shear).*

Figure 6.6: *Dependence of density peaking on internal inductance. Symbols refer to reversal parameter.*

Fig. 6.6. We are not aware of any *a priori* theoretical reason for the good correlation

$$\frac{n_{e0}}{< n_e >} = 1.18 \cdot l_i + 0.48$$

with this particular measure of current profile peakedness. (It should also be noted that the proportionality factor is expected to depend on plasma shape.)

Since the SVD-I may, in principle, be prone to systematic errors, we cross checked the l_i dependence using a qualitative but sensitive measure of peaking based on the ratio of the directly measured line average densities from a central and an off-axis interferometer chord. This is only applicable for a dataset with the same plasma geometry, as is the case here. Both chords are nearly horizontal, making them also insensitive to possible changes in core geometry caused by small differences in the Shafranov shift. The result in Fig. 6.7 shows that the chord ratio follows $1/l_i$ in the same way as the peaking factor derived from the SVD-I. This figure is also resolved into classes of line average electron density, showing that the absolute density, which determines the depth of neutral penetration, has no effect on the peakedness of the density profile.
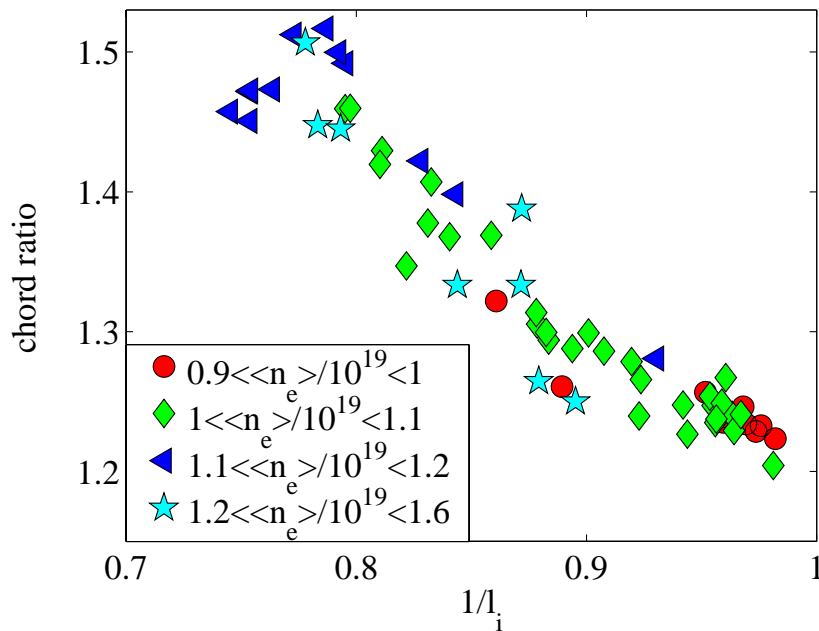

Figure 6.7: *Ratio of chord #8 (on-axis) and chord #5 (off-axis) line density measurements versus $1/l_i$. Symbols refer to the classes of line average densities measured by the central FIR chord.*

In Fig. 6.8 we have plotted $n_{e0}/ < n_e >$ as a function of a qualitative indicator of

temperature peaking determined from electron cyclotron emission, confirming that there is no correlation with temperature peaking. This indicator was chosen as the normalized temperature difference between the core and a point at 60% of the minor radius. ECE signals beyond some 65% of the minor radius were overwhelmed by downshifted radiation from LHCD generated suprathermal electrons. The symbols in Fig. 6.8 are for classes of l_i, showing that there is no correlation between l_i and $< T_e > /T_{e0}$, which would allow the results to be interpreted either by TEP or by thermodiffusion. The possibility of a visually unnoticed secondary dependence of density peaking on temperature peaking has been assessed using a three-parameter regression of the form

$$\frac{n_{e0}}{< n_e >} = c_l l_i + c_T \frac{\Delta T_e}{< T_e >} + c_0 \tag{6.2}$$

where $\Delta T_e/ < T_e >$ was evaluated between $r = 0$ and $r = 0.6$ a as in Fig. 6.8. The standard deviation σ of the fit is unchanged when $\Delta T_e/ < T_e >$ is included in the fit (compare regressions #1 and #2 in Table 6.1), confirming the irrelevance of temperature peaking. The three parameter regression with T_e/T_i (T_e from LIDAR and T_i from CXS) evaluated at $r/a = 0.5$ as a second parameter was performed on a reduced dataset for which T_i measurements are available. An addition of T_e/T_i to the leading l_i dependence decreases very slightly the standard deviation however, the error on the coefficient c_{T_e/T_i} is significantly higher than coefficient itself. This uncertainty, probably related to small number of data points for T_i (19 in total), makes the dependence on T_e/T_i questionable.

In Figs. 6.9, 6.10 and 6.11 the dependencies of the density peaking on the LHCD power P_{LHCD}, the loop voltage V_{loop} and on effective collisionality for drift wave instabilities ν_{eff} (see for definition Eq. 3.10) are shown by the classes of symbols. Two parameter regressions with parameter $\tau_e V_{loop}/I_p$ (see Eq. 5.3), P_{LHCD}, ρ^* or ν_{eff} as a main parameters give much higher standard deviations than ones obtained when l_i is taken as main parameter. It appears that in three parameter regressions with P_{LHCD} or $\tau_e V_{loop}/I_p$ taken in addition to l_i, the standard deviation is slightly decreased (columns #3 and #4 in Table 6.1). The negative coefficient $c_{P_{LHCD}}$ shows a weak effect of profile broadening with increase of LHCD power. The secondary (to l_i) effect of the Ware pinch appears in a slight peaking of the density profile as Ware pinch increases. We should note, that since the $c_{P_{LHCD}}$ and c_{Ware} are small in comparison with c_{l_i}, with errors of the order of the

	1	2	3	4	5	6	7	8
c_0	0.48 ±0.09	0.45 ±0.1	0.66 ±0.12	0.79 ±0.19	0.53 ±0.1	0.48 ±0.09	0.52 ±0.15	0.47 ±0.1
l_i	1.18 ±0.08	1.17 ±0.08	1.0 ±0.11	0.94 ±0.15	1.12 ±0.09	1.12 ±0.09	1.16 ±0.09	1.19 ±0.1
$\Delta T_e / <T_e>$		0.04 ±0.06						
$10^7 \tau_e |V_{loop}|/I_p$			0.08 ±0.04					
$P_{LHCD}/10^6$				−0.02 ±0.01				
ν_{eff}					0.04 ±0.04			
$<n_e>/10^{20}$						0.04 ±0.04		
$10^3 \cdot \rho^*$							−0.01 ±0.02	
q_{min}/q_0								−0.01 ±0.03
$\sigma \cdot 100$	3.6	3.59	3.33	3.39	3.5	3.5	3.6	3.6

Table 6.1: *Results of linear regressions for $n_{e0}/<n_e>$. Intervals are given for the 90% confidence level. Dataset size is 71 samples.*

coefficients itself, the effect of the LHCD power or the Ware pinch on the density peaking borders on statistical insignificance. In addition to the leading l_i dependence, ν_{eff} or $<n_e>$ (regressions #5 and #6) produce a small reduction of the standard deviation, however uncertainties in the coefficients do not allow to affirm the importance of these parameters.

The normalized Larmor radius

$$\rho^* = \frac{v_{\perp e}}{a\omega_{ce}} \tag{6.3}$$

where a is a minor radius, $v_{\perp e}$ is the perpendicular component of electron thermal velocity and ω_{ce} is the electron cyclotron frequency, evaluated at mid-radius, ranges in the presented LHCD discharges from $2 \cdot 10^{-3}$ to $3.25 \cdot 10^{-3}$. The regression #7 in Table 6.1 shows that once the dependence on l_i is acknowledged, the influence of ρ^* on density peaking is not statistically meaningful. The same conclusion holds for reversal factor q_{min}/q_0
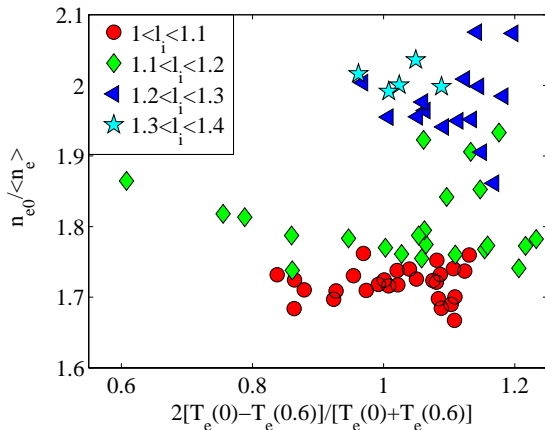
Figure 6.8: *Density peaking versus average electron temperature gradient from ECE in the plasma core region. Symbols refer to classes of internal inductance.*
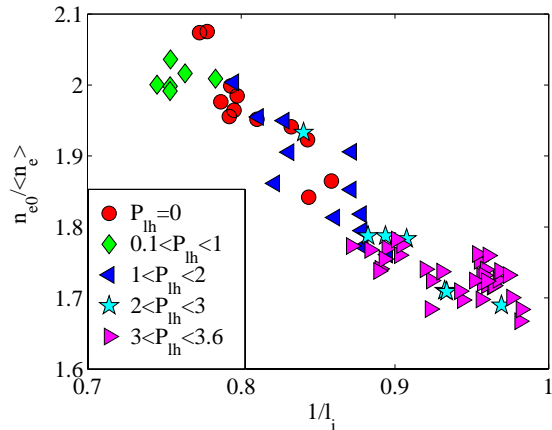
Figure 6.9: *Dependence of density peaking on internal inductance, resolved into classes of LHCD power*
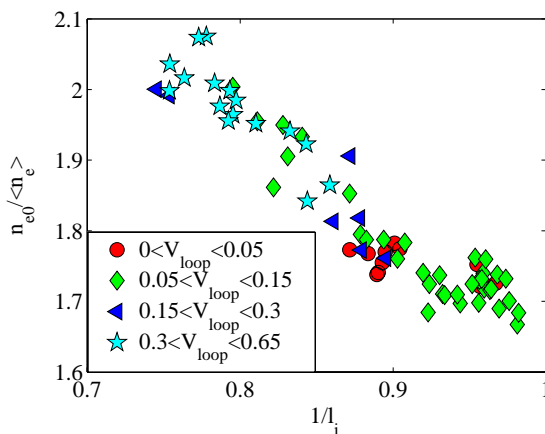
Figure 6.10: *Dependence of density peaking on internal inductance, resolved into classes of loop voltage*
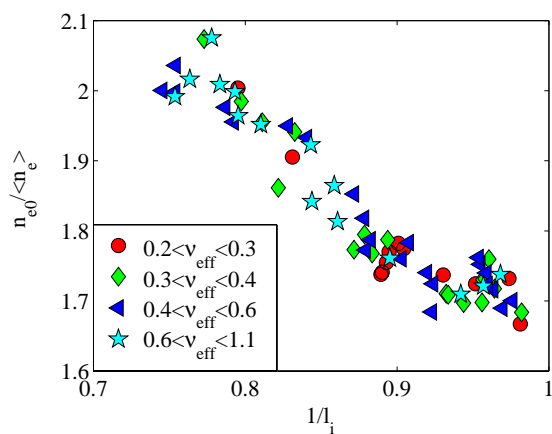
Figure 6.11: *Dependence of density peaking on internal inductance, resolved into classes of effective collisionality ν_{eff} at $r/a = 0.6$. The electron collisionality ν^* ranged from 0.04 to 0.3.*

(regression #8).

6.2.1   Comparison with TEP predictions

Since the peaking subsists at zero loop voltage and is insensitive to the electron temperature peaking, neither the Ware pinch, nor thermodiffusion are considered here. We

modelled the density profiles semi-empirically by assuming a pinch velocity

$$V = -\eta D \frac{\nabla q}{q} \tag{6.4}$$

The modelled peaking is in good agreement for normal shear discharges if $\eta \simeq 0.75$ as it is shown in Fig. 6.12. This value η is close to the average η in TCV ECRH discharges (see section 5.4.3) and to η obtained in DIII-D L-modes [19, 20].
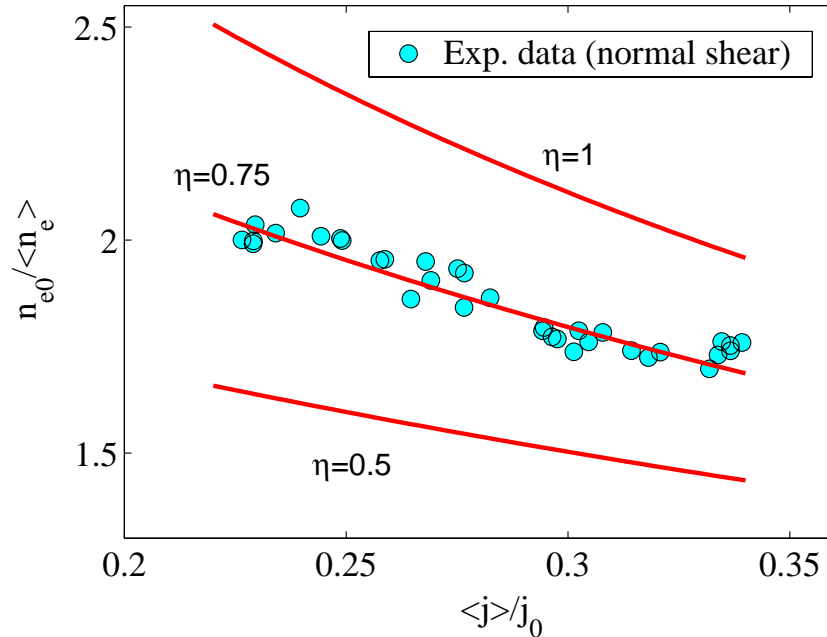
Figure 6.12: *Dependence of density peaking on the peaking of the current profile at constant* q_{95} *in normal shear discharges (dots) together with the peaking predicted by TEP with three different values of* η *(lines).*

TEP with $\eta \sim 0.75$ describes well also the normal shear region in the discharges with reversed shear. However, Eq. 6.4 fails to describe the profiles in reversed shear region, for which it predicts hollow density profiles, which are clearly outside the error bars of the SVD-I inversion. Therefore we tested the expression for TEP proposed by Isichenko et al [18]

$$\frac{n_e(r)}{n_e(0)} \approx \left\{ 1 - \frac{4}{3R_0} \int\limits_0^r \left(\frac{d \ln q}{d \ln r} + \frac{3}{8} \right) dr' \right\} \tag{6.5}$$

The model profiles were evaluated by replacing r with the volume coordinate $a\sqrt{Vol/Vol_{tot}}$, where a is the minor radius, and using safety factor profiles from polarimeter constrained equilibrium reconstructions.
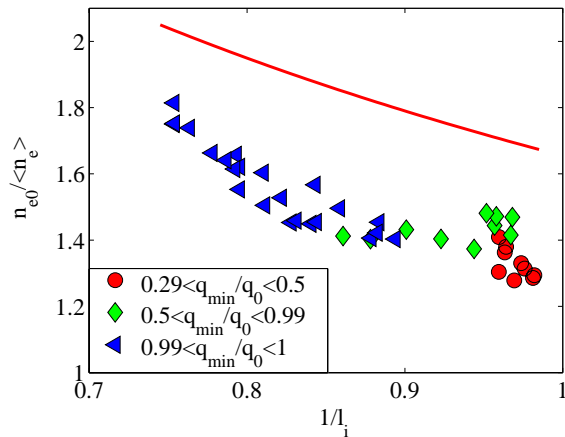
Figure 6.13: *Examples of density peaking from Eq. 6.5 (dots). The average experimental peaking is indicated by the line.*
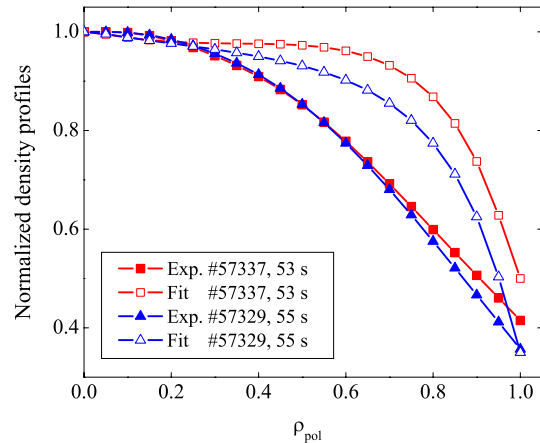
Figure 6.14: *Examples of density peaking from Eq. 6.5 (open symbols), modelled using the safety factor profiles in Fig. 6.2. In the discharge #57337 the shear is strongly reversed and the discharge #57329 has low normal shear. Normalized experimental profiles of the density are shown by coloured symbols.*

The density peaking, obtained from Eq. 6.5, follows a dependence on l_i, decreasing with l_i as it is shown in Fig. 6.13 by dots. However the values of the predicted peaking are clearly lower than the experimental peaking, the average of which is plotted in the same figure by a continuous line. Fig. 6.14 shows examples of model profiles for reversed and normal shear discharges produced using the above expression and the safety factor profiles shown in Fig. 6.2. Eq. 6.5, does not produce hollow profiles, even in the cases with the strongest shear reversal (see #57337 in Fig. 6.14), however, the predicted density profiles are significantly flatter than experimental ones in a considerable part of the discharge.

Although there is good agreement with TEP/curvature pinch predictions (in the form Eq. 6.4) in positive shear regions, we must be aware that this should not necessarily be expected at low or negative shear. Anomalous pinches only exist as a result of microturbulence such as in TEM and ITG modes. If these modes are suppressed or stabilized, as may be the case in regions with low or negative shear and with low core heating as with off-axis LHCD, the corresponding pinches would be absent too. In the discharges described here, this would still leave the weak neoclassical pinches, other than the Ware

pinch, such as neoclassical thermodiffusion, for which $V_{Te,neo} = D_{neo}\nabla T_e/(2Te)$ in axisymmetrical geometry [27]. In the absence of any other convective mechanism and anomalous diffusion, this pinch tends to produce density profiles such that $\nabla n_e/n_e = \nabla T_e/(2T_e)$. To test this hypothesis it would be necessary to confirm experimentally, or at least theoretically, that the low or reversed shear core region is turbulence-free, an undertaking which is beyond the scope of this thesis.

6.3 JET H-mode

The data presented here contain a great variety of stationary (for several current redistribution times) discharge conditions with $0.97 \leq B_T \leq 3.5$ T, $0.95 < Ip < 3$ MA, $1.7 \cdot 10^{19} \leq n_e > \leq 11 \cdot 10^{19}$ m^{-3}, $2.3 \leq q_{95} \leq 6.5$, $4 \leq R/L_{T_e}(0.5) \leq 9$, $0.6 \leq T_e(0.5)/T_i(0.5) \leq 1.7$, $0.04 \leq V_{loop} \leq 0.55$ V, $3 \cdot 10^{-3} \leq \rho^* \leq 9 \cdot 10^{-3}$ and combinations of heating methods with $P_{nbi} \leq 17MW$ (co-injected), $P_{icrh} \leq 10$ MW, $P_{lhcd} \leq 3$ MW, including a minority of cases with substantial RF heating (P_{icrh}/P_{tot} in the range $0.4 - 0.9$ and near central deposition). The normalized toroidal beta

$$\beta_N = \beta_t \frac{aB_T}{I_p}$$

where β_t is the ratio of plasma pressure to toroidal magnetic field B_T and I_p is the total plasma current varies in dataset by more than factor of 3 from 0.7 to 2.6. Both type I and type II ELMs are represented, no ELM-free discharge phases or ITBs are included. The data were not screened to exclude neoclassical tearing modes [110, 111], which may be expected at the upper end of the range of β_N in the dataset.

The collisionality dependence of the density peaking factors for a large representative set of stationary ELMy JET H modes and hybrid scenario H-modes (which have moderate to high q_{95} and low core magnetic shear) is shown in Fig. 6.15. The effective collisionalities obtained on JET extend into the range expected for the ITER reference H-mode, $\nu_{eff} < 0.1$ at $r/a = 0.5$, depending on assumptions and transport models [112, 113].

The different symbols in Fig. 6.15 refer to classes of internal inductance, which is a robust measure of overall magnetic shear. The same data are plotted versus l_i in Fig. 6.16. There is no discernible dependence on l_i, except for $\nu_{eff} < 0.25$. This observation was
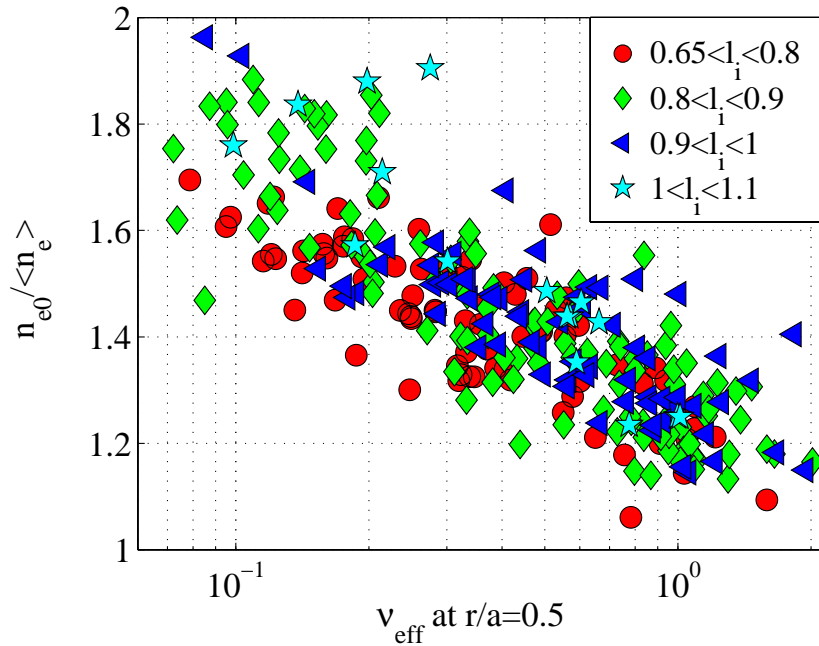
Figure 6.15: *Density peaking factor in H-mode versus ν_{eff} at $r/a = 0.5$. Symbols refer to the classes of internal inductance l_i.*

confirmed by linear two and three parameter regressions. As it is seen from columns #1 and #2 of Table 6.2, in the region $\nu_{eff} < 0.25$ the influence of l_i and ν_{eff} on the density peaking is of equal importance and the linear combination of internal inductance and logarithm of effective collisionality with the coefficients presented in column #3 provides the best fit of experimental data in the region of low ν_{eff}.

For the discharges with $\nu_{eff} > 0.25$, $log(\nu_{eff})$ becomes the main scaling parameter and the influence of l_i on the density profile is decreased (see regressions #3, #4 and #5). This behaviour of the density peaking is in contrast to L-modes in DIIID [20], TCV (see chapter 5) and JET (section 6.2), where magnetic shear (or the peakedness of the current profile) was found to be the most important parameter, irrespective of collisionality.

It seems reasonable to assume that the differences between density behaviour in L- and H-mode are somehow linked to the nature of the underlying turbulence (ITG or TEM). The fundamental difference between L and H-modes is the edge pedestal, which appears to lead to flatter core density profiles, which is stabilising TEMs and de-stabilising for ITGs. At $\nu_{eff} < 0.25$, however, the significant density gradient in H-mode would reduce ITG growth rates and contribute to destabilising TEMs, which may explain why a shear
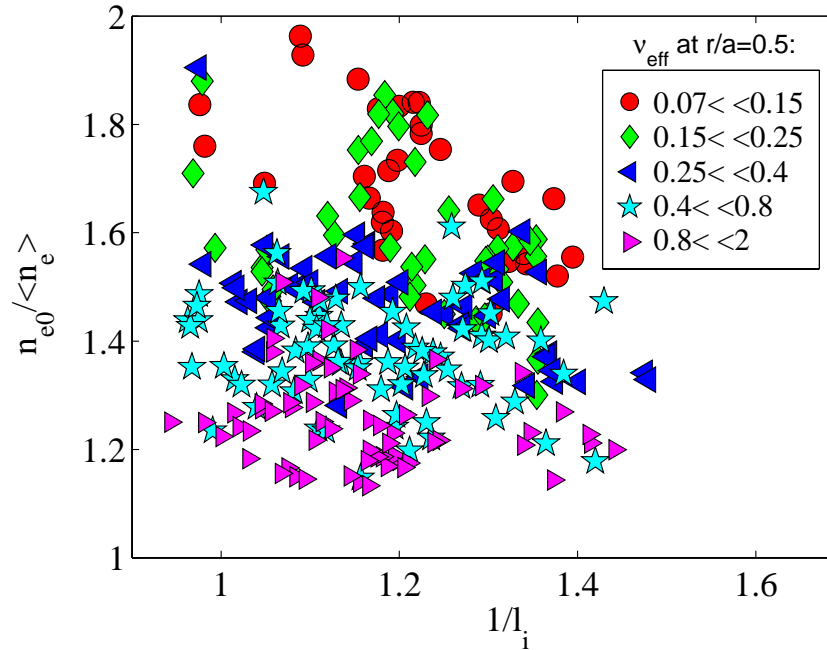
Figure 6.16: *Peaking factor in H-mode versus $1/l_i$ resolved by classes of effective collisionality ν_{eff}.*

dependence similar to that of L-modes is observed.

	1 $\nu_{eff} < 0.25$	2 $\nu_{eff} < 0.25$	3 $\nu_{eff} < 0.25$	4 $\nu_{eff} > 0.25$	5 $\nu_{eff} > 0.25$	6 $\nu_{eff} > 0.25$
c_0	1.1 ± 0.24	1.26 ± 0.1	0.62 ± 0.3	1.36 ± 0.17	1.27 ± 0.01	0.96 ± 0.1
l_i	0.63 ± 0.29		0.78 ± 0.3	0.2 ± 0.2		0.35 ± 0.12
$\log(\nu_{eff})$		-0.19 ± 0.08	-0.19 ± 0.07		-0.18 ± 0.02	-0.18 ± 0.02
$\sigma \cdot 10$	1.3	1.29	1.14	1.27	0.91	0.87

Table 6.2: *Results of linear regressions. The regressions $\#1 - \#3$ are performed on the subset of the data for which $\nu_{eff} < 0.25$ and regressions $\#4 - \#6$ corresponds to the subset with $\nu_{eff} > 0.25$. Intervals are given for the 90% confidence level. Dataset contains 240 samples.*

The dependence of the density peaking on the logarithm of the effective collisionality found in JET H-mode is very similar to the dependence previously discovered on ASDEX Upgrade [26]. A side-by-side comparison of JET and ASDEX Upgrade results is presented
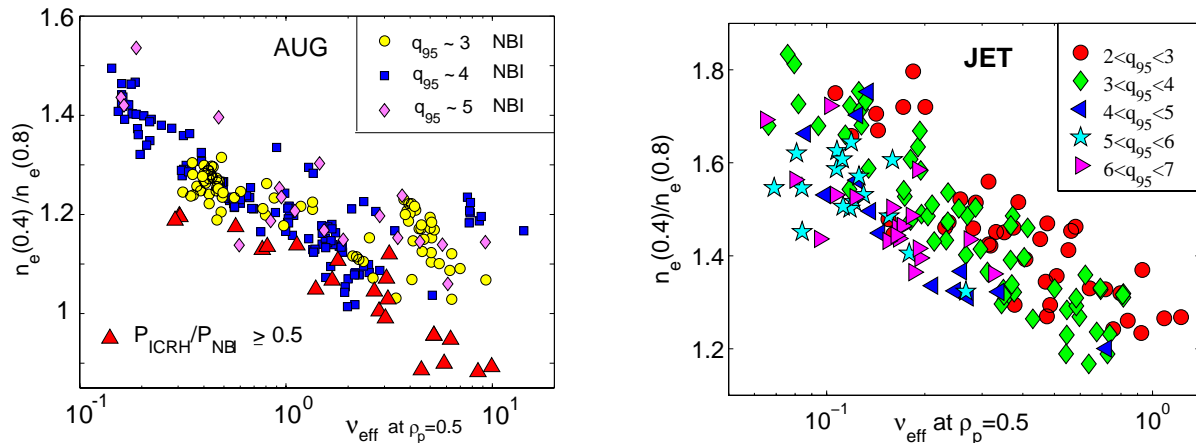
Figure 6.17: *Density peaking expressed as a ratio of electron density at $\rho_{pol} = 0.4$ and $\rho_{pol} = 0.8$ versus n_{eff} in ASDEX-Upgrade in H-mode discharges [26] (left) and in JET in H-mode discharges (right).*

in Fig. 6.17. To keep the same appearance as in [26] we expressed the JET density peaking as a ratio of electron density at $\rho_{pol} = 0.4$ and at $\rho_{pol} = 0.8$. The small difference in this ratio in ASDEX Upgrade and in JET for the same ν_{eff} may be due to the uncertainties in values of Z_{eff} which enter in the definition of ν_{eff}. Therefore we can conclude that the results from the two devices agree within the errors of the measurements. Unfortunately, the data from ASDEX Upgrade does not cover the $\nu_{eff} < 0.15$ region and we cannot compare the current profile peaking dependence appearing in JET at the lowest ν_{eff}.

We found no direct dependence of peaking on β_N, ρ^*, $< n_e >$, V_{loop}, P_{icrh}/P_{tot}, T_e/T_i, L_{T_e}, L_{T_i}, nor on ELM frequency and amplitude despite the correlation of some of these parameters with ν_{eff} in the operational domain. For any value of ν_{eff}, V_{loop} has a wide range of variation, which is uncorrelated with peaking. L_{T_e}, L_{T_i}, T_e/T_i and ρ^* evaluated at $r/a = 0.5$, q_{95}, and β_N are not or only weakly correlated with ν_{eff}. ρ^* and β_N are strongly collinear, but neither of the two appears to have a direct influence on the density profiles. The lack of a dependence on $< n_e >$ and the fraction of RF heating P_{icrh}/P_{tot}, which govern respectively the penetration of beam neutrals and of edge neutrals and the relative magnitude of the beam particle source, show that the source profile and magnitude do not determine the density profile. The fact that neither of the above mentioned parameters provides a statistically convincing alternative to collisionality as the main scaling parameter for $n_{e0}/< n_e >$ is also confirmed by two parameter regressions.
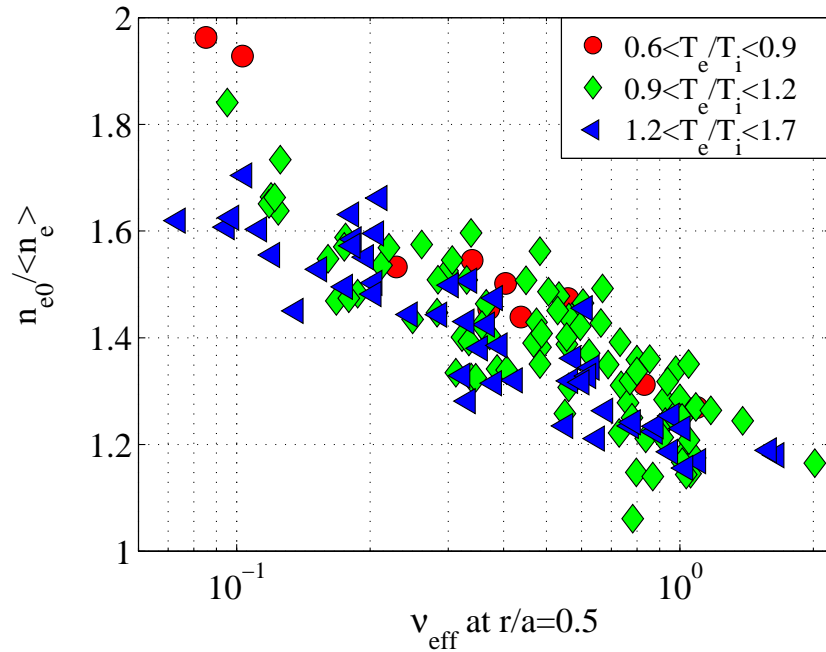
Figure 6.18: *Density peaking factor in H-mode versus ν_{eff} at $r/a = 0.5$. Symbols refer to the classes of T_e/T_i ratio evaluated at $r/a = 0.5$.*

In order to find any additional dependencies to ν_{eff}, we used three parameter linear regressions (Table 6.3). We selected only samples for which T_i was measured assuring the compatibility of the results of different regressions. When l_i is taken in addition to ν_{eff}, σ is decreased (column #2) showing the relation already presented in Table 6.2 for separated domains of ν_{eff}. A decrease of σ by 5% is observed when the T_e/T_i ratio is adopted as a second parameter in the regression (column #3 in Table 6.3). In Fig. 6.18 the dependence of the density peaking on the effective collisionality is resolved into the classes of T_e/T_i. Visually the discharges with higher T_e/T_i seem to be slightly broader and this is confirmed by the negative sign of the coefficient for T_e/T_i. The result is in agreement with the flattening of the density profile in response to the increase of electron heating observed in TCV ECRH discharges (see section 5.3) and in ASDEX Upgrade discharges [101]. This suggests that on all three tokamaks the flattening is related to destabilisation of TEMs. According to theory, destabilisation of TEMs leads to outward pinch which partly cancels the inward pinch produced by TEP or TTD thereby broadening the density profiles [101]. The weakness of density flattening in JET may be due to a lack

	1	2	3	4	5	6	7	8	9
c_0	1.25 ± 0.02	1 ± 0.02	1.39 ± 0.06	1.27 ± 0.04	1.31 ± 0.03	1.29 ± 0.04	1.25 ± 0.03	1.28 ± 0.04	1.11 ± 0.1
$\log(\nu_{eff})$	-0.18 ± 0.01	-0.19 ± 0.01	-0.19 ± 0.01	-0.19 ± 0.02	-0.18 ± 0.02	-0.17 ± 0.02	-0.19 ± 0.02	-0.19 ± 0.02	-0.19 ± 0.01
l_i		0.28 ± 0.12							0.35 ± 0.12
T_e/T_i			-0.12 ± 0.05						-0.16 ± 0.05
$10^2 \rho_e^*$				-0.05 ± 0.07					
β_N					-0.04 ± 0.02				
$< n_e > /10^{20}$						-0.09 ± 0.07			
$10^7 \tau_e |V_{loop}|/I_p$							0.02 ± 0.19		
$P_{tot}/10^7$								-0.03 ± 0.03	
$\sigma \cdot 100$	8.13	7.77	7.74	8.02	7.85	8.0	8.6	8.05	7.15

Table 6.3: *Results of multi parameter linear regressions performed on data subset with T_i measurements available. Intervals are given for the 90% confidence level. Dataset contains 140 samples.*

of electron heating power available at JET.

A three parameter regression with β_N as a secondary parameter improves σ by 3% with respect to regression #1. The $c_{\beta N}$ is however very small in comparison with $c_{\nu eff}$. Regression #7 shows that the parameter $\tau_E V_{loop}/I_p$ does not influence the density profile. An addition of parameters ρ^*, $< n_e >$ or $T_e(0)/ < T_e >$ to the leading scaling with $\log \nu_{eff}$ does decrease the σ of regression #1 in Table 6.3, however the errors in the coefficients are comparable or larger than coefficients, illustrating the lack of further statistically meaningful dependencies. Among the secondary parameters tested, l_i and T_e/T_i appear to be the most significant ones. When ν_{eff}, l_i and T_e/T_i are used together σ is further reduced (column #9). The coefficients c_{li} and $c_{Te/Ti}$ are similar, showing the equal importance of l_i and T_e/T_i in the four parameter fit.

The agreement between JET and ASDEX Upgrade, together with the lack of noticeable dependencies on dimensionless parameters ρ^* or β_N, suggests that an extrapolation to ITER should be possible. Assuming otherwise similar conditions, we expect $n_{e0}/ < n_e > \sim 1.7$ for the collisionality of the ITER reference H-mode ($\nu_{eff} \simeq 0.06$ at $r/a = 0.5$), corresponding to $R/L_n \approx 5 \pm 1$ at mid-radius. This is proposed to apply to the initial, non-active phase of operation when hydrogen or helium will be used as working gases. Extrapolation to ignited conditions is however uncertain, because the large electron heating power deposited in the core by α-particles. The amount of net electron heating and their effect on TEMs will however be reduced by electron-ion coupling, for which smaller devices with high local electron heating power densities, as TCV and ASDEX Upgrade, are not necessarily representative.

6.4 Summary

In normal shear L-mode plasmas with fixed $q_{95} = 8$, the peaking of the density profiles is found to scale with the peaking of the current profile,

$$\frac{n_{e0}}{< n_e >} = \frac{1}{0.88 < j > /j_0 + 0.29}$$

with no significant dependence on the peaking of the electron temperature profile. A more general relation,

$$\frac{n_{e0}}{< n_e >} = 1.18 \cdot l_i + 0.48$$

was found to be applicable to both the positive and the negative magnetic shear plasmas in the dataset. A contribution from the Ware pinch can be excluded for the fully lower hybrid current driven plasmas in the dataset. Density peaking is also independent of effective collisionality in the range covered by these experiments, $0.2 < \nu_{eff} < 1.1$, for ν_{eff} evaluated at 50% of the minor radius. Analysis of the anomalous pinch in TCV have not provided the answer to the question of the relative importance of TEP and anomalous thermodiffusion. The present LHCD experiments have clearly identified TEP, rather than anomalous thermodiffusion, as the dominant anomalous process of particle convection at normal shear.

The density profiles in normal shear discharges are in fair agreement with simple model profiles derived from TEP theory, with a free parameter $\eta \simeq 0.75$ in agreement with DIII-D and TCV ECRH results. However, a monotonic density profile in the core at negative shear cannot be explained solely by TEP.

A large representative set of stationary ELMy JET H modes and 'hybrid scenario' H-modes exhibits a clear collisionality dependence of the density peaking

$$\frac{n_{e0}}{< n_e >} = -0.17 \log \nu_{eff} + 1.28$$

This dependence is similar to the one observed in ASDEX Upgrade H-modes [26]. An important shear dependence of density profiles was found in JET H-mode for low collisionalities $\nu_{eff} < 0.25$. For higher ν_{eff}, the role of l_i significantly decreases. In addition to $\log \nu_{eff}$ and l_i, T_e/T_i it was found to slightly affect the density profiles. In all of the collisionality domain studied, the increase of T_e/T_i leads to broader density profiles. The density flattening in response to the increase of electron heating is in agreement with the ASDEX Upgrade observation [101] and also with the flattening of the density profiles in TCV in response to ECRH (see section 5.3).

Extrapolation of this results to the ITER reference H-mode gives the peaking $n_e/ < n_e > \sim 1.7$. These peaked profiles may significantly enhance fusion power in a reactor beyond the current expectations, which are based on flat profiles [109].

Chapter 7

Carbon transport estimates from ionization balance measurements in TCV

7.1 Introduction

Impurities released from the first wall and divertor plates due to plasma-wall interactions can have a major effect on plasma behaviour in tokamaks. They can penetrate into the main plasma column with several undesirable consequences such as:

- a reduction in the number of fuel ions in the plasma available for productive fusion interactions (dilution)

- large power losses from the plasma by radiation

- reduction of the density limit at which major disruptions occur

On the other hand, the presence of impurities in the tokamak plasma can also be beneficial, since impurity radiation is able to reduce the heat flux to the divertor, thereby reducing impurity production and thermal loading on the heat load components. Knowledge of impurity transport parameters and its relation with the transport of main plasma particles is therefore crucial in order to find the operating regimes with peaked profiles of the main density and at the same time without the accumulation of impurities in the centre of the reactor.

Transient perturbation methods are a proven technique to obtain impurity transport parameters [114, 115]. Injection of small amounts of impurities is performed using fast piezoelectric valves or the laser blow-off technique. Information on the transport is obtained from the detection of emission from impurity ionization stages located in different spatial regions, matched by numerical simulations of the detected signal using transport codes. The perturbation technique in not convenient, however for the study of intrinsic impurities. The main difficulty is to achieve the sufficient contrast on the detected signals with the small injected amount of impurities which should not change the properties of the plasma.

An alternative to the perturbation technique is the analysis of the impurity radiation detected by spectrometers in the steady state ionization equilibrium. For this purpose the impurity radiation has to be monitored along many different appropriately distributed chords simultaneously, in order to obtain a complete radial profile of line emission, which can be modelled using a transport code for the derivation the impurity transport coefficients. The advantage of the spectroscopy as a method for determination of transport parameters is the possibility to find lines which are specific to the relevant ionization stages of the impurity.

TCV is equipped with a four channel ultra soft x-ray (USX) spectrometer which can detect line radiation of He and H like lines of C, O and B [116]. However in the usual TCV plasma configurations, the radial distribution of the channels of the USX spectrometer covers only 40 % of plasma radius and there is normally no chord that sees the plasma edge where the line radiation profile of light impurities has maximum changes. These circumstances, as well as uncertainties in the relative calibration of the spectrometer channels, do not allow a measurement of the line emission profiles in such plasmas. Fortunately, the shaping capabilities of the TCV tokamak allowed us to slowly compress a plasma towards the high field side inner wall, thereby sweeping the low field side flux surfaces across the USX viewing lines with good spatial resolution in a single discharge.

In the following sections we describe the USX spectrometer, an experimental arrangement and a technique used for the estimation of transport parameters from steady state

profile of ionization stages of main intrinsic impurity in TCV, Carbon.

7.2 Spectrometer design

The USX spectrometer shown in Fig. 7.1 was designed and manufactured at the IPP Prague. Its uses multilayer mirrors (MLM) made from reflective artificial periodic structures composed of alternating layers of highly reflective materials and low Z spacers. MLM's offer diagnostic possibilities in the ultrasoft x-ray range (200-1000eV) wavelength range outside of the reach of most existing spectrometers, such as VUV instruments used at lower energies and x-ray spectrometers used at higher energies. The energy selectivity of the MLM's depends on the number of layer pairs. The flat MLM's used on TCV have 30 to 50 layer pairs with periods in the range 3 to 7 nm, depending on their design wavelength range. Incident radiation is diffracted according the Bragg law, $m\lambda = 2d \times \sin\theta$.

The centre wavelength of each of the 4 channels of the device can be independently adjusted, while maintaining alignment thanks to a pantograph system, which mechanically couples the mirror position and incidence angle as it slides along a guiding rod, as well as the detector orientation. The channeltron detectors are housed in a cylindrical soft iron magnetic shield with a total thickness of 4 cm to guard them from the poloidal fields (0.1 T) at its location 1.5 m above the TCV vacuum vessel. The shielding is equipped with cylindrical holes for outgassing and for transmitting the radiation from the MLM's to the channeltron detectors. It rotates together with the detector inside it when the wavelength setting is changed. Residual magnetic fields in the detector area were measured to be as low 10^{-4} T.

The four channels of the device can use different mirrors and filters optimized for the ranges 200-300, 300-400, 400-500 and 500-800 eV respectively. For the experiments described here, all channels were equipped with MLM's for the Carbon energy range.

7.3 Radially resolved line profile measurements

Experiments were performed in several Ohmic L-mode limited discharges with plasma currents I_p ranging between 130 kA and 300 kA, line averaged electron densities in the
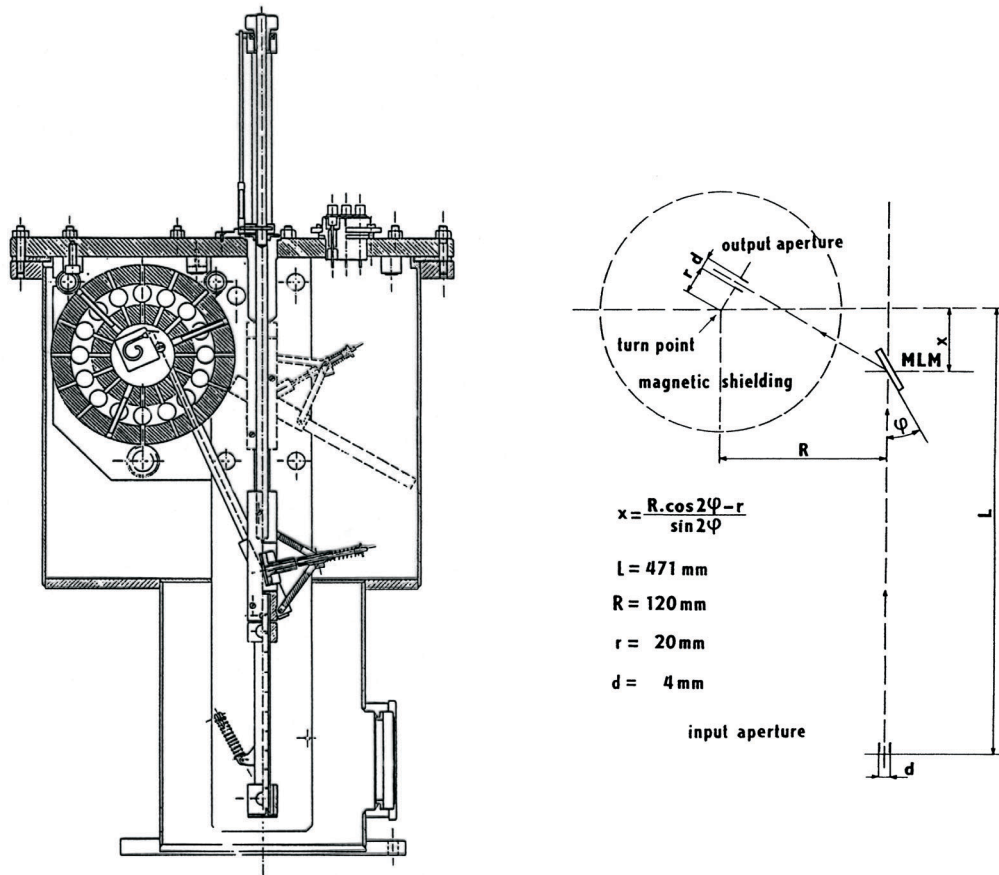
Figure 7.1: *Ultra-soft X-ray multichromator. Left: Overall design. Detectors are inside the magnetic shielding outlined by the broken circle. Separation from the TCV vacuum is achieved by polymer foils placed below the input aperture. Right: Ray path geometry.*

range $< n_e > \simeq 1 - 4 \cdot 10^{19}~m^{-3}$, central electron temperatures about 700-1100 eV, average elongation $\kappa \simeq 1.25$ and average triangularity $\delta \simeq 0.25$. The plasmas were compressed by some 10% while keeping the edge safety factor q_{95} constant. An example of temporal behaviour of current, safety factor and signals from the digital counter in a discharge with $n_e \simeq 3 \cdot 10^{19}~m^{-3}$ is shown in Fig. 7.2. All four channels measured CV radiation at 308 eV. The contours of the LCFS before the start of the compression and final LCFS contour at the end of the compression, when the plasma current is minimal, are shown on Fig. 7.2 at the right. The vertical lines indicate the lines of sight of the spectrometer. During the 300 ms of compression, each channel scans about 4 cm in the radial direction, resulting for the four channels in 80% coverage of the distance from the plasma centre to the low
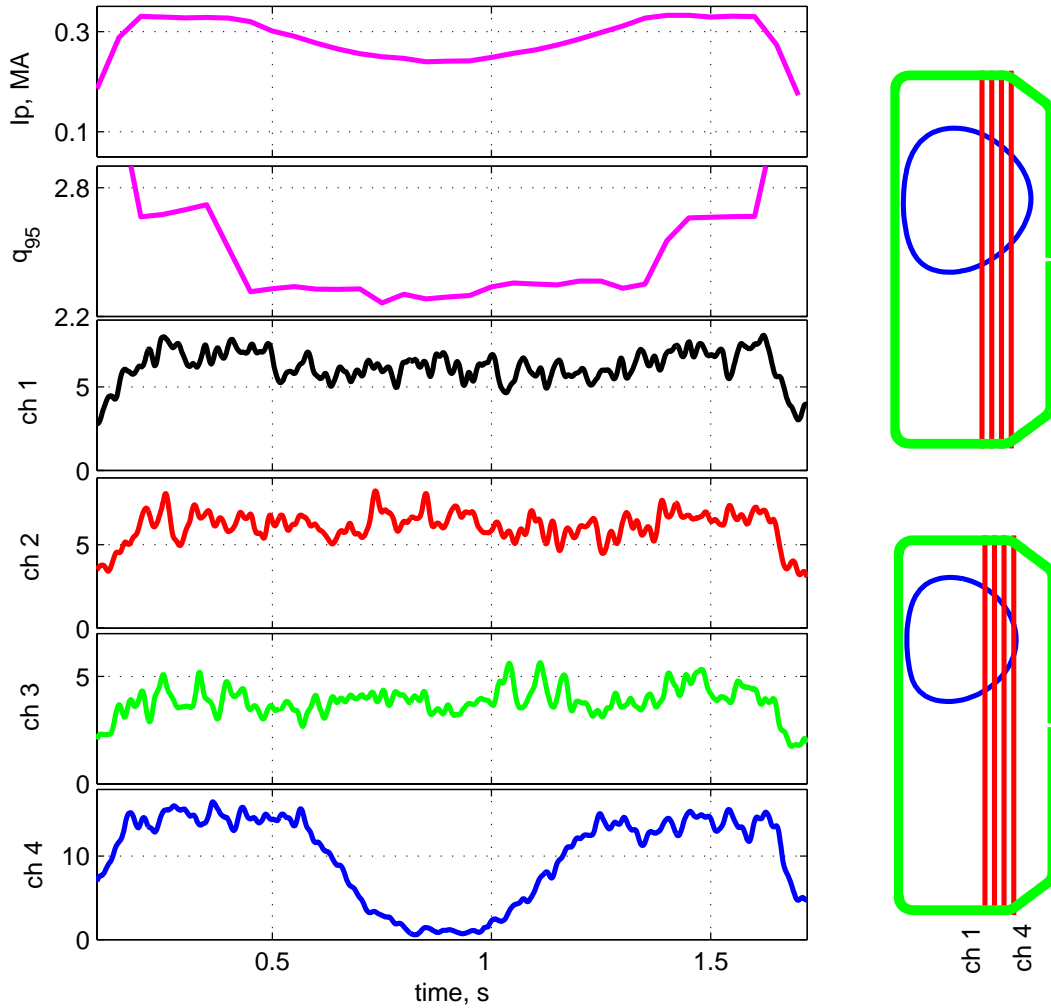
Figure 7.2: *On the left: plasma current, edge safety factor and time traces from digital counters of USX in TCV discharge #24429. On the right: contours of LCFS (blue) and the position of the USX chords (red) for two time moments.*

field side edge. It is seen that at the end of the compression the plasma edge is resolved up to the LCFS and the signal of the detector closest to the edge drops practically to zero. The signal fluctuations can be explained by poor photon statistics due to short integration length just inside the LCFS.

In order to derive an equivalent steady state profile of line emission, the main plasma parameters such as profile of the density and plasma safety factor at the edge were kept constant during the compression. It was assumed that current changes during the compression do not significantly affect the impurity transport parameters as long as edge safety factor remains constant (see section 5.2).

Due to the relatively small distance between channels, plasma positions, as quantified by the poloidal flux based normalised minor radius $\rho_{pol} = \sqrt{\psi/\psi_{LCFS}}$, seen by one channel in the beginning of the compression pass in front of the neighbouring channel at the end of the compression. This overlap allowed us to make a relative calibration of the channels, linking the values of the signal at different stages in the compression. It is essential for such a cross-channel calibration that the total impurity concentration during the compression remains constant. This was indeed ascertained using Z_{eff} derived from soft x-rays as described in [38]. To correctly connect the signals from neighbouring channels one should also take into account the changes in integration length during the sweep. To do so, signals from each channel were renormalised by the corresponding path length inside the LCFS at each time. The resulting normalised profile obtained from USX measurements at 308 eV is shown in Fig. 7.3 as a function of the impact parameter (smallest value of ρ_{pol}) of the viewing line. The different symbols correspond to the different channels of the spectrometer. In the plasma compression phase presented here, the signal of each chord starts at lower values of ρ_{pol} and goes to the right in ρ_{pol} as the plasma becomes smaller.
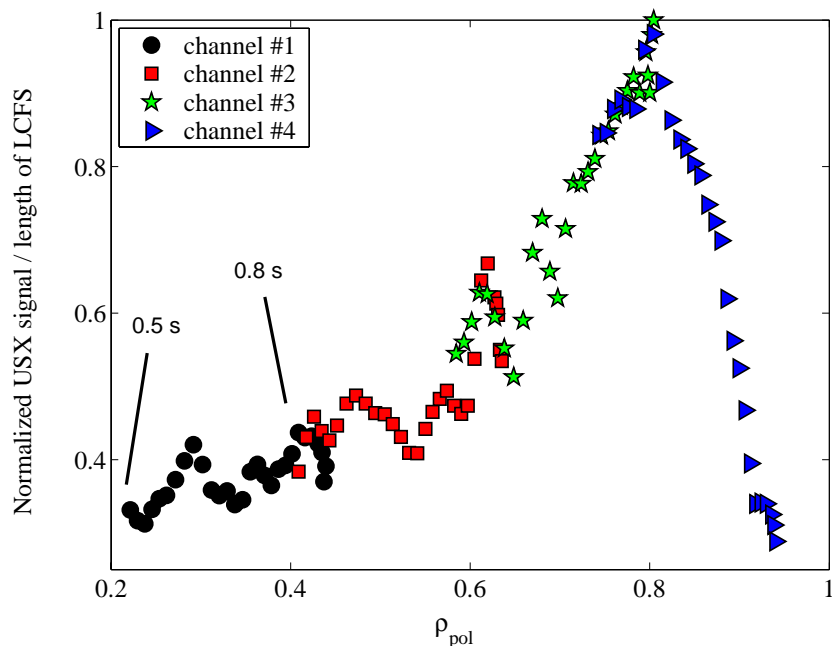

Figure 7.3: *The resulting normalized profile of line emission obtained from USX measurements at 308 eV (He-like line of carbon) and mapped on the ρ grid. The numbers on the graph correspond to the time of measurement for channel 1 (black dots)*

7.4 Modelling of the emission profiles

The profile shown above was deemed to represent a steady state line integrated emission profile of CV and was used to estimate carbon transport parameters by means of the STRAHL code [117]. STRAHL is a one dimensional transport code that calculates the solution of the equation of impurity particle conservation for each ionisation stage

$$\frac{\partial n_{I,Z}}{\partial t} = -\nabla \vec{\Gamma}_{I,Z} + Q_{I,Z}$$

where $\Gamma_{I,Z}$ is the flux density of the impurity and $Q_{I,Z}$ is the source/sink term, which includes ionisation, radiative, dielectronic and charge exchange recombination from and to the neighbouring ionisation stages. The impurity flux density was represented in the conventional form as a sum of diffusive and convective terms:

$$\Gamma_Z = -D_Z \nabla n + V_Z n$$

The background electron temperature and density profiles used in the simulations were taken form the Thomson scattering system and mapped onto the ρ_{pol} grid using the equilibrium code LIUQE [90]. Modelling included profiles of D and V as a function of ρ_{pol} as input parameters and the line brilliance as an output. The line emission profiles from the simulation were then mapped onto the real discharge geometry and integrated along each USX chord. Line integrals were normalised to the corresponding chord length in order to keep the same procedure as for the experimental profile on Fig 7.3. The resulting profiles were compared with experimental ones in order to find the D and V which give the best fit. To this effect the profiles of D and V were given by smoothly connecting 5 nodal points along the minor radius. The best fitting ones were found iteratively, by independently scanning the node values.

In Fig 7.4 (left) the experimental profile of integrated line emission measured by USX (dots) is plotted together with the simulated one (line) showing a good agreement between experiment and simulation for the CV line at 308 eV. We obtain consistent results when using the CVI line at 368 eV, as shown in Fig. 7.5 for an identical discharge (#24426).

The examples of radial profiles of the diffusion coefficients used in simulations are shown in Fig. 7.4 on the right. It was found that there is a range of profiles of the
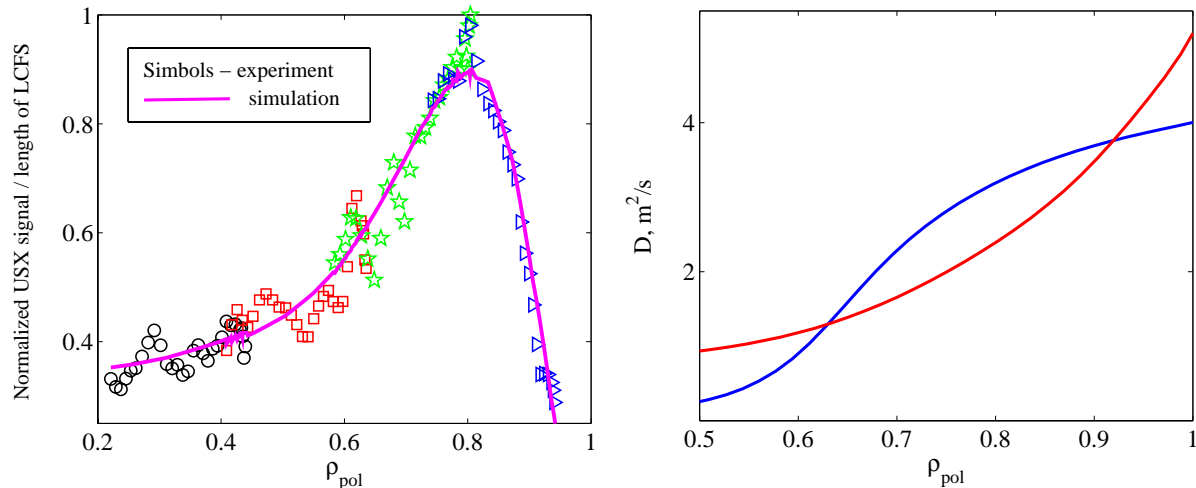
Figure 7.4: *The experimental profile measured by USX (dots) is plotted together with the simulated one (line). The corresponding diffusion coefficients are shown on the right.*

diffusion coefficient which give a good fit to the final profile of integrated line emission. In general, the best fitting profiles of D obey the following rule. The profiles with the highest values of D at the edge are also the ones with the steepest rise (concave profile on Fig. 7.4 right). Profiles with a lower value at the edge are associated with a more gradual decay towards the plasma centre. Based on the profiles of D suitable for this discharge, the accuracy in the determination of diffusion coefficient can be estimated at 30 % at the edge and 70 % at $\rho_{pol} \sim 0.6$. The values of D in the region $\rho_{pol} < 0.5$ do not influence the simulated profile.

Results were found to be practically independent of the profile of convective velocity. In the simulation, D were kept fixed while parabolic profiles of V were assumed with $V(0) = 0$ and $V(1)$ varied in the range 10 m/s to -10 m/s. Such variations resulted in changes in the final integrated profile, which are smaller than the experimental uncertainties. The reason could be the dominance of the diffusive part over the convective part in the total particle flux because of large values of CV (or CVI) density gradients distinctive for partly ionized stages in tokamak plasmas. Accordingly, the pinch velocity remains undetermined.

In Fig. 7.5 on the left, the experimental profiles of integrated emission of CVI (368 eV) line for two discharges are presented. Discharge #24426 (triangles) has an average plasma current of 0.27 MA and line average plasma density $< n_e > \simeq 4 \cdot 10^{19}$ m^{-3} The
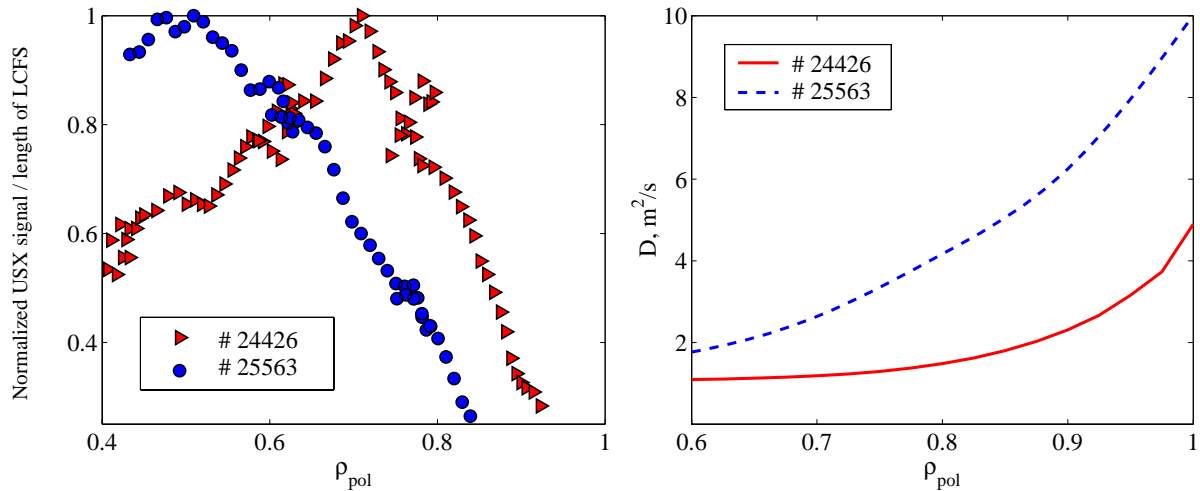
Figure 7.5: *The resulting normalized profiles of line integrated CVI (368 eV, H-like line) line emission mapped on the grid obtained from USX measurements in two different discharges with different plasma density Discharge #24426 was an identical repeat of the discharge shown in Fig. 7.4*

second discharge, depicted as dots, has the same average plasma current and significantly lower density $< n_e > \simeq 1 \cdot 10^{19}$ m^{-3}. The values of the edge safety factor are the same for both discharges and are equal to 2.2. The normalized temperature and density profiles were the same, but the axial temperature was higher in the lower density discharge, 1000 eV, as compared to 700 eV at high density.

The profiles of the integrated line emission for these two discharges are remarkably different. In the case of the lower density discharge, the maximum as well as the outer gradient region of the profile are displaced towards the plasma centre with respect to the profile in the discharge with higher density. If the transport parameters were the same, the maximum of the emission profile would be displaced outward for the low density case, not inward as observed. The difference can only be explained by a substantial increase of impurity diffusivity with decreasing density. The simulations reproduce both profiles well, giving, for the low-density discharge best fitting values of the D at the edge which exceed by a factor of two the values obtained at higher density (Fig 7.5 right).

7.5   Discussion

The relationship between particle and heat transport coefficients is a matter for concern in fusion reactors and is theoretically less straightforward than sometimes assumed, even in a two-species plasma [84]. The above profiles of the diffusion coefficient were compared with the profiles of the effective heat conductivity coefficient χ obtained from the power balance. In the case of the high density discharge, where χ is of the order of 4 m^2/s at the edge, the diffusion coefficient D is similar in the shape and in magnitude with χ. In low density case, χ rises to as high as 25 m^2/s at the edge. The carbon ion diffusion coefficient is higher than in the high density case as well, but does not exceed 10 m^2/s at the edge. One can conclude that the carbon diffusion coefficient is not related to the effective heat conductivity coefficient via a simple proportionality coefficient. This conclusion is confirmed by an analysis of several discharges with different values of χ.

A more relevant study should be made using separately determined electron χ_e and ion χ_i heat conductivities. Unfortunately, the large uncertainties related to the calculation of conductivities at the edge ($\rho_{pol} > 0.6$) due to errors in ion temperature profile and the equipartion term do not allow us to make a reliable analysis. An interesting particularity of the results obtained is that the best fitting values of diffusion coefficient in these experiments are higher by a factor of five than the values typically obtained in silicon laser ablation experiments [118]. The reason for such this discrepancy remains unknown, although it should be noted that the laser ablation experiments, which are analyzed using soft X-ray diagnostics in different discharges, only provide information for $\rho_{pol} < 0.8$, whilst the transport parameters from the experiments described in this paper are characteristic of the plasma periphery, $\rho_{pol} > 0.6$.

7.6   Summary

The extreme capabilities of the TCV tokamak allows to change the plasma shape in such a way that each chord of USX spectrometer sees the different regions of the plasma and thus it becomes possible to obtain the complete scan of the CVI or CV emission along the radii with good spatial resolution in a single discharge. These experiments were performed

in several Ohmic L-mode limited discharges with plasma current ranging between 0.13 and 0.3 MA, linear integrated electron densities in the range of $n_{el} \sim 1.1 - 4.3 \cdot 10^{19}$ m^{-2}. The measured profiles were assumed to represent steady state line emission profiles of carbon ions and were used to obtain carbon transport parameters by means of the STRAHL code. An analysis of several discharges showed that the bestfitting values for the diffusion coefficient at the edge in these experiments are in the order of $3 - 5$ m^2/s and increase when the density decreases. The comparison of this D with the heat conductivity χ showed that relation between them is more complex than a simple proportionality with a fixed coefficient.

Despite the promising results obtained we acknowledge that compression of the plasma is unpractical and introduces uncertainties in the analysis. For TCV a charge exchange diagnostic seems to be more attractive for systematic study of impurity transport. CX allows to perform the measurements of the ionization stage profiles without the compression and supplies local, not line integrated measurements [82]. Another advantage of CX is the possibility to measure the profile of the fully stripped population, which combined with measurements from partly ionized stage can provide the information on pinch velocity for the impurity.

Chapter 8

Conclusions and outlook

This thesis presents an extensive and systematic study of particle transport in TCV and JET, focussing on steady state electron density profile behaviour. The extreme flexibility of TCV in terms of plasma shaping and ECRH heating, as well as the large dimensions of JET, have allowed to create the density profile databases containing in total about 1600 density profiles as well as different plasma parameters, covering a very wide range of discharge conditions. The implementation of inversion techniques for line integrated interferometry measurements allowed to significantly improve the quality of the JET electron density profile data. In order to identify the processes underlying particle transport, the observed density profile behaviour was compared with expectations for different processes predicted by theory.

The analysis of density profiles behaviour in source-free steady state L-modes in Ohmic TCV plasmas showed that density peaking strongly correlates with the current profile width expressed by the parameter $< j > / (j_0 q_0)$, increasing as the current profile peaks. Remarkably, even in discharges with fast current modulation, the density profiles appear to follow, with no or little delay, the evolution of the current profile. In TCV L-mode ECRH plasmas, where the density profile broadens with respect to the Ohmic target, a scaling with deposition location, additional to the $< j > / (j_0 q_0)$ scaling, is observed. Central power deposition reduces the density peaking. Surprisingly, in TCV ECRH L-mode discharges, no dependence of the density peaking on the level of the ECRH power or on the absolute values of the temperature was found. The fact that at fixed current, profile peaking depends only on the location of the power suggests the existence of a threshold,

beyond which the net turbulent inward pinch is reduced. Since central ECRH power deposition increases the electron temperature and T_e/T_i, TEM may be responsible for this density behaviour, however detailed modelling is needed to confirm this hypothesis. The changes of the current profiles induced by additional heating may also cause or contribute to density flattening in the presence of ECRH, however for this work, reliable current profile measurements were not available. Future studies based on measurements of the current profile or its modelling may resolve the uncertainties in the interpretation of the results. Density peaking in the presence of the pumpout effect or strong eITB departs from the scaling observed for L-mode. This difference in behaviour was attributed to the presence of strong shear reversal and transport barrier in ITB discharges and MHD activity during pumpout.

Density peaking in source-free L-mode plasmas with LHCD in JET is observed to increase with increasing peaking of the current profile. In JET L-mode normal shear discharges, the peaking, as well as its scaling with the current profile width, is very close to observations in TCV. The internal inductance was found to be the best scaling parameter for density peaking in the JET LHCD L-mode dataset of normal and reversed shear discharges. We should mention, that in TCV the parameter $<j>/(j_0 q_0)$, being of course related to l_i, provides much better scaling for density peaking than l_i. The reason of this difference between JET and TCV may be related to the large variety of plasma shapes in TCV. Many parameters, which one might expect to be important for particle transport, such as ν_{eff}, ρ^*, T_e/T_i, β_N, $<n_e>$, V_{loop} appear to have a very weak or no influence on density peaking in L-mode. The density peaking behaviour of JET H-modes is remarkably different from that of L- modes, scaling with effective collisionality, with only a very slight dependence on shear, except at the lowest collisionalities when shear is important. This difference between L- and H-mode may be linked to the nature of the underlying turbulence (ITG in H-mode or TEM/ITG in L-mode). T_e/T_i was found to weakly affect the density profiles, increasing the peaking when T_e/T_i is decreased. No evidence for significant dependencies of $n_e(0)/<n_e>$ on ρ^*, β_N, $<n_e>$, V_{loop} in H-mode has been obtained.

In this work, special attention was devoted to the question whether the neutral particle

source situated at the plasma edge can explain the observed density peaking. Simulations performed using one dimensional kinetic transport code KN1D showed that the region over which the source term is important is restricted on TCV and JET, for the discharges considered, to the outermost few cm of the discharge and can be ignored in the particle balance equation in the confinement region. This argumentation is corroborated by the absence of a dependence of the experimental density peaking on the average plasma density and the working gas (D or He) on both machines, which is inconsistent with the large variations with average density or working gas of the penetration depth of the neutrals.

Comparisons with theoretically predicted processes, such as neoclassical transport, equipartition and thermodiffusion, showed that none of these processes reproduces all of the observed behaviour.

The neoclassical Ware pinch was found to be unable to explain peaking in Ohmic TCV plasmas in the confinement zone. The comparison of the convective flux due to the Ware pinch with the outward diffusive flux in several high power TCV ECRH discharges showed that the Ware pinch is too small to compensate for the diffusive outward flux. Peaked density profile in TCV and JET discharges with fully sustained current drive in the absence of core particle source unambiguously prove the presence of an anomalous inward pinch in tokamak plasmas. Despite the fact that in this work we found the Ware pinch to be an unimportant contributor to the electron density peaking in the confinement zone, we cannot exclude, however, that the Ware pinch may influence density peaking in the central regions of inductively sustained plasmas, especially in the low turbulence region in the presence of ITB's.

Positive shear L-modes in TCV and JET and JET H-modes at low ν_{eff} have profiles which are consistent with turbulent equipartition. The density profiles in TCV Ohmic discharges can be fitted by TEP alone if η is about 1. In the case of TCV ECRH heating, TEP seems to match well the experimental profiles however, a decrease of η is required to follow the flattening of the profiles as deposition of power becomes important. TEP provides a good description of density profiles in the JET normal shear discharges if $\eta \simeq 0.75$ however fails to reproduce the peaked density profile in the region of reversed

shear. A further theoretical difficulty is to understand why there is no evidence for a shear dependence for H-modes at $\nu_{eff} > 0.2$, despite the expectance that the curvature pinch is the dominant convective mechanism when ITG modes dominate.

In Ohmic TCV discharges, turbulent thermodiffusion alone provides sufficient peaking for the majority of the discharges if $0.4 < \alpha < 0.6$ but an additional scaling of α is needed to explain the observed scaling of density with parameter $< j > /(j0q0)$. In ECRH discharges, the modification of the temperature gradients by heating, together with the stiffness of the density profiles, leads to the necessity of assuming changes of α along the radius. TTD alone fits the density profiles in the ECRH discharges with values of α from 0.1 to 0.5 depending on the temperature profile modifications, however we did not find a specific dependence of α on discharge parameters. In most TCV discharges, the strong correlation of the temperature profile and current profile peaking does not allow to unambiguously separate the effect of the current profile from the effect of thermodiffusion. The scaling of peaking with l_i in JET L-mode discharges, together with the independence of the density peaking on gradients of the temperature, identify TEP rather than TTD as the main mechanism determining the electron density profile. At the same time the flattening of the density profiles in TCV ECRH discharges, as well as dependence of the density peaking on T_e/T_i in JET H-mode may indicate the presence of outward TTD in addition to a dominant inward pinch such as produced by TEP.

The above observations of electron density behaviour in TCV and JET pose welcome constraints on the theoretical understanding and on ongoing modelling efforts. A theoretical difficulty is the existence of peaked density profiles at high ν_{eff} in L-modes, while, for high values of ν_{eff}, H-mode profiles are much flatter. A surprising and theoretically puzzling observation is that the density peaking is observed throughout the entire collisionality range accessible to TCV, not just in low collisionality plasmas where full ECCD is achieved.

Based on the agreement of density profile behaviour in JET and ASDEX Upgrade H-modes, we suggested, for the collisionality of the ITER reference H-mode, the density peaking to be $n_{e0}/ < n_e > \sim 1.7$. This is proposed to apply to the initial, non-active phase of operation when hydrogen or helium will be used as working gases. The presence of α-

heating in D-T plasmas however makes the extrapolation to ignited conditions uncertain, because the large central electron heating power may destabilise TEM, which may reduce the peaking by outward TTD. However, even a more modestly peaked density profile would provide an appreciable gain in fusion power over the standard assumption of a flat profile.

Bibliography

[1] K. A. Brueckner and S. Jorna, "Laser-driven fusion", *Rev. Mod. Phys.*, vol. 46, p. 325, 1974.

[2] L. A. Artimovich, "Tokamak devices", *Nucl. Fusion*, vol. 12, p. 215, 1972.

[3] H. P. Furth, "Tokamak research", *Nucl. Fusion*, vol. 15, p. 487, 1975.

[4] J. Wesson, "Tokamaks", *Clarendon Press Oxford, Third edition*, 2004.

[5] M. Fujiwara *et al. Proc. 6th Int. Toki Conf. on Plasma Phys. and Contr. Nuclear Fusion (Toki, 1994)*, p. 58, 1994.

[6] G. Grieger *et al. Proc. 13th Int. Conf. on Plasma Phys. and Contr. Fusion Research, Washington, DC 1990)*, vol. 3, p. 525.

[7] R. F. Post, "The magnetic mirror approach to fusion", *Nucl. Fusion*, vol. 27, p. 1579, 1987.

[8] H. A. B. Bodin and W. E. Newton, "Reversed field pinch: Status and trends", *Plasma Phys. Control. Fusion*, vol. 29, p. 1297, 1987.

[9] F. Wagner and U. Stroth, "Transport in toroidal devices-the experimentalist's view", *Plasma Phys. Control. Fusion*, vol. 35, p. 1321, 1993.

[10] K. Borrass *et al.*, "Recent H-mode density limit studies at JET", *Nucl. Fusion*, vol. 44, p. 752, 2004.

[11] M. Greenwald, "Density limits in toroidal plasmas", *Plasma Phys. Control. Fusion*, vol. 44, 2002.

[12] G. T. Hoang, C. Bourdelle, B. Pégourie, B. Schunke, *et al.*, "Particle pinch with fully noninductive Lower Hybrid Current Drive in Tore Supra", *Phys. Rev. Lett.*, vol. 90, p. 155002, 2003.

[13] I. Furno, H. Weisen, and TCV Team, "Observation of inward and outward particle convection in the core of electron cyclotron heated and current driven plasmas in the Tokamak à Configuration Variable", *Phys. Plasmas*, vol. 10, p. 2422, 2003.

[14] A. A. Ware, "Pinch effect for trapped particles in a tokamak", *Phys. Rev. Lett.*, vol. 25, p. 916, 1970.

[15] L. Garzotti *et al.*, "Particle transport and density profile analysis of different JET plasmas", *Nucl. Fusion*, vol. 43, p. 1829, 2003.

[16] J. Nycander and V. V. Yancov, "Anomalous pinch flux in tokamaks driven by the longitudinal adiabatic invariant", *Phys. Plasmas*, vol. 2, p. 2874, 1995.

[17] V. V. Yankov, "Commentary on Pastukhov's paper (Sov. J. Plasma Phys., 1980, vol. 6, no. 5, p. 549) and the application of the turbulent equdistribution approach to the problem of transport in tokamaks", *Plasma Physics Reports*, vol. 21, p. 719, 1995.

[18] M. B. Isichenko, A. V. Gruzinov, P. H. Diamond, and P. N. Yushmanov, "Anomalous pinch effect and energy exchange in tokamaks", *Phys. Plasmas*, vol. 3, p. 1916, 1996.

[19] D. R. Baker and M. N. Rosenbluth, "Density profile consistency and its relation to the transport of trapped versus passing electrons in tokamaks", *Phys. Plasmas*, vol. 5, p. 2936, 1998.

[20] D. R. Baker *et al.*, "Particle transport phenomena in the DIII-D tokamak", *Nucl. Fusion*, vol. 40, p. 1003, 2000.

[21] F. Miskane and X. Garbet, "Anomalous particle pinch in tokamaks", *Phys. Plasmas*, vol. 7, p. 4197, 2000.

[22] X. Garbet *et al.*, "Turbulent particle transport in magnetized plasmas", *Phys. Rev. Lett.*, vol. 91, p. 03500, 2003.

[23] A. J. H. Nordman, J. Weiland, "Simulation of toroidal drift mode turbulence driven by temperature gradients and electron trapping", *Nucl. Fusion*, vol. 30, p. 983, 1990.

[24] R. Waltz *et al.*, "A gyro-Landau-fluid transport model", *Phys. Plasmas*, vol. 4, p. 2482, 1997.

[25] J. Weiland, "Collective modes in inhomogeneous plasmas", *IOP Publishing Ltd, Bristol, Philadelphia*, 2000.

[26] C. Angioni *et al.*, "Density peaking, anomalous pinch, and collisionality in tokamak plasmas", *Phys. Rev. Lett.*, vol. 90, p. 205003, 2003.

[27] L. M. Kovrizhnykh, "Neoclassical theory of transport processes in toroidal magnetic confinement systems", *Nucl. Fusion*, vol. 24, p. 851, 1984.

[28] K. Matsuda *et al. IEEE Trans. Plasma Sci.*, vol. 6, 1989.

[29] J. Sheffield, "Plasma scattering of electromagnetic radiation", *Academic Press*, 1975.

[30] R. Behn *et al. Proc. of the 7th Int. Symp. Laser Aided Plasma Diagnostics, Fukuoka*, p. 392, 2002.

[31] I. H. Hutchinson, "Principles of plasma diagnostics", *Cambrige University Press, Cambridge, UK*, 1987.

[32] N. Gottardi, "Evaluation of electron density profiles in plasmas from integrated measurements", *J. Appl. Phys.*, vol. 50, p. 2647, 1979.

[33] H. K. Park, "A new asymmetric Abel-inversion method for plasma interferometry in tokamaks", *Plasma Phys. Control. Fusion*, vol. 31, p. 2035, 1989.

[34] J. P. T. Koponen and O. Dumbrajs, "Electron density profile reconstruction from multichannel microwave interferometer data at W7-AS", *Rev. Sci. Instrum*, vol. 68, p. 4038, 1997.

[35] I. Furno *et al.*, "A new method for the inversion of interferometry data using basis functions derived from singular value decomposition of local measurements in tokamak plasmas", *Plasma Phys. Control. Fusion*, vol. 47, p. 49, 2005.

[36] M. Anton *et al.*, "X-ray tomography on the TCV tokamak", *Plasma Phys. Control. Fusion*, vol. 38, p. 1849, 1996.

[37] J. Stoer and R. Bulirsch, "Introduction to Numerical Analysis", *Springer. New York.*, 1980.

[38] H. Weisen, D. Pasini, A. Weller, and A. W. Edwards, "Measurement of light impurity densities and Z_{eff} in JET using x-ray tomography", *Rew. Sci. Instrum*, vol. 62, p. 1531, 1991.

[39] M. Keilhacker *et al.*, "High fusion performance from deuterium-tritium plasmas in JET", *Nucl. Fusion*, vol. 39, p. 209, 1999.

[40] P. R. Thomas *et al.*, "Observation of alpha heating in JET DT plasmas", *Phys. Rev. Lett.*, vol. 80, p. 5548, 1998.

[41] E. Thompson *et al.*, "The use of neutral beam heating to produce high performance fusion plasmas including the injection of tritium beams into Jount European Torus (JET)", *Phys. Fluids B*, vol. 5(7), p. 2468, 1993.

[42] J. Jacquinot *et al.*, "Preliminary ICRF results from JET", *Plasma Phys. Control. Fusion*, vol. 27, p. 27, 1985.

[43] D. F. H. Start *et al.*, "Bulk ion heating with ICRH in JET DT plasmas", *Nucl. Fusion*, vol. 39, p. 321, 1999.

[44] C. D. Challis *et al. Nucl. Fusion*, vol. 29, p. 563, 1989.

[45] L.-G. Errikson, T. Hellsten, and U. Willén, "Comparison of time dependent simulations with experiments in ion cyclotron heated plasmas", *Nucl. Fusion*, vol. 33, p. 1037, 1993.

[46] M. Lennholm *et al. Fusion Engineering, 1995. SOFE '95. 'Seeking a New Energy Era', 16th IEEE/NPSS Symposium*, vol. 1, p. 754, 1995.

[47] D. Mazon *et al.*, "Active control of the current density profile in JET", *Plasma Phys. Control. Fusion*, vol. 45, 2003.

[48] G. M. D. Hogeweij *et al.*, "A model for electron transport barriers in tokamaks, tested against experimental data from RTP", *Nucl. Fusion*, vol. 38, p. 1881, 1998.

[49] X. Litaudon *et al.*, "Electron and ion internal transport barriers in Tore Supra and JET", *Plasma Phys. Control. Fusion*, vol. 41, 1999.

[50] S. Ide *et al.*, "Formation and sustainment of ITBs under various heating schemes in JT-60U", *Plasma Phys. Control. Fusion*, vol. 44, 2002.

[51] G. Braithwaite *et al.*, "JET polari-interferometer", *Rev. of Scient. Instrum.*, vol. 60, p. 2825, 1989.

[52] C. W. Gowers *et al.*, "Recent developments in LIDAR thomson scattering measurements on JET", *Review of Scientific Instruments*, vol. 66, p. 471, 1995.

[53] D. V. Bartlett *et al. Electron Cyclotron Emission and Electron Resonance Heating (Proc. 9th Joint Workshop Borrego Springs) World Scientific Publishing, Singapore*, p. 511, 1995.

[54] M. von Hellermann *et al.*, "Visible charge exchange spectroscopy at JET.", *Rev. Sci. Instrum*, vol. 61, p. 3479, 1990.

[55] H. Salzmann and K. Hirsch, "Time-of-flight Thomson backscattering technique for large fusion devices", *Rew. Sci. Instrum*, vol. 55, p. 4, 1984.

[56] L. L. Lao *et al.*, "Equilibrium analysis of current profiles in tokamaks", *Nucl. Fusion*, vol. 30, p. 1035, 1990.

[57] L. Zabeo *et al.*, "A versatile method for the real time determination of the safety factor and density profiles in JET", *Plasma Phys. Control. Fusion*, vol. 44, p. 2483, 2002.

[58] F. L. Hinton and R. D. Hazeltine, "Theory of plasma transport", *Rev. Mod. Phys.*, vol. 48, p. 239, 1976.

[59] A. Galeev and R. Sagdeev, "Theory of neoclassical diffusion", *Rev. of Plas. Phys.*, vol. 7, p. 257, 1979.

[60] S. Hirshmann and D. Sigmar, "Neoclassical transport of impurities in tokamak plasmas", *Nucl. Fusion*, vol. 21, p. 1079, 1981.

[61] R. K. Varma, "Anomalous particle pinch in tokamaks", *Plasma Phys. Control. Fusion*, vol. 40, p. 1999, 1998.

[62] R. K. Varma, "Anomalous particle pinch in tokamaks", *Plasma Phys. Control. Fusion*, vol. 41, p. 1053, 1999.

[63] O. Sauter *et al.*, "Marginal β-limit for neoclassical tearing modes in JET H-mode discharges", *Plasma Phys. Control. Fusion*, vol. 44, p. 1999, 2002.

[64] O. Sauter and C. Angioni, "Neoclassical conductivity and bootstrap current formulas for general axisymmetric equlibria and arbitrary collisionality regime", *Phys. Plasmas*, vol. 6, p. 2835, 1999.

[65] B. B. Kadomtsev, "Tokamak plasma: A complex physical system", *IOP Publishing Ltd., Bristol*, 1992.

[66] R. J. Hastie, "Sawtooth instability in tokamak plasmas", *Astrophysics and Space Science*, vol. 256, p. 177, 1998.

[67] J. Wesson, "Sawtooth oscilations", *Plasma Phys. Control. Fusion*, vol. 28, p. 243, 1986.

[68] J. W. Connor, "A review of models for ELMs", *Plasma Phys. Control. Fusion*, vol. 40, p. 191, 1998.

[69] J. W. Connor, "Edge-localized modes - physics and theory", *Plasma Phys. Control. Fusion*, vol. 40, p. 531, 1998.

[70] J. Q. Dong, W. Horton, and J. Y. Kim, "Toroidal kinetic ν_i-mode study in high-temperature plasmas", *Physics of Fluids B*, vol. 4, p. 1867, 1992.

[71] W. Horton, "Drift waves and transport", *Rev. Mod. Phys.*, vol. 71, p. 735, 1999.

[72] W. Horton, D. Choi, and W. M. Tang, "Toroidal drift modes driven by ion pressure gradients", *Physics of Fluids*, vol. 24, p. 1077, 1981.

[73] P. N. Guzdar, L. Chen, W. M. Tang, and P. H. Rutherford, "Ion-temperature-gradient instability in toroidal plasmas", *Physics of Fluids*, vol. 26, p. 673, 1983.

[74] X. Garbet *et al.*, "Physics of transport in tokamaks", *Plasma Phys. Control. Fusion*, vol. 46, 2004.

[75] J. W. Connor, "Tokamak turbulence - electrostatic or magnetic ?", *Plasma Phys. Control. Fusion*, vol. 35, 1993.

[76] M. Z. Tokar *et al.*, "Model for the transition to the radiatively improved mode in a tokamak", *Phys. Rev. Lett.*, vol. 84, p. 895, 2000.

[77] P. C. Stangeby and G. M. McCracken, "Plasma boundary phenomena in tokamaks", *Nucl. Fusion*, vol. 30, p. 1225, 1990.

[78] R. K. Janev, "Elementary processes in hydrogen-helium plasmas : cross sections and reaction rate coefficients", *Springer-Verlag, Berlin ; New York*, 1987.

[79] D. Reiter, "The EIRENE code. User manual", *Jul 2599 KFA Julich, Germany*, 1992.

[80] B. LaBombard, "Manual of Kn1D code", 2002.

[81] R. Pitts *et al.*, "Divertor geometry effects on detachment in TCV", *Journal of Nuclear Materials*, vol. 290, p. 940, 2001.

[82] P. Bosshard, "Confinement ionique dans le tokamak TCV mesuré par le spectroscopie d'echange de charge", *PhD thesis No 2723(03), Ecole Polytechnique Fédérale de Lausanne, Switzerland*, 2003.

[83] K. W. Gentle, O. Gehre, and K. Krieger, "Determination of particle transport coefficients in ASDEX by gas modulation", *Nucl. Fusion*, vol. 32, p. 217, 1992.

[84] D. R. Baker *et al.*, "Measurement of electron particle transport coefficients in different operational modes of DIII-D", *Nucl. Fusion*, vol. 38, p. 485, 1998.

[85] J. O'Rourke, "Measurements of the electron source distribution and particle transport coefficients in JET", *Plasma Phys. Control. Fusion*, vol. 35, p. 585, 1993.

[86] I. Condrea *et al.*, "Helium discharge operations in TCV", *Proc. 29th EPS Conference on Controlled Fusion and Plasma Physics, Montreux, Switzerland, June 2002*, vol. 26B, pp. P–2.079, 2002.

[87] S. Erents *et al.*, "Simple relations between scrape-off layer parameters of high recycling divertors. Part I: The relation between 'upstream' density and temperature", *Nucl. Fusion*, vol. 40, p. 295, 2000.

[88] R. A. Pitts *et al.*, "Comparing scrape-off layer and divertor physics in JET pure He and D discharges", *Journal of Nucl. Materials*, vol. 313-316, p. 777, 2003.

[89] M. Valovič *et al.*, "Density peaking in low collisionality H-mode in JET", *Plasma Phys. Control. Fusion*, vol. 46, p. 1877, 2004.

[90] F. Hofmann *et al.*, "Tokamak equilibrium reconstruction using Faraday rotation measurements", *Nucl. Fusion*, vol. 28, p. 1871, 1988.

[91] H. Weisen *et al.*, "Shape dependence of sawtooth inversion radii and profile peaking factors in TCV L - mode plasmas", *Nucl. Fusion*, vol. 42, p. 136, 2002.

[92] J. Stober *et al.*, "Behaviour of density profiles of H-mode discharges in ASDEX Upgrade", *Plasma Phys. Control. Fusion*, vol. 44, 2002.

[93] M. A. Henderson *et al.*, "Control of electron internal transport barriers in TCV", *Plasma Phys. Control. Fusion*, vol. 46, 2004.

[94] Z. A. Pietrzyk, C. Angioni, *et al.*, "Central electron temperature enhancements due to sawtooth stabilization during counter electron cyclotron current drive in Tokamak à Configuration Variable", *Phys. Plasmas*, vol. 7, p. 2909, 2000.

[95] C. Angioni, "Modeling of electron transport and of sawtooth activity in tokamaks", *PhD thesis No 2469 Ecole Polytechnique Fédérale de Lausanne, Switzerland*, 2001.

[96] P. H. Rebut, P. P. Lallia, and M. L. Watkins *Proc. 12th Int. Conf. on Plasma Physics and Controlled Nuclear Fusion Research, Nice 1988, IAEA Vienna*, vol. 2, p. 191, 1989.

[97] F. Ryter *et al.*, "Confinement and transport studies of conventional scenarios in ASDEX Upgrade", *Nucl. Fusion*, vol. 41, p. 537, 2001.

[98] V. Erckmann and U. Gasparino, "Electron cyclotron resonance heating and current drive in toroidal fusion plasmas", *Plasma Phys. Control. Fusion*, vol. 36, p. 1869, 1994.

[99] TFR Group, "TFR, the tokamak of Tokamak de Fontenay-aux-Roses", *Nucl. Fusion*, vol. 25, p. 1011, 1985.

[100] H. Weisen, I. Furno, and TCV Team, "Particle transport with high power central ECH and ECCD in TCV", *Nucl. Fusion*, vol. 41, p. 1230, 2001.

[101] C. Angioni *et al.*, "Density response to central electron heating: theoretical investigations and experimental observations in ASDEX Upgrade", *Nucl. Fusion*, vol. 44, p. 827, 2004.

[102] Y. R. Martin *et al.*, "Accessibility and properties of ELMy H-mode and ITB plasmas in TCV", *Plasma Phys. Control. Fusion*, vol. 45, 2003.

[103] J. Stober *et al.*, "Optimization of confinement, stability and power exhaust of the ELMy H-mode in ASDEX Upgrade", *Plasma Phys. Control. Fusion*, vol. 43, p. 39, 2001.

[104] A. Pochelon *et al. Proc. 24th Eur. Conf. on Controlled Fusion and Plasma Physics (Berchtesgaden, 1997)*, vol. 21A, p. 537, 1997.

[105] S. Coda *et al.*, "High-power ECH and fully non-inductive operation with ECCD in the TCV tokamak", *Plasma Phys. Control. Fusion*, vol. 42, 2000.

[106] H. Weisen and E. Minardi, "Stationary magnetic entropy in ohmic tokamak plasmas: Experimental evidence from the TCV device", *Europhysics Letters*, vol. 56, p. 542, 2001.

[107] G. Becker, "Anomalous inward particle flux in tokamaks due to a thermoelectric-type effect", *Nucl. Fusion*, vol. 27, p. 11, 1987.

[108] J. Stober *et al.*, "Dependence of the density shape on the heat flux profile in ASDEX Upgrade high density H modes", *Nucl. Fusion*, vol. 41, p. 1535, 2001.

[109] ITER Physics Basis Editors *Nucl. Fusion*, vol. 39, p. 2137, 1999.

[110] R. Carrera *et al.*, "Island bootstrap current modification of the nonlinear dynamics of the tearing mode", *Physics of Fluids*, vol. 29, p. 899, 1986.

[111] Z. Chang *et al.*, "Improved confinement with reversed magnetic shear in TFTR", *Phys. Rev. Lett.*, vol. 74, p. 4663, 1995.

[112] G. V. Pereverzev and O. V. Zolotukhin *30th EPS Conference on Contr. Fusion and Plasma Phys., St. Petersburg, 11-17 July 2003 ECA*, vol. 27A, 2003.

[113] V. Mukhovatov *et al.*, "Comparison of ITER performance predicted by semi-empirical and theory-based transport models", *Nucl. Fusion*, vol. 43, p. 942, 2003.

[114] R. Dux *et al.*, "Z dependence of the core impurity transport", *Nucl. Fusion*, vol. 29, p. 1509, 1999.

[115] R. Giannella *et al.*, "Role of current profile in impurity transport in JET L mode discharges", *Nucl. Fusion*, vol. 34, p. 1185, 1994.

[116] V. Piffl, H. Weisen, A. Zabolotsky, and the TCV Team, "Ultrasoft x-ray spectroscopy using multilayer mirrors on TCV", *Plasma Phys. Control. Fusion*, vol. 46, p. 1659, 2004.

[117] R. Dux, "STRAHL User Manual", 2000.

[118] E. Scavino *et al.*, "Effects of plasma shape on laser blow-off injected impurity transport in TCV", *Plasma Phys. Control. Fusion*, vol. 45, p. 1961, 2003.

Acknowledgments

I would like to thank, first and foremost, my project mentor, Dr. Henri Weisen, for his guidance and support throughout my thesis work. I am deeply appreciate the tremendous amount of discussions that I had with him. He has always been a constant resource of information, new ideas and references.

I am indebted to Drs. O. Sauter and R. Pitts who have provided important advices during the course of the work, to Dr. R Behn with whom I have closely worked for the first 2 years, to Dr. K-D. Zastrow from whom I have learned a lot during JET trace-tritium campaign, to Drs. V.Piffl and X. Garbet for their input and interest in this research. I am grateful for the excellent codes which I have used in may work. Thanks go to Dr. R. Dux for providing the "Strahl" code and to Dr. B. LaBombard for the "Kn1D" code.

I would also like to express my gratitude to Prof. M. Q. Tran and Dr. K. Appert for giving me the opportunity to work nine months at CRPP in 1999 and then to start my PhD study at EPFL.

I am very grateful to the all staff at TCV and JET who have shared their time, energy and expertise. Special thanks go to P. Marmillod, B. Marlétaz and P. Lavanchy of the CRPP electronic workshop for their help and advice in the integration of the diagnostic which I have been using during my work. I greatly appreciate the computing assistance I received from X. Llobet et P. Etienne. I am also indebted to the members of technical staff of TCV P. Conti, O. Bartolomeoli and C. Raggi for their precious help.

In addition to the supervisors, collaborators, and colleagues who have directly contributed to this thesis work, my research life has been supported by many generous, warm-hearted people, without whom I could not have accomplished the thesis. I would like to thank E. Grüter and P. Halter who made administrative side of my life much easier and who always had a pleasant word and a smile for me. I would like to thank PhD students of CRPP. They all made my stay in Lausanne very pleasant and enjoyable.

I would like to send my best thanks to my mother, Lubov, father, Yuri, and brother, Dimitri for their every support in my long student life. Finally, I would like to thank my wife, Ilyana, who is my deepest love. This work, and my life, are dedicated to her.

Curriculum vitae

NAME: Alexey Zabolotskiy

DATE OF BIRTH: 14 January 1975

PLACE OF BIRTH: Novosibirsk, Russia

EDUCATION and EXPERIENCE:

October 2000 - present	**Centre de Recherches en Physique des Plasmas** Ecole Polytechnique Fédérale de Lausanne, Switzerland *Assistant and Doctoral Student*
1999-2000	**Centre de Recherches en Physique des Plasmas** Ecole Polytechnique Fédérale de Lausanne, Switzerland *9 months employment financed by Swiss government scholarship*
1996-1999	**Novosibirsk State University, Russia** *A master of science degree in physics*
1992-1996	**Novosibirsk State University, Russia** *A bachelor of science degree in physics*
1982-1992	**Primary and secondary school, Kuibushev,** **Novosibirsk region, Russia**

PUBLICATIONS:

- **A. Zabolotsky**, H. Weisen and TCV Team, *"Observation and empirical modelling of the anomalous particle pinch in TCV"*, Plasma Physics and Controlled Fusion 45, No 5 (May 2003), 735-746

- H. Weisen, **A. Zabolotsky**, C. Angioni, I. Furno, X. Garbet, C. Giroud, H. Leggate, P. Mantica, D. Mazon, J. Weiland, L. Zabeo, K.-D. Zastrow and JET-EFDA

contributors,*"Collisionality and shear dependences of density peaking in JET and extrapolation to ITER"*, Nuclear Fusion 45 (2005), L1-L4

- H. Weisen, **A. Zabolotsky**, X. Garbet, D. Mazon, L. Zabeo, H. Leggate, M. Valovic, K.-D. Zastrow and contributors to the JET-EFDA work programme, *"Shear dependence of density peaking in JET"*, Plasma Physics and Controlled Fusion 46, No 5 (May 2004), 751-765

- V. Piffl, H. Weisen, **A. Zabolotsky** and the TCV Team,*"Ultrasoft x-ray spectroscopy using multilayer mirrors on TCV Plasma"*, Phys. Control. Fusion 46, 1659-1674

- I. Furno, H. Weisen, C. Carey, C. Angioni, R. Behn, E. Fable, **A. Zabolotsky**, the TCV team and JET-EFDA Contributors, *"A new method for the inversion of interferometry data using basis functions derived from singular value decomposition of local measurements in tokamak plasmas"*, Plasma Phys. Control. Fusion 47, (2005), 49-69

- A. W. Degeling, H. Weisen, **A. Zabolotsky**, B. P. Duval, R. A. Pitts, M. Wischmeier, P. Lavanchy, Ph. Marmillod, and G. Pochon, *"AXUV bolometer and Lyman-α camera system on the TCV tokamak"*, Review of Scientific Instruments 75, 4139 (2004)

- X. Garbet, P. Mantica., H.Weisen, **A. Zabolotsky**, L. Garzotti, H. Hordman, M. Valovic, and the JET EFDA Contributors, *"Theoretical investigation of anomalous particle pinch and comparison with JET experimental results"*, 30th EPS Conference on Controlled Fusion and Plasma Physics, St.Petersbourg 7-11, July 2003

- I. Condrea,R. Pitts,B.P. Duval, S.M. Ahmed, **A. Zabolotsky**, M. Wischmeier, A. Karpushov, J. Horacek, Y.R. Martin, J. Mlynar, *"Helium Discharge Operations in TCV"*, Proc. 29th EPS Conference on Controlled Fusion and Plasma Physics, Montreux, Switzerland, June 2002, ECA Vol. 26B (2002), P-2.079

- E. Scavino, J.S. Bacos, H. Weisen, **A. Zabolotsky**, *"Impurity transport in shaped

TCV plasmas", 28th EPS Conference on Controlled Fusion and Plasma Physics, June 2001, Madeira, Spain

- A. D. Whiteford, K.-D. Zastrow, M. Adams, L. Bertalot, S. Conroy, M. G. O'Mullane, S. Popovichev, H. P. Summers, **A. Zabolotsky** and JET EFDA contributors, *"Quantitative forward modelling of neutron emission to derive transport coefficients of tritium in JET, including error propagation through to transport parameters"*, 31th EPS Conference on Controlled Fusion and Plasma Physics, London 28 June-2 July 2004.

- K-D. Zastrow, J. M. Adams, Yu. Baranov, P. Belo, L. Bertalot, J. H. Brzozowski, C. D. Challis, S. Conroy, M. de Baar, P. de Vries, P. Dumortier, J. Ferreira, L. Garzotti, T. C. Hender, E. Joffrin, V. Kiptily, J. Mailloux, D. C. McDonald, R. Neu, M. O'Mullane, M. F. F. Nave, J. Ongena, S. Popovichev, M. Stamp, J. Stober, D. Stork, I. Voitsekhovitch, M. Valovic, H. Weisen, A. D. Whiteford, **A. Zabolotsky** and JET EFDA Contributors. *"Tritium transport experiments on the JET tokamak"*, Plasma Physics and Controlled Fusion 46 No 12B, B255-B265